Mechanical Characterization of Soft Materials Using Volume-Controlled Cavitation

by

Wanis Nafo

A thesis
presented to the University of Waterloo
in fulfillment of the
thesis requirement for the degree of
Doctor of Philosophy
in
Civil Engineering

Waterloo, Ontario, Canada, 2020

Examining Committee Membership

The following served on the Examining Committee for this thesis. The decision of the Examining Committee is by a majority vote

External Examiner	**Prof. Abbas Samani** Department of Medical Biophysics & Department of Electrical and Computer Engineering, University of Western, Ontario.
Supervisor	**Prof. Adil Al-Mayah** Civil and Environmental Engineering, University of Waterloo.
Internal Member	**Prof. Hassan Baaj** Civil and Environmental Engineering, University of Waterloo.
Internal Member	**Prof. Scott Walbridge** Civil and Environmental Engineering, University of Waterloo.
Internal-external Member	**Prof. Duane Cronin** Mechanical and Mechatronics Engineering, University of Waterloo.

Author's Declaration

This thesis consists of material all of which I authored or co-authored: see Statement of Contributions included in the thesis. This is a true copy of the thesis, including any required final revisions, as accepted by my examiners.

I understand that my thesis may be made electronically available to the public.

Statement of Contribution

This thesis is comprised of seven chapters. At the time of submission of this thesis, four papers were produced based on the thesis' work. The analysis and discussion in all the papers were done by myself with guidance of my supervisor, Prof. Adil Al-Mayah. The experimental schemes were prepared and discussed together with my supervisor.

Chapter 3

Nafo, W., & Al-Mayah, A. (2019). Measuring Hyperelastic Properties of Hydrogels Using Cavity Expansion Method. Experimental Mechanics. https://doi.org/10.1007/s11340-019-00504-4.

Chapter4

Nafo, W., & Al-Mayah, A. Measuring the Hyperelastic Response of Porcine Tissues In-Vitro Using Controlled Cavitation Rheology. Submitted to Experimental Mechanics (under review).

Chapter 5

Nafo, W. & Al-Mayah, A. Characterization of PVA Hydrogels' Hyperelastic Properties by Uniaxial Tension and Cavity Expansion Tests. Submitted to International Journal of Non-Linear Mechanics (under review).

Chapter 6

Nafo, W. & Al-Mayah, A. Mechanical Characterization of PVA Hydrogels' Rate-Dependent Response Using Multi-Axial Loading. Submitted to Mechanics of Time-Dependent Materials (under review).

Abstract

The mechanical properties of soft materials are used in a wide range of fields and applications including biomedical engineering, sports, and automobile industry, in addition to medical applications. Therefore, several methods have been used to measure these properties including tension, compression, and indentation.

This study focuses on the application of multiaxial loading using cavitation mechanics to measure nonlinear mechanical properties of soft materials. It was found that applying controlled cavitation within the internal structure of soft materials provided enough information to characterize their mechanical behavior. This is done by inserting a needle-balloon tool inside the tested material while being attached to a system that allows for injections of an incompressible fluid (water) into the balloon.

To establish this methodology as a robust characterization technique of the mechanics of soft materials, it was used in a four-stages investigation: developing an analytical framework to characterize the non-linear elastic behavior of rubber-like materials (elastomeric gels), measuring the hyperelastic properties of soft biological tissues (porcine liver), comparing the cavity expansion test with a conventional uniaxial tensile testing, and establishing an analytical framework to characterize the time-dependent behavior of viscoelastic materials.

In the first stage, a solution that relates the applied radial loads and tangential deformation is introduced. This solution allows the calibration of hyperelastic strain energy functions (SEF), which were Yeoh, Arruda-Boyce and Ogden (used in all stages). Finite element simulations were used to validate the material parameters of the three hyperelastic models. Computed tomography (CT) imaging was used to validate the spherical configuration assumption of the inflated balloon inside the sample. The validation process considered the two types of stresses generated during the test, radial and hoop stresses. It was observed that the radial stresses were insignificant compared to the hoop stresses.

In the second stage, a smaller balloon was used to test porcine liver tissues; however, the protocol of this stage was similar to the first stage. Few changes were introduced to the definition of the deformation term, as a result, the measured deformations in the cavity test coincided with the deformation levels reported in literature. In addition, the three hyperelastic models predicted initial

shear moduli that agreed with their counterparts reported in literature using conventional testing techniques.

To understand the similarities and differences between the cavity expansion test and conventional axial loading, the third stage addressed the comparison between the cavitation and uniaxial tension characterization. The comparison focused on the stress levels, range of strains as well as the initial shear moduli. It was found that the strain levels in the hydrogels were similar up to the failure point. In addition, the hoop stresses generated due to cavity loads were similar to the tensile stresses generated in uniaxial tension up to a strain level of 45%. Afterward, hoop stresses increased exponentially reaching a peak magnitude that was twice that observed in the uniaxial tension. Since the radial stresses were insignificant, the previous two observations provided an indication to the equi-biaxial nature of the cavity expansion test.

The final stage of this study addressed the characterization of the viscoelastic properties of rubber-like materials. In this stage, linear viscoelastic theory was used. The cavitation rheology is used to measure the non-linear elastic response of the hydrogels at three different strain rates. The simple shear relaxation test was used to measure the viscous response of the hydrogels. While the elastic material parameters were calibrated using the same method used in previous stages, the viscous coefficients of the Prony series were determined using Abaqus' calibration tool. Afterward, the elastic parameters and viscous coefficients were used to reproduce the experimental data numerically using FE simulations, and analytically using Matlab code. The agreement between experimental data, FE simulations and the analytical code showed that the cavity expansion test was capable of measuring the time-dependent response of rubber-like materials.

Acknowledgements

I would like to take this opportunity to express my appreciation to those who provided me with guidance, assistance and support through this life-changing journey.

Foremost, I would like to express my sincere gratitude and appreciation to my supervisor, Prof. Adil Al-Mayah; his tactful guidance, patience and availability for discussions at any time were crucial in shaping this thesis to this level.

I would also like to thank my committee members, Prof. Abbas Samani from the University of Western Ontario, and Profs. Duane Cronin, Hassan Baaj and Scott Walbridge from the University of Waterloo for their insights and guidance.

Before thesis submission, parts of this thesis were peer-reviewed in the form of scientific journal articles. I would like to extend my gratitude and appreciation to editors and anonymous reviewers for their insights. They truly helped improve my work and reshape my notions about various challenges I encountered in my research work.

I am also grateful to the technical staff: Terry Ridgeway, Mark Griffett, Peter Volcic and Mark Sobon for their support and assistance.

I cannot take this opportunity without acknowledging the contribution of my colleague and friend, Mustafa Alhusain; we had various discussions and debates that helped improve my perspectives about challenges in research and life, thank you for amazing five years and countless years to come. I would also like to thank Chi-Hsiang Liao, Sarah Abu-Obaid, Piyius Raj Singh, Drs. AbdulRahman Ghannoum and Hamed Shahrokhi, and all the amazing friends I met during this journey.

Thank you all!

Dedication

To my parents who reserved no effort to support me, to whom I owe everything.

To my siblings, the backbone of my life. You have been and continue to be my comrades in the battle of life.

Thank you from the depth of my heart!

Table of Contents

List of Figures

List of Tables

Chapter 1

Introduction

Mechanical characteristics of soft materials such as biological tissues and elastomers play a significant role in numerous medical applications. For example, elastomers such as Polyvinyl alcohol (PVA) hydrogels are synthesized to match the mechanics of biological tissues such as articular cartilage and nuclus pulposus, and thus be suitable alternatives to damaged tissues (Joshi et al., 2006a; Ma et al., 2009). Understanding the mechanics of soft matter is also important to improve existing solutions. For instance, biomechanical-based deformable image registration (DIR) is used to improve the quality of image guided radiotherapy (Zhong et al., 2012) and surgery (Lim et al., 2009).

The mechanical behavior of soft materials is commonly measured using various techniques based on the applications of the tested materials. In the biomedical field, the mechanics of biological tissues is commonly measured using axial tension (uniaxial, planar and biaxial) (Fehervary et al., 2016; Jacobs et al., 2013a; Rashid et al., 2014a) , compression (Morriss et al., 2008), indentation (Li et al., 2019), and inflation (Kang, 2008). In most cases, the tissues are excised from their biological environment. It is not always possible to test the fresh tissues immediately after excision. Most of these tissues are preserved using different techniques such as fixation, refrigeration and freezing, and dehydration. These techniques were reported to have tangible effects on the mechanical properties of the preserved tissues (Betsch & Baer, 1980; Ling et al., 2016; Y.-C. Lu & Untaroiu, 2012a; Nicolle & Palierne, 2010). In addition, there are further challenges that normally arise in ex-vivo testing such as slippage and friction that might occur during uniaxial tension and compression tests, respectively. Therefore, this thesis focuses on the application of a new technique developed at the University of Waterloo (Al-Mayah, 2011) that have the potential to eliminate the challenges normally arise during the use of conventional techniques, and due to the storage process.

The proposed technique has the capacity to measure the mechanics of the materials' inner structure with minimal intervention. This can be achieved by inducing controlled volumes to apply spherical deformations while observing the consequent loads. The materials' behavior can then be characterized by analyzing the loads and deformations using different constitutive models. In this thesis, the capability of the proposed technique to measure the materials' mechanics readily is

demonstrated in the coming chapters, in which the mechanics of PVA hydrogels and porcine liver tissues were investigated.

1.1. Aims and Scope

The aims of this thesis are (1) establishing the use of a geometry-controlled cavitation as a valid method to measure the hyperelastic properties of soft materials; (2) measuring the nonlinear elastic properties of biological tissues such as porcine liver tissues and compare it to properties reported in literature using conventional techniques; (3) providing clear perspectives on the mechanism of the cavity expansion in terms of stresses, strains, and elastic moduli compared to a simple axial loading methodology; and (4) establishing the cavity expansion technique as a valid method to measure the rate-dependent response of isotropic viscoelastic soft materials.

The thesis presents experimental and analytical investigation of the nonlinear mechanical properties of soft materials. The experimental work includes tension, cavity expansion, simple shear relaxation, and compressibility tests. On the other hand, the analytical work includes the use of hyperelastic strain energy functions (SEFs) and Prony series for nonlinear elastic and viscos behaviors characterization, respectively. The thesis uses analytical tools that are available in most FE solvers. In addition to their availability in Abaqus, hyperelastic models such as Yeoh, Arruda-Boyce, and Ogden are used due to their efficiency in capturing the nonlinear elastic response of soft materials in different types of loading as will be shown in the coming chapters. The viscoelastic solution uses the linear viscoelastic material representation due to its applicability to the viscoelastic response of PVA hydrogels. All the analytical works are based on assuming the tested materials are isotropic. The least squares method is used to calibrate the hyperelastic models, and Abaqus' calibration tool is used to calibrate the coefficients of Prony series.

1.2. Thesis Contribution

The thesis' main contributions focus on using multiaxial loading conditions as a characterization technique of soft materials. The main three contributions are

1. Applying multiaxial loading methodology that allows for measuring the mechanics of soft materials. The proposed method is capable of eliminating the challenges that normally accompany conventional characterization techniques. The loading mechanism is based on applying pressure

in one direction, and tension in two orthogonal directions, a unique feature does not exist in traditional axial and local loading techniques.

2. Implementing a new calibration framework, which is capable of characterizing the non-linear elastic and time-dependent behaviors of soft materials. The calibration process is based on relating compressive loads to tension deformations to calibrate the material parameters of the chosen constitutive models. This process is achieved by using an algorithm that is based on the least squares method.

3. Clarifying the mechanism of the cavity expansion test; due to the multi-axial nature of the used technique, this thesis demonstrates the mechanism of cavity loads and how they differ from loads applied in a conventional tension test.

These three contributions are validated using three investigation methodologies, (i) experiments: cavity expansion test, uniaxial tension test, compressibility test, and simple shear test. These tests are used to obtain data necessary to calibrate the parameters of the chosen models; (ii) FE simulations: used to validate the calibrated parameters by reproducing the experimental data numerically; (iii) CT imaging: used to confirm the resemblance between the geometric configuration of the applied cavitation and the analytical solution.

1.3. Overview of the Thesis

This thesis is divided into seven chapters including the current one. In chapter 2, an introduction about the materials used in this thesis, experimental methods, and constitutive models are introduced. Chapter 3 presents the measurement of hyperelastic properties of PVA hydrogels using cavity expansion method. The purpose of this study is to introduce multi-axial experimental and analytical procedures to characterize the nonlinear elastic properties of rubber-like materials by controlled cavitation.

Due to the importance of hyperelastic properties of abdominal organs, particularly liver, in various medical and industrial applications, the multiaxial loading is used to measure the mechanical properties of porcine liver tissues as presented in chapter 4.

To further understand the mechanism of the cavity expansion testing, it was compared with one of the common characterization techniques, uniaxial tension test. In chapter 5, stress levels, range of

strains and initial shear moduli are compared to understand the differences between the two loading regimes.

Most rubber-like materials are commonly known of their viscoelastic properties. Thus, chapter 6 introduces analytical and experimental procedures to measure the viscoelastic properties of PVA hydrogels. In this study, hyperelastic models in addition to Prony series are used to describe the viscoelastic properties of the gels.

Chapter 7 presents conclusions and recommendations for future works.

Chapter 2

Background

2.1. Introduction

This chapter presents the background information for the materials, and experimental and analytical concepts used in this study. Section 2.2 introduces the two types of soft materials used in this study; PVA hydrogels and porcine liver. Section 2.3 discusses experimental techniques used to characterize the mechanical behavior of these materials. The non-linear elastic (hyperelastic) response of the investigated materials will be discussed in detail in section 2.4 including mathematical fundamentals, common models and implementation. Soft materials are also known by their viscoelasticity, therefore, the linear viscoelastic description to their behavior is introduced in section 2.5.

2.2. Soft Materials

The term "soft materials" refers to any material that deforms easily under externally applied loads. Soft materials include foams, gels, polymers, colloids and soft biological materials. In this study, the term is used to describe polymeric gels, particularly PVA hydrogels, and soft biological materials such as porcine liver tissues. While the PVA hydrogels are used more frequently in this thesis due to their availability and simple synthesis, the liver tissues are used as an application to investigate the potential of the proposed technique to measure the non-linear properties of biological tissues as will be shown in chapter 4.

2.2.1. *PVA Hydrogels*

PVA hydrogels are very popular in the biomedical field due to their physiochemical and bio-tribological properties (Pan et al., 2007; Suciu et al., 2004). This type of gels is considered a prospect replacement of damaged or diseased cartilaginous tissues. Under loading, PVA hydrogels mimic the mechanical response of articular cartilage. For example, PVA hydrogels exhibit exponential stress-strain response under compression, similar to that of articular cartilage. This is mainly due to the friction generated by free water flow in both materials (Li et al., 2016; Maiolo et al., 2012; Pan & Xiong, 2009). However, these hydrogels are not fully ready to replace articular cartilage due to lack of strength and toughness. Therefore, several investigations were performed to improve the gels' mechanical properties (Kokabi et al., 2007; Xu et al., 2018). In addition to

articular cartilage, PVA hydrogels proved to be able to mimic the mechanical properties of porcine aortic root and nucleus pulposus by controlling the preparation conditions of the hydrogels (Joshi et al., 2006b; Wan et al., 2002).

PVA hydrogels are a class of general category of gels known as polymeric gels. In general, this type of gels contains a polymer and a solvent forming a three dimensional network by physical or chemical bonds connecting macromolecular chains (Millon et al., 2006; Park & Park, 1996). These chains can be permanent when chemical crosslinkers are used, or reversible when physical crosslinking is performed (Lozinsky et al., 2001; Ottenbrite et al., 2010).

PVA is obtained by polymerization of vinyl acetate to poly (vinyl acetate) (PVAc), followed by hydrolysis of PVAc. The higher the hydrolysis degree, the lower solubility of the PVA. Thus, for PVA of more than 95 % hydrolysis degree, temperature greater than 70 ^{o}C is introduced to dissolve the PVA in water (Chang, 2000; Millon et al., 2006). To form hydrogels, PVA can be crosslinked physically or chemically. The latter can be performed by adding chemical materials such as formaldhyde, glutaraldhyde, acetaldehyde and other monoaldehydes (Chang, 2000; Drury & Mooney, 2003; Lozinsky et al., 2001; Millon et al., 2006) to the PVA solution. The physical crosslinking is done by subjecting PVA solutions to cycles of freezing and thawing. This process was adopted to synthesize PVA hydrogels in this study.

Producing PVA hydrogels by physical crosslinking was first reported in 1975 by Peppas (Peppas, 1975). Since then, numerous studies have investigated the effect of PVA content and processing parameters (the number of freeze-thaw cycles) on the hydrogels' mechanical performance, (Kobayashi & Hyu, 2010; Wan et al., 2002).

The mechanism of physical crosslinking of PVA hydrogels is based on phase separation, i.e. separating the solution into a PVA-rich phase and a water-rich phase. This process is crucial during the hydrogel gelation. When the PVA solution is exposed to sub-zero degrees (^{o}C), the water freezes, detaching PVA and creating zones of high PVA concentration. As the PVA chains come into close proximity with each other, hydrogen bonding and crystalline formation occur, which remain intact after thawing. As a result, a three dimensional network is created (Hassan & Peppas, 2000; Hatakeyema et al., 2005; Ricciardi et al., 2004), see Figure 2.1.

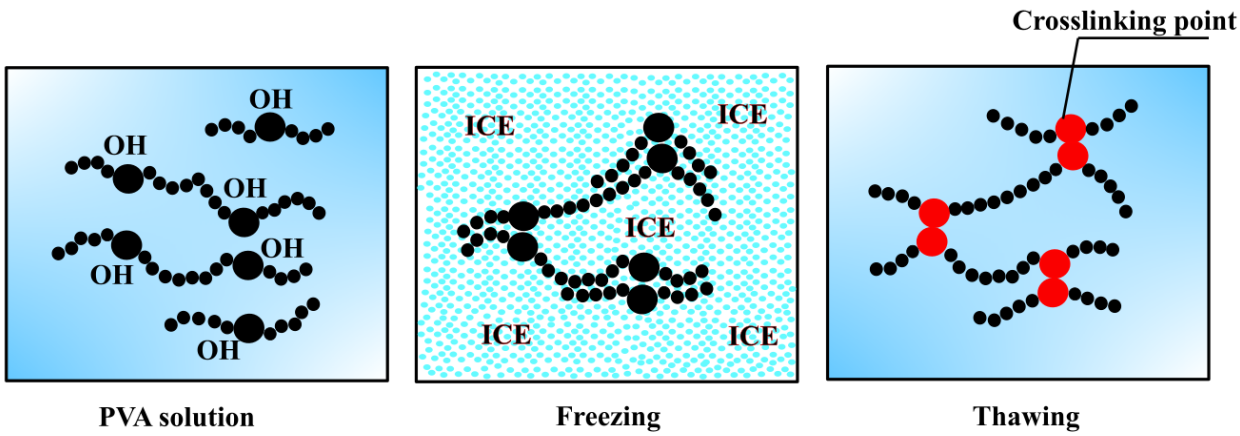

Figure 2. 1. Mechanism of physical crosslinking: One freeze-thaw cycle.

2.2.2. *Liver Tissues*

Understanding the mechanical behavior of liver tissues is fundamental in the biomedical field. These properties are indicative to the pathogenic condition of diseased tissues. In addition, these properties are essential for treatment applications such as computer-aided surgeries (surgical navigation) and radiotherapy (Al-Mayah et al., 2011; Chabanas et al., 2003; Eom et al., 2009a; Luboz et al., 2005) , which are developed and improved by using Finite Element (FE) models. In automobile accidents, liver is the most frequent abdominal organ to be injured due to its soft material properties (Feliciano, 1989), thus assessing liver damage during car accidents has been investigated in several studies (Chien et al., 2013; Holbrook et al., 2007; Slotta et al., 2014). In addition, numerous works developed biofidelic computational models to obtain infallible injury assessment of abdominal organs during traumatic events (Deng et al., 1999; Haug, 1997; Shao et al., 2013). The computational models used for surgical navigation and injury assessment of the liver require the knowledge of the organ's mechanical properties.

The biological structure of liver tissues is similar to other abdominal organs, in which it consists of parenchyma and capsule. The first carries out all biological functions of the organ, while the capsule is a dense fibrous tissue that covers the parenchyma. The combined mechanical behavior of the capsule and parenchyma was reported by Brunon et al., 2010, see Figure 2.2. In uniaxial tension, the mechanical response exhibits nonlinearity of the force-displacement relationship due to the rearrangement of randomly distributed collagen fibers. When they are fully extended, the tissues (parenchyma and capsule) show linear hardening until the capsule fails under loading. Afterward, all the loads transfer to the parenchyma which eventually ruptures releasing all the stored energy during the loading process (Nafo & Al-Mayah, 2018).

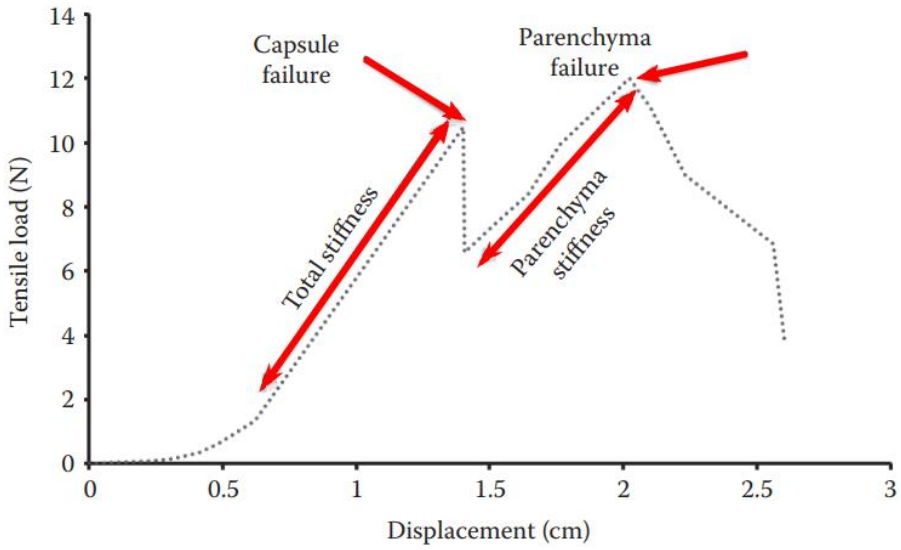

Figure 2. 2. Tensile load-displacement of liver tissues. Liver parenchyma is encapsulated inside the liver capsule. (Reprinted from Brunon, A.K. et al., *J. Biomech.*, 43, 2221–2227, 2010. With permission.).

Overall, the parenchyma is softer than the capsule, as shown in literature using stress-strain relationship. It was reported that, at failure, the parenchyma showed ultimate stress and strain of 61 kPa and 24 %, respectively (Kemper et al., 2010), while the capsule showed ultimate stress and strain of 9.2 MPa and 35.6 %, respectively (Hollenstein et al., 2006).

Liver tissues are also known to be viscoelastic. Kemper et al 2010 used uniaxial tension to test 51 liver samples extracted from 7 humans using four different rates (0.01 s^{-1}, 0.1 s^{-1}, 1 s^{-1} and 10 s^{-1}) (Kemper et al., 2010). It was shown that as the rate of loading increased, the ultimate stress of the tissues increased, while the ultimate strain decreased, see table 1.1.

Table 1. 1. Rate-dependence response of liver parenchyma in uniaxial tension (Kemper et al., 2010).

	Liver	
Strain rate (s^{-1})	**Ultimate stress (kPa)**	**Ultimate strain (%)**
0.01	40.21	34
0.1	46.79	32
1	52.61	30
10	61.02	24

2.3. Experimental Characterization Techniques

The experimental testing of soft materials is performed for various purposes, which include investigating a material's mechanical behavior, calibrating material models, studying materials' failure modes and testing for quality control. A number of testing techniques have been reported in the literature to fulfill these purposes; in this section, the focus is on the mechanical tests that were adopted in this study: uniaxial tensile test, simple shear test, volumetric test and cavity expansion test. In addition, a non-destructive x-ray micro-computed tomography (CT) scanning test will be addressed in this section.

2.3.1. *Uniaxial Tensile Test*

This test is very common in characterizing the mechanical response of soft materials due to its procedural simplicity and relatively direct data analysis (Jacobs et al., 2013b). In this test, a sample with a gauge length of "L" and a cross-sectional area (A) is gripped from both ends and stretched by the applied load (F) at a certain loading rate. The resulting load-displacement data can be normalized to obtain stress-strain (σ-ε) or stress-stretch (σ-λ) data essential to calibrate material models.

Some modifications were made to the tensile test to overcome some of the challenges associated with the loading grips, such as stress concentrations at the gripping region. To overcome this issue, specimens are normally cut into a dog-bone shape to ensure uniform deformation and stress distribution along the gauge length, see Figure 2.3 (a). Alternatively, the gripping force can be reduced while maintaining sufficient gripping stress to prevent slippage by using sand paper (Nafo & Al Mayah, 2018), see Figure 2.3 (b).

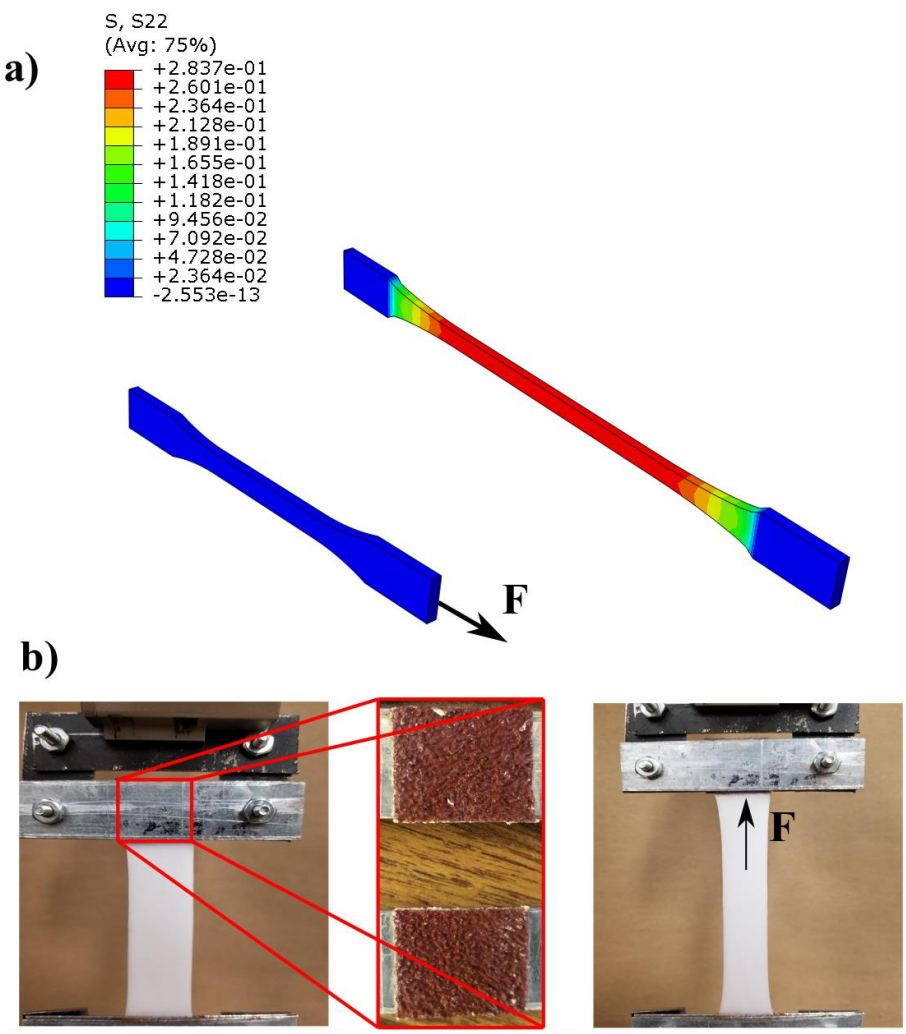

Figure 2. 3. a) FE simulation of dog-bone shaped specimen and the uniform distribution of stresses along the gauge length. b) Using sand paper to prevent the slippage of the aqueous PVA hydrogel strip at the gripping region.

2.3.2. *Simple Shear Test*

In characterizing the mechanical response of soft materials, many finite strain models decompose the material mechanical response into shear and volumetric behaviors (Bergstrom, 2015). Thus, it is sometimes required to evaluate the shear behavior of a material, including the long-term response (relaxation/creep) as demonstrated in FE solvers such as Abaqus ® (ABAQUS/CAE, 2013). This technique is commonly implemented in two configurations: single-lap or double-lap shear setup, see Figure 2.4.

Although both setups follow the same concept, the single-lap setup is more difficult to implement, as it is not self-aligned and errors due to rotation might occur if no attention was paid to the

gripping mechanism. These challenges are normally eliminated in the double-lap setup due to its symmetry.

Both setups are carried out using common uniaxial loading machines. The raw data obtained from this test is in the form of force-displacement, which can be converted into stress-strain form. Due to the plane state of the test, no change occurs to the area of the out-of-plane surfaces (Destrade et al., 2015). However, a numerical investigation showed that the specimen's height to width ratio should remain under 0.5. Higher ratios resulted into errors up to 17 % in predicting the experimental data (Bergstrom, 2015).

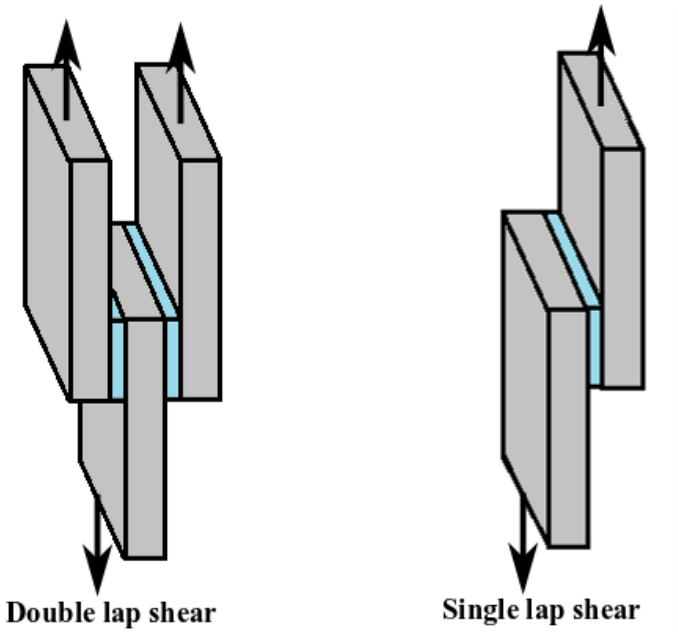

Figure 2. 4. Schematic figures of the both setups of the simple shear test. The regions represent the test samples.

2.3.3. *Cavity Expansion Test*

In a previous study (Nafo, 2016), an earlier prototype was used to measure the linear elastic stiffness of two types of PVA hydrogels and bovine liver tissues. In the current study, the experimental protocol as well as the analytical framework were developed. This enabled the technique to accurately characterize the hyperelastic and viscoelastic properties of the tested soft materials.

The analytical framework was developed to account for the mechanical nonlinearity of the soft materials in chapter 3, the same framework also used in the following chapters for calibrating the

hyperelastic models. Further development to the framework is presented in chapter 6 to consider the viscoelastic response of PVA hydrogels.

2.3.4. *Compressibility Tests*

The compressibility of a material is a measure of its volume change when subjected to external loads. Two common coefficients that determine the compressibility of a material are the bulk modulus (K) and the Poisson's ratio (ν). The liver tissues are normally considered incompressible (ν = 0.49999) (Glozman & Azhari, 2010). On the other hand, PVA hydrogels tend to exhibit very low compressibility (ν= 0.45 – 0.48) (Lee et al., 2013; Urayama et al., 1993). However, in FE applications, the compressibility (K and/or ν) of such materials have limited influence on the materials' mechanical behavior in different loading modes as demonstrated in (Bergstrom, 2015) as well as in chapter 3.

There are several techniques to measure the compressibility of soft materials. For example, Digital Image Correlation (DIC) systems (Chen et al., 2013) was used to measure axial and lateral strains during uniaxial loading. The strain data can be used to calculate the Poisson's ratio and then the bulk modulus (in case the elastic moduli are known).

Another technique to measure the compressibility of soft materials is known as fully confined compression test or volumetric test. In this approach, a cylindrical sample confined inside a rigid-walled cylinder, and then loaded with a punch that has the same diameter as the inner diameter of the containing cylinder, as shown in Figure 2.5. The force-displacement data obtained from this test can be converted into pressure-volumetric strain data by using the specimen geometry. The bulk modulus can then be calculated as the slope of this data. This test is demonstrated in chapter 3, where the compressibility of PVA hydrogels was measured.

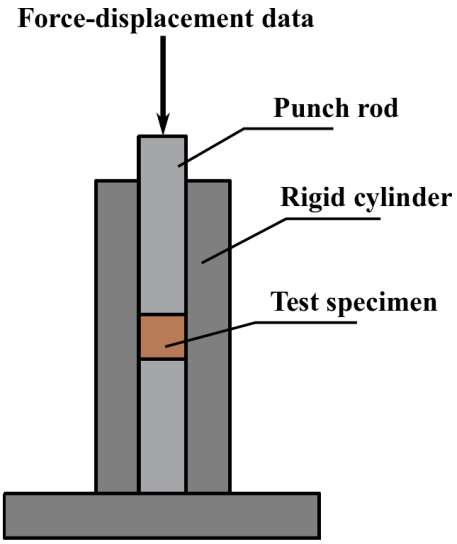

Figure 2. 5. Schematic figure of the fully confined compression fixture.

2.3.5. *Other Common Mechanical Testing Methods*

There are several other modes of loading, such as biaxial tension, torsion, split-Hopkinson pressure bar and compression tests. These modes are used to measure the mechanical behavior of the soft materials based on their applications, see Figure 2.6.

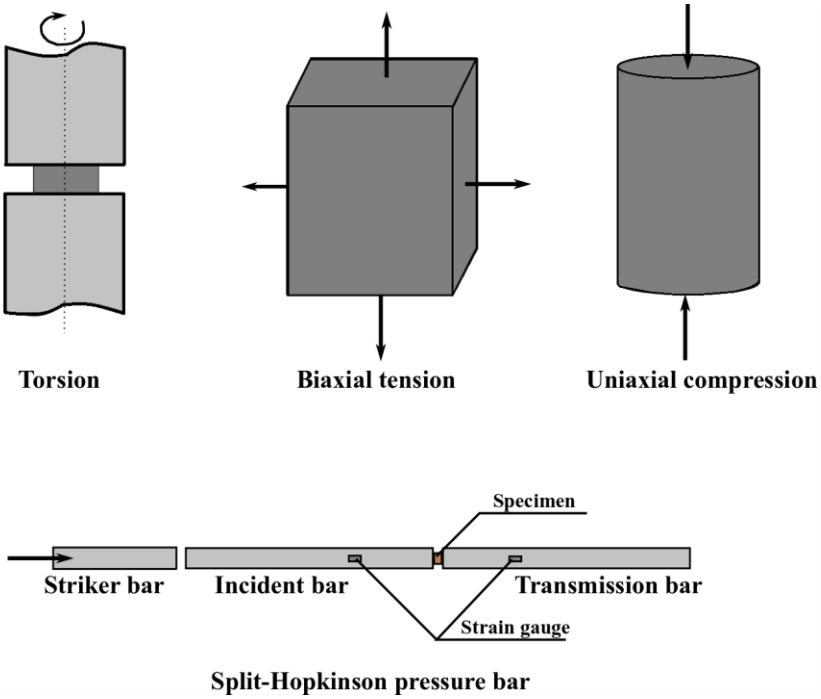

Figure 2. 6. Different loading modes to measure the mechanical behavior of soft materials.

The required accuracy of the used material model also defines the types of tests that need to be used. For example, to characterize the comprehensive behavior of an incompressible isotropic soft

material in tension using phenomenological models, it is recommended to test the material in both uniaxial and biaxial tension. On the other hand, more advanced micro-mechanical models are capable of predicting the comprehensive tensile behavior only by using the data from one test (uniaxial or biaxial tension) (Arruda & Boyce, 1993). However, this type of models still needs more experimental data in cases of predicting rate-dependence or temperature effect.

2.3.6. *Computed Tomography (CT) Scans*

Computed tomography scanning is based on taking two dimensional (2D) x-ray images at various angles from the scanned object. These images are then digitally reconstructed to create a three dimensional (3D) rendered volume. The components of any CT instruments are an x-ray source that emits penetrating radiation, a platform on which objects are positioned, and a detector (Duliu, 1999), see Figure 2.7. Overall, this technology is used for industrial and medical applications. Industrial CT is different from the medical CT in three aspects: (i) the detector and the x-ray source are stationary around a moving platform on which specimens are placed, (ii) industrial CT allow higher range of voltage and current that suit wide range of materials including dense materials, (iii) industrial CT have higher resolution, i.e., voxel size of 5 μm in micro-CT systems and 0.5 μm in nano-CT systems, while medical CT have a resolution of 70 μm at best (du Plessis et al., 2017).

The production of x-rays takes place inside the x-ray source (vacuumed tube) by heating a cathode (tungsten filament). The heating process generates a beam of electrons that travel in a vacuumed space (Pressure = 10^{-06} mmHg) to hit an anode (metal of high atomic weight). Electrons produce energy in the form of heat and x-rays. Since heat occurs on the surface of the anode, most CT instruments have a rotating anode to avoid local overheating of its surface. The x-rays are utilized by directing them towards any targeted object and then collected by a 2D detector.

After the detector collects the attenuated radiation, it converts the x-rays into 2D digital images commonly known as “projections” or “radiographs”. After all the projections are collected, a 3D volume can be reconstructed using appropriate algorithms (e.g. Feldkamp filtered back-projection algorithm (Feldkamp et al., 1984). A software package that is based on similar algorithms is Volume Graphics (*Volumegraphics.com*). Examples of this process will be shown in chapters 3 and 4, in which the x-rays are used to investigate the cavity deformation inside PVA hydrogels and porcine liver tissues.

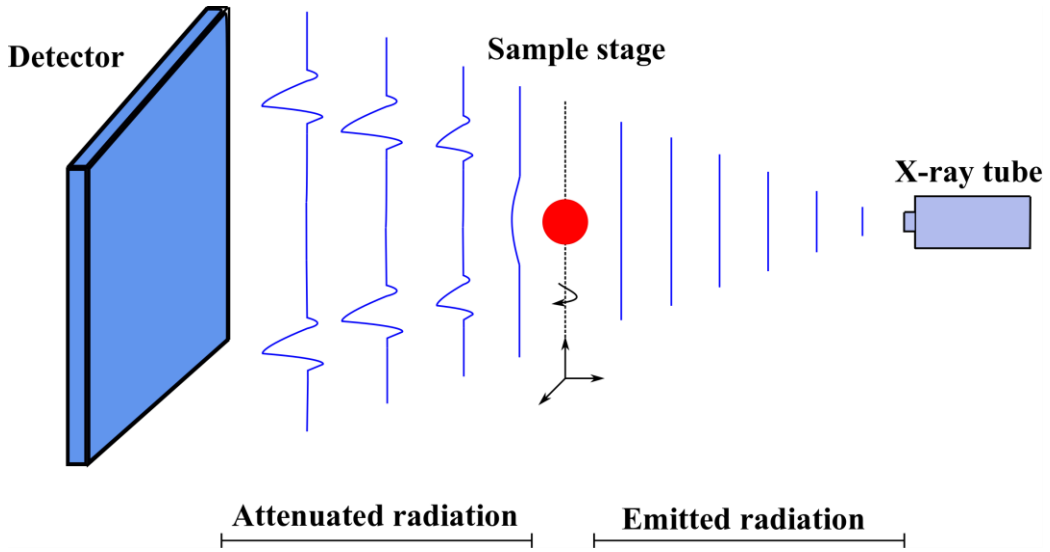

Figure 2. 7. Schematic diagram of x-ray tomography scan process.

2.4. Hyperelasticity

Hyperelasticity is a class of constitutive models that is used to characterize non-linear elastic materials. This type of models is relatively easy to calibrate and it can provide sufficient predictions of the mechanical behavior of soft materials. Hyperelastic models are suitable for large strain predictions and simple in representing materials' response that, in some cases, is related to the micromechanics of the soft materials' deformation behavior. This chapter addresses the stress expressions in terms of the elastic term of Helmholtz free energy in different loading conditions, hyperelastic models, and the viscoelastic response of the soft materials.

2.4.1. *Continuum Mechanics of Hyperelasticity*

In general, the expression of stresses in hyperelastic models is based on strain energy functions (the elastic term of Helmholtz free energy, W) (Lemaître, 2001). The general Cauchy stress is given by

$$\sigma(\mathbf{F}) = \frac{1}{\mathrm{J}} \frac{\partial \mathrm{W}(\mathbf{F})}{\partial \mathbf{F}} \mathbf{F}^{\mathrm{T}} \tag{2.1}$$

Where **F** is the deformation gradient, and J is the Jacobian determinant (J = det **F**).

To satisfy material frame indifference, the energy and the stress terms have to have the following forms

$$\boldsymbol{\sigma}(\mathbf{F}) = \mathbf{R}\, \boldsymbol{\sigma}(\mathbf{U})\, \mathbf{R}^{\mathrm{T}} = \mathbf{R}\, \boldsymbol{\sigma}(\mathbf{C})\, \mathbf{R}^{\mathrm{T}} \tag{2.2}$$

Where **R** is the rotational tensor, **U** is the right stretch tensor and **C** is Cauchy-Green tensor.

$$\mathbf{W(F)} = \mathbf{W(U)} = \mathbf{W(C)} \tag{2.3}$$

By substituting equations 2.2 and 2.3 into 2.1 gives

$$\boldsymbol{\sigma}(\mathbf{U}) = \mathbf{R}\left(\frac{1}{\mathrm{J}}\frac{\partial \mathrm{W}(\mathbf{U})}{\partial \mathbf{U}}\mathbf{U}^{\mathrm{T}}\right)\mathbf{R}^{\mathrm{T}} \tag{2.4}$$

The partial derivative of the energy term with respect of the right stretch tensor can transform into a partial derivative with respect of the right Cauchy-Green tensor, see derivation in Appendix A:

$$\frac{\partial \mathrm{W}(\mathbf{U})}{\partial \mathbf{U}} = 2\mathbf{U}\,\frac{\partial \mathrm{W}(\mathbf{C})}{\partial \mathbf{C}} \tag{2.5}$$

Substituting 2.5 into 2.4 gives the expression of the Cauchy stress that satisfy material frame indifference:

$$\boldsymbol{\sigma}(\mathbf{C}) = \frac{2}{\mathrm{J}}\mathbf{F}\frac{\partial \mathrm{W}(\mathbf{C})}{\partial \mathbf{C}}\mathbf{F}^{\mathrm{T}} \tag{2.6}$$

In this study, the tested materials are considered isotropic, thus, it is convenient to express the energy term as a function of the invariants of the right Cauchy-Green tensor $I_1(\mathbf{C})$, $I_2(\mathbf{C})$ and $I_3(\mathbf{C})$ where

$$I_1 = \lambda_1^2 + \lambda_2^2 + \lambda_3^2 \tag{2.7}$$

$$I_2 = \lambda_1^2\,\lambda_2^2 + \lambda_2^2\,\lambda_3^2 + \lambda_3^2\,\lambda_1^2 \tag{2.8}$$

$$I_3 = \lambda_1^2\,\lambda_2^2\,\lambda_3^2 \tag{2.9}$$

By expressing the energy term as a function of the strain invariants, equation 2.6 becomes

$$\boldsymbol{\sigma}\left(\mathrm{I}_1,\mathrm{I}_2,\mathrm{I}_3\right) = \frac{2}{\mathrm{J}}\mathbf{F}\left[\frac{\partial \mathrm{W}}{\partial \mathrm{I}_1}\frac{\partial \mathrm{I}_1}{\partial \mathbf{C}} + \frac{\partial \mathrm{W}}{\partial \mathrm{I}_2}\frac{\partial \mathrm{I}_2}{\partial \mathbf{C}} + \frac{\partial \mathrm{W}}{\partial \mathrm{I}_3}\frac{\partial \mathrm{I}_3}{\partial \mathbf{C}}\right]\mathbf{F}^{\mathrm{T}} \tag{2.10}$$

Where

$$\frac{\partial \mathrm{I}_1}{\partial \mathbf{C}} = \frac{\partial \mathrm{tr}\mathbf{C}}{\partial \mathbf{C}} = \mathbf{I} \tag{2.11}$$

$$\frac{\partial \mathbf{I_2}}{\partial \mathbf{C}} = \frac{1}{2}\left(2\mathrm{tr}\mathbf{C}\,\mathbf{I} - \frac{\partial \mathbf{tr}(\mathbf{C^2})}{\partial \mathbf{C}}\right) = \mathrm{I}_1\mathbf{I} - \mathbf{C} \tag{2.12}$$

$$\frac{\partial \mathrm{I}_3}{\partial \mathbf{C}} = \mathrm{I}_3\mathbf{C}^{-1} \tag{2.13}$$

$\mathbf{C} = \mathbf{F}\,\mathbf{F}^{T,}$ and the left Cauchy-Green tensor $\mathbf{B} = \mathbf{F}^{T}\,\mathbf{F}$. For isotropic materials $\mathbf{F} = \mathbf{F}^{T}$, thus, by inserting 2.11, 2.12 and 2.13 into 2.10 gives:

$$\boldsymbol{\sigma}(I_{1,}I_{2,}I_{3}) = \frac{2}{J}\left(\frac{\partial W}{\partial I_1} + I_1\frac{\partial W}{\partial I_2}\right)\mathbf{B} - \frac{2}{J}\frac{\partial W}{\partial I_2}\mathbf{B}^2 + \frac{2}{J}I_3\frac{\partial W}{\partial I_3}\,\mathbf{I} \qquad \textbf{(}2.14)$$

$I_3(\mathbf{F})$ Often expressed as J (Holzapfel, 2000), as will be demonstrated in chapter 3, thus equation 2.15 can be written as

$$\boldsymbol{\sigma}(I_{1,}I_{2,}J) = \frac{2}{J}\left(\frac{\partial W}{\partial I_1} + I_1\frac{\partial W}{\partial I_2}\right)\mathbf{B} - \frac{2}{J}\frac{\partial W}{\partial I_2}\mathbf{B}^2 + \frac{\partial W}{\partial J}\,\mathbf{I} \qquad (2.15)$$

Most hyperelastic models are based on the decomposition of the deformation gradient into deviatoric ($\bar{.}$) and volumetric components:

$$\mathbf{F} = J^{1/3}\,\overline{\mathbf{F}} \qquad (2.16)$$

$$\mathbf{C} = J^{2/3}\,\overline{\mathbf{C}} \qquad (2.17)$$

Similarly,

$$I_1 = J^{2/3}\,\bar{I}_1 \qquad (2.18)$$

$$I_2 = J^{4/3}\,\bar{I}_2 \qquad (2.19)$$

Using the energy term as a function of the deviatoric invariants transfer equation 2.15 into

$$\boldsymbol{\sigma}(\bar{I}_1,\bar{I}_2,J) = \frac{2}{J}\left(\frac{\partial W}{\partial \bar{I}_1}\frac{\partial \bar{I}_1}{\partial I_1} + J^{2/3}\bar{I}_1\frac{\partial W}{\partial \bar{I}_2}\frac{\partial \bar{I}_2}{\partial I_2}\right)\mathbf{B} - \frac{2}{J}\frac{\partial W}{\partial \bar{I}_2}\frac{\partial \bar{I}_2}{\partial I_2}\mathbf{B}^2 + \left(\frac{\partial W}{\partial \bar{I}_1}\frac{\partial \bar{I}_1}{\partial J} + \frac{\partial W}{\partial \bar{I}_2}\frac{\partial \bar{I}_2}{\partial J} + \frac{\partial W}{\partial J}\right)\mathbf{I} \qquad (2.20)$$

Inserting equations 2.18 and 2.19 into 2.20 gives

$$\boldsymbol{\sigma} = \frac{2}{J}\left(\frac{\partial W}{\partial \bar{I}_1} + \bar{I}_1\frac{\partial W}{\partial \bar{I}_2}\right)\mathbf{B} - \frac{2}{J}\frac{\partial W}{\partial \bar{I}_2}\mathbf{B}^2 + \left(\frac{\partial W}{\partial J} - \frac{2\bar{I}_1}{3J}\frac{\partial W}{\partial \bar{I}_1} - \frac{4\bar{I}_2}{3J}\frac{\partial W}{\partial \bar{I}_2}\right)\mathbf{I} \qquad (2.21)$$

For an incompressible isotropic material, equation 2.21 reduces to

$$\boldsymbol{\sigma} = 2\left(\frac{\partial W}{\partial \bar{I}_1} + \bar{I}_1\frac{\partial W}{\partial \bar{I}_2}\right)\mathbf{B} - \frac{2}{J}\frac{\partial W}{\partial \bar{I}_2}\mathbf{B}^2 + p\,\mathbf{I} \qquad (2.22)$$

Some hyperelastic models are based on the principal stretches ($\lambda_1, \lambda_{2,}\lambda_3$), thus, it is convenient to express the energy term as a function of these stretches $W(\lambda_1, \lambda_{2,}\lambda_3)$. In this case, the Cauchy stress can be given as

$$\sigma_i(\lambda_1, \lambda_2, \lambda_3) = \sum_{j=1}^{3} \frac{2}{J} \lambda_i^2 \frac{\partial W}{\partial \lambda_j} \frac{\partial \lambda_j}{\partial C_{ii}} \tag{2.23}$$

Since $\frac{\partial \lambda_j}{\partial C_{ii}} = \frac{\partial W}{2\lambda_i}$, equation 2.23 becomes

$$\sigma_i(\lambda_1, \lambda_2, \lambda_3) = \frac{\lambda_i}{J} \frac{\partial W}{\partial \lambda_i} \tag{2.24}$$

The complete form of Cauchy stress can be expressed as

$$\boldsymbol{\sigma} = \sum_{i=1}^{3} \frac{\lambda_i}{J} \frac{\partial W(\lambda_1, \lambda_2, \lambda_3)}{\partial \lambda_i} \hat{\mathbf{n}}_i \otimes \hat{\mathbf{n}}_i \tag{2.25}$$

Where $\hat{\mathbf{n}}_i$ are the principal directions of the left Cauchy-Green tensor **B**

2.4.2 *Hyperelastic models*

In literature, there are numerous hyperelastic models proposed to characterize the hyperelastic response of soft materials. In this study, three well known models are implemented: Yeoh model, Arruda-Boyce model and Ogden model. The choice of these particular models was based on several parameters that are common in most hyperelastic models: (i) phenomenological nature (Yeoh and Ogden), (ii) micromechanical nature (Arruda-Boyce), (iii) dependency on strain invariants (Yeoh and Arruda-Boyce), (iv) dependency on principal stretches (Ogden), (v) availability in most FE solvers, and (vi) ability to capture non-linear response of soft materials in different loading conditions (uniaxial stretch, biaxial stretch, and pure shear).

- **Yeoh model**

The Yeoh model (Yeoh, 1993) is based on the first strain invariant (I_1). For a compressible material, the model is expressed as

$$W(C_{10}, C_{20}, C_{30}, K) = C_{10}(\bar{I}_1 - 3) + C_{20}(\bar{I}_1 - 3)^2 + C_{30}(\bar{I}_1 - 3)^3 + \frac{K}{2}(J-1)^2 \tag{2.26}$$

While C_{10}, C_{20} and C_{30} are the material parameters of the deviatoric term, K is the bulk modulus of the material. It is also worth mentioning that the volumetric deformation is sometimes represented by higher order terms as demonstrated in chapter 3.

Due to the weak dependency of the Helmholtz free energy on the second strain invariant (I_2) for most elastomers (Bergstrom, 2015; Kaliske & Rothert, 1997; Kawabata et al., 1995; Yeoh, 1993), in addition to the difficulty of measuring this dependency experimentally, Yeoh, 1993 suggested

to ignore the I_2 in his model. For an incompressible material, the Cauchy stress for uniaxial, biaxial, and planar deformations can be given as

$$\sigma_{uni}= 2 [C_{10} + 2C_{20}(\bar{I}_1 - 3) + 3C_{30}(\bar{I}_1 - 3)^2] (\lambda^2 - \lambda^{-1}) \quad (2.27)$$

$$\sigma_{bi}= 2 [C_{10} + 2C_{20}(\bar{I}_1 - 3) + 3C_{30}(\bar{I}_1 - 3)^2] (\lambda^2 - \lambda^{-4}) \quad (2.28)$$

$$\sigma_{pl}= 2 [C_{10} + 2C_{20}(\bar{I}_1 - 3) + 3C_{30}(\bar{I}_1 - 3)^2] (\lambda^2 - \lambda^{-2}) \quad (2.29)$$

The accuracy of the Yeoh model in characterizing the material behavior is demonstrated in Figure 2.8 The model is used to predict Treloar data (Treloar, 1944, 2005). The model showed excellent potential in predicting the rubber mechanical behavior in different loading modes with $R^2 > 0.995$ for all three scenarios of loadings.

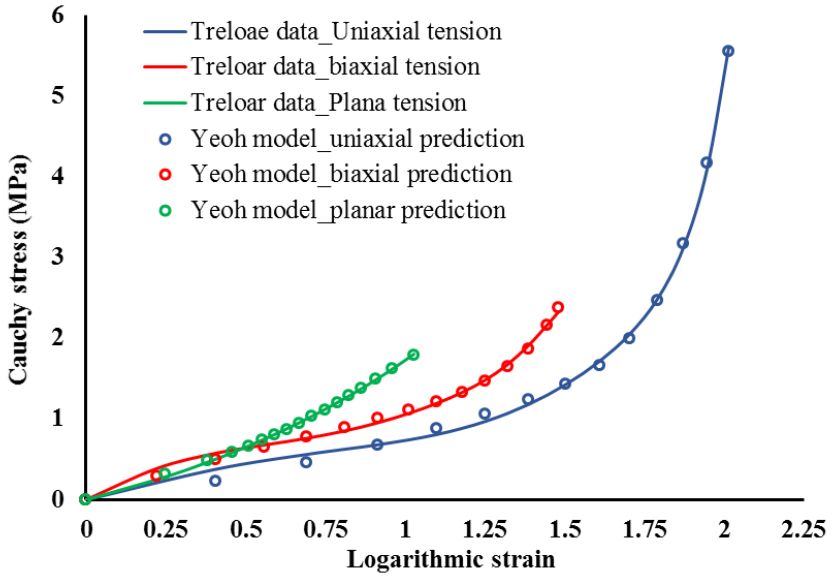

Figure 2. 8. Comparison between Treloar data and the prediction of incompressible Yeoh model.

- **Arruda-Boyce model**

This model is also known as the eight-chain model (Arruda & Boyce, 1993). The model describes the micromechanical behavior of materials. It is based on a cell unit that has eight diagonal molecular chains. The cell unit is located in a principal stretch space as demonstrated in Figure 2.9.

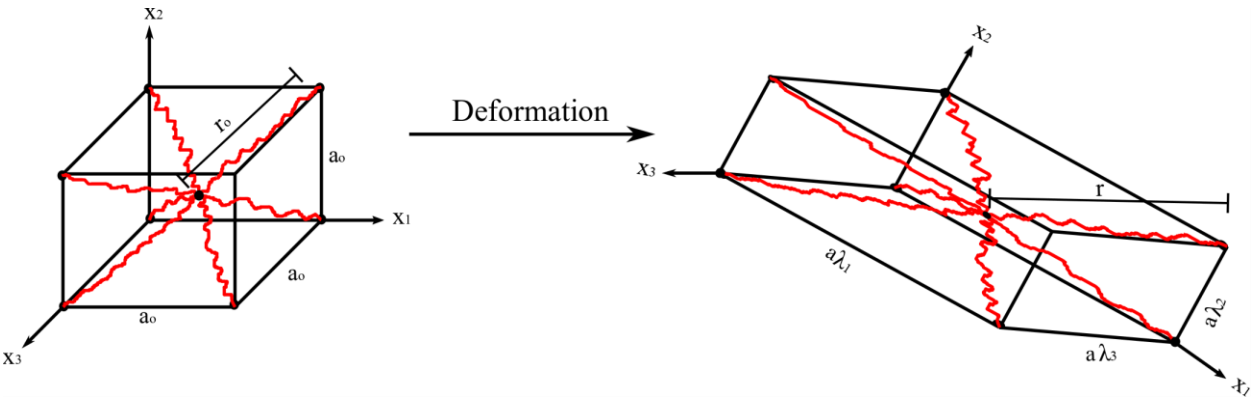

Figure 2. 9. Arruda-Boyce model: undeformed and deformed configurations.

The initial chain length is given as $r_0 = \sqrt{N}l$ (Arruda & Boyce, 1993; Flory & Volkenstein, 1969). For a fully extended chain length, $r_l = Nl$, where N is the number of the rigid links of the unit cell that has an equal length (l), and thus, the locking stretch (extensibility limiter) becomes

$$\lambda_m = \frac{r_l}{r_0}\sqrt{N} \tag{2.30}$$

The general form of Arruda-Boyce model of an incompressible material can be expressed as

$$W = \mu\left[\frac{\bar{I}_1-3}{2} + \frac{\bar{I}_1^{\,2}-9}{20N} + \frac{11(\bar{I}_1^{\,3}-27)}{1050N^2} + \frac{19(\bar{I}_1^{\,4}-81)}{7000N^3} + \frac{519(\bar{I}_1^{\,5}-243)}{673750N^4}\right] + \frac{K}{2}\left(\frac{J^2-1}{2} - \ln J\right) \tag{2.31}$$

Where μ represents the initial shear modulus.

For an incompressible material, the Cauchy stress for uniaxial, biaxial and planar deformations is given as

$$\sigma_{uni} = 2\mu\left[\frac{1}{2} + \frac{2\bar{I}_1}{20N} + \frac{33\bar{I}_1^{\,2}}{1050N^2} + \frac{76\bar{I}_1^{\,3}}{7000N^3} + \frac{2595\bar{I}_1^{\,4}}{673750N^4}\right]\left(\lambda^2 - \lambda^{-1}\right) \tag{2.32}$$

$$\sigma_{bi} = 2\mu\left[\frac{1}{2} + \frac{2\bar{I}_1}{20N} + \frac{33\bar{I}_1^{\,2}}{1050N^2} + \frac{76\bar{I}_1^{\,3}}{7000N^3} + \frac{2595\bar{I}_1^{\,4}}{673750N^4}\right]\left(\lambda^2 - \lambda^{-4}\right) \tag{2.33}$$

$$\sigma_{pl} = 2\mu\left[\frac{1}{2} + \frac{2\bar{I}_1}{20N} + \frac{33\bar{I}_1^{\,2}}{1050N^2} + \frac{76\bar{I}_1^{\,3}}{7000N^3} + \frac{2595\bar{I}_1^{\,4}}{673750N^4}\right]\left(\lambda^2 - \lambda^{-2}\right) \tag{2.34}$$

The accuracy of Arruda-Boyce model in predicting material non-linear elastic behavior is shown in Figure 2.10.

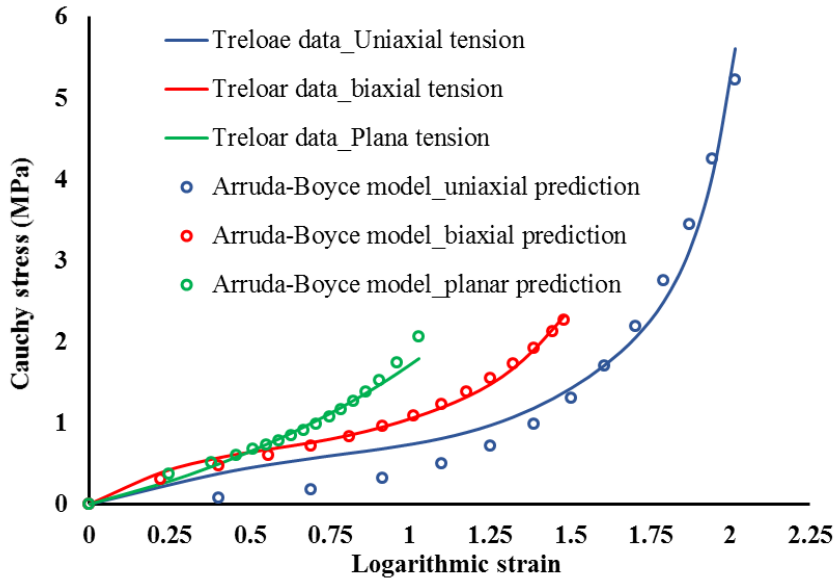

Figure 2. 10. Comparison between Treloar data and the prediction of incompressible Arruda-Boyce model.

The model showed very good potential in predicting the rubber mechanical behavior in different loading modes with R^2 >0.97 for all three scenarios of loadings.

- **Ogden model**

The Ogden model (Ogden, 1997) is a general hyperelastic model that is expressed in terms of the principal stretches. The model can be expressed in several formats; one popular format in literature is given as

$$W(\bar{\lambda}_1, \bar{\lambda}_2, \bar{\lambda}_3) = \sum_{i=1}^{n=3} \frac{2\mu_i}{\alpha_i^2} (\bar{\lambda}_1^{\alpha_i} + \bar{\lambda}_2^{\alpha_i} + \bar{\lambda}_3^{\alpha_i} - 3) + \sum_{i=1}^{n=3} \frac{K}{2} (J-1)^{2i} \quad (2.35)$$

Although this format is potent, it makes the selection of material parameters for stable prediction a complex process (Bergstrom, 2015). The general forms of Cauchy stress in the three loading scenarios for an incompressible material are expressed as

$$\sigma_{uni} = \sum_{i=1}^{n=3} \frac{2\mu_i}{\alpha_i} (\lambda^{\alpha_i} - \lambda^{-0.5\alpha_i}) \quad (2.36)$$

$$\sigma_{bi} = \sum_{i=1}^{n=3} \frac{2\mu_i}{\alpha_i} (\lambda^{\alpha_i} - \lambda^{-2\alpha_i}) \quad (2.37)$$

$$\sigma_{pl} = \sum_{i=1}^{n=3} \frac{2\mu_i}{\alpha_i} (\lambda^{\alpha_i} - \lambda^{-\alpha_i}) \quad (2.38)$$

The accuracy of the Ogden model in predicting material non-linear elastic behavior is shown in Figure 2.11.

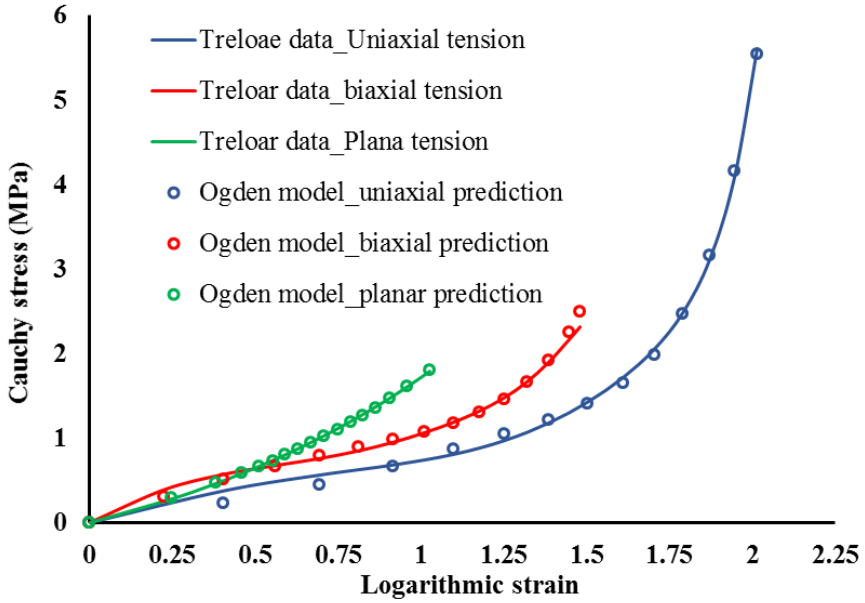

Figure 2. 11. Comparison between Treloar data and the prediction of incompressible Ogden model.

The model showed excellent potential in predicting the rubber mechanical behavior in different loading modes with R^2 >0.998 for all three scenarios of loadings.

2.5. Viscoelasticity

Polymeric gels and biological tissues are known for their viscoelastic behavior. This behavior is a combination of the elastic and viscous natures of these materials. The simplest method to model this combination is by using linear viscoelasticity theory. This modelling framework has been extensively studied for many years (Christensen, 2014; Ogden, 1997; Shaw, 2018).

Linear viscoelasticity is based on Boltzmann's super position principal, which is used to form an integral equation. The general form of an isotropic linear viscoelastic material can be expressed as

$$\sigma(t) = \int_{-\infty}^{t} E_R(t-\tau)\frac{d\varepsilon(\tau)}{d(\tau)}d(\tau) \tag{2.39}$$

By using integration by parts, equation 2.39 becomes

$$\sigma(t) = E_0\varepsilon(t) - \int_0^t \dot{g}_R(t-\tau)\, E_0\varepsilon(\tau)d(\tau) \tag{2.40}$$

Where g_R is the normalized relaxation modulus and expressed as

$$g_R = \frac{E_R(t)}{E_0} \tag{2.41}$$

The first term of equation 2.40 represents the material's elastic response, and the second term represents its viscous response.

In this study, the linear viscoelasticity is used to model large deformations, which are an inherent mechanical feature of rubber-like materials; therefore, hyperelastic stress function can be used instead of the linear elastic term in equation 2.40:

$$\sigma(t) = \sigma_{h.el}(\varepsilon(t)) - \int_0^t \dot{g}_R(t-\tau)\, \sigma_{h.el}(\varepsilon(\tau))d(\tau) \tag{2.42}$$

In cases where conventional techniques such as those used to obtain Treloar data, the material's non-linear elastic response can be characterized by fitting equations 2.27 – 2.29, 2.32 – 2.34 and 2.36 – 2.38 for Yeoh, Arruda-Boyce and Ogden hyperelastic models, respectively. In this study however, the hyperelastic response of the materials under cavity loads will be characterized in the polar coordinate system using a different analytical framework that will be introduced in chapter 3. The viscous response of equation 2.42 is expressed as Prony series and can be estimated by fitting to traditional relaxation data as will be demonstrated in chapter 6.

The viscous term of equation 2.42 can be implemented numerically as follows:

1. For simplicity, consider a conventional loading scenario of an incompressible material
2. At time (t), equation 2.42 represents the stress status. At time (t+Δt)

$$\sigma(t+\Delta t) = \sigma_{h.el}(\varepsilon(t+\Delta t)) - \int_0^{t+\Delta t} \dot{g}_R(t+\Delta t-\tau)\, \sigma_{h.el}(\varepsilon(\tau))d(\tau) \tag{2.43}$$

$$\Rightarrow \quad \sigma(t+\Delta t) = \sigma_{h.el}\big(\varepsilon(t+\Delta t)\big) - \sum_{i=1}^{N} \sigma_v^i(t+\Delta t) \tag{2.44}$$

where σ_v is viscos stress of Prony series term "i"

3. Expanding the viscos stress gives

$$\sigma_v^i(t+\Delta t) = \int_0^t \frac{d((1-g_i)+g_i e^{-\frac{t+\Delta t-\tau}{\hat{\tau}_i}})}{d\tau}\, \sigma_{h.el}(\tau)d\tau + \int_t^{t+\Delta t} \frac{d((1-g_i)+g_i e^{-\frac{t+\Delta t-\tau}{\hat{\tau}_i}})}{d\tau}\, \sigma_{h.el}(\tau)d\tau \tag{2.45}$$

$$\Rightarrow \quad \sigma_v^i(t+\Delta t) = \sigma_{v1} + \sigma_{v2} \tag{2.46}$$

Where g_i are dimensionless shear moduli at different relaxation times (Mills, 2007).

4. σ_{v1} can also be expressed as

$$\sigma_{v1} = \int_0^t \frac{g_i}{\hat{\tau}_i}\left(e^{-\frac{t}{\hat{\tau}_i}} . e^{-\frac{\Delta t}{\hat{\tau}_i}} . e^{\frac{\tau}{\hat{\tau}_i}}\right) \sigma_{h.el}(\tau)d\tau \quad (2.47)$$

$$= \quad e^{-\frac{\Delta t}{\hat{\tau}_i}} \sigma_v^i(t) \quad (2.48)$$

5. Assuming linear relationship between $\sigma_{h.el}(\tau)$ and $\boldsymbol{\tau}$ gives:

$$\sigma_{h.el}(\tau) = \sigma_{h.el}(t) + \Delta\sigma_{h.el} \frac{\tau - t}{\Delta t} \quad (2.49)$$

Where

$$\Delta\sigma_{h.el} = \sigma_{h.el}(\varepsilon(t + \Delta t)) - \sigma_{h.el}(\varepsilon(t)) \quad (2.50)$$

Thus, a closed form solution for σ_{v2} can be given as

$$\sigma_{v2} = g_i\sigma_{h.el}(t)\left(1 - e^{-\Delta t/\hat{\tau}_i}\right) + g_i \frac{\Delta\sigma_{h.el}}{\Delta t}((\Delta t - \hat{\tau}_i) + \hat{\tau}_i e^{-\Delta t/\hat{\tau}_i}) \quad (2.51)$$

Substituting 2.47 and 2.51 into 2.46 gives

$$\sigma_v^i(t + \Delta t) = e^{-\frac{\Delta t}{\hat{\tau}_i}} \sigma_v^i(t) + g_i\sigma_{h.el}(t)\left(1 - e^{-\Delta t/\hat{\tau}_i}\right) + g_i \frac{\Delta\sigma_{h.el}}{\Delta t}((\Delta t - \hat{\tau}_i) + \hat{\tau}_i e^{-\Delta t/\hat{\tau}_i}) \quad (2.52)$$

Equation 2.52 can be substituted into equation 2.44 to simulate the total response of the linear viscoelastic materials with large deformations. A demonstration of this analytical solution is presented by using Matlab code in Appendix C.

This chapter introduced the experimental and analytical fundamentals that are going to be used in the following chapters. The cavity expansion test is going to be used in chapters 3, 4, 5, and 6. The compressibility test is going to be used in chapter 3 to measure the compressibility of PVA hydrogels. The uniaxial tension test will be used to measure the mechanical properties of PVA hydrogels in axial loading in chapter 5. The simple shear test will be used in chapter 6 to measure the viscous response of PVA hydrogels. The CT imaging is going to be used in chapters 3 and 4 to characterize the cavity configuration visually.

Chapter 3

Measuring Hyperelastic Properties of Hydrogels Using Cavity Expansion Method

Abstract

Numerous methods have been proposed to measure the mechanical properties of hyperelastic materials such as hydrogels. Common techniques, such as tension, compression, and indentation tests, experience various challenges due to material structure and surface conditions. These challenges affect the measured mechanical properties of the tested material. Therefore, a new technique is proposed to measure the hyperelastic mechanical properties of hydrogels by introducing cavity deformations to the internal solid structure of hydrogels. The data obtained from the cavity test were analyzed mathematically by using three strain energy functions and then were validated numerically through FE simulations. Computed Tomography (CT) imaging was implemented to investigate the shape of the cavities, which showed that the proposed technique is capable of applying controlled spherical deformations. The stresses in the cavity test were generated in the radial and hoop directions; therefore, the validation process took into consideration both types of stresses. The numerical simulations considered the two common views about hyperelastic materials: slightly compressible and incompressible. A comparison between experimental results and FE simulations of the cavity test has shown a good agreement in pressure-deformation data.

3.1. Introduction

Hydrogels have been used in a wide range of biomedical applications including catheter coating (Yang et al., 2007), contact lenses (Hu et al., 2011), wound dressing (Corkhill et al., 1989), and drug delivery (Lin & Anseth, 2009). Their popularity in the medical field is related to the biocompatible nature of hydrogels due to their high water content (Oyen, 2014). They respond elastically to very large deformations (up to 700% strain), and they exhibit a non-linear stress-strain relationship. The broad range of applications of hydrogels and other similar materials rationalize the extensive research conducted to study their mechanical behavior using experiments, and to characterize their response through the development of a number of constitutive models.

Numerous techniques have been implemented to investigate the mechanical response of rubber-like materials; perhaps the most common are compression, tension, and indentation. These techniques are based on measuring deformations while monitoring the corresponding loads to measure the mechanical properties of materials, or vice versa. The analysis in tension and compression is based on the assumption of uniformly distributed stresses on a volume equivalent to the product of the gage length and the cross-sectional area. However, in the indention test, the load is more localized, and the mechanical response of the materials depends fundamentally on the geometry of the indenter (Oyen, 2011).

Tension can be applied in many states. A uniaxial state to measure the mechanics of isotropic materials; plane state to investigate the materials' behavior in pure shear; and multi-axial state (equi-biaxial) to investigate the behavior of anisotropic materials (Jacobs et al., 2013b; Mitchell et al., 2007). In compression, the state of loading is uniaxial; however, the material state can be unconfined or confined. In the former, the material is compressed between two non-porous platens (Roberts et al., 2011); while in the latter, the sample is compressed in a confined container with porous platens (Gu et al., 2003). In indentation, the state of loads can be perceived as a "*local version*" of compression test (Oyen, 2014). Indentation is becoming more popular in testing hydrogels because samples require minimal preparations for testing compared to relatively complex cutting/machining into specific shapes (dumbbell/dog-bone) used in tension. In addition, it is very easy to keep the sample moist throughout the test.

Although compression, tension and indentation tests are effective in studying material behavior, complications might arise during the loading process. For example, in tensile testing, the gripping strategies are prone to daunting challenges such as slippage and stress concentrations. The effect of the slipping and related gripping problems lies in its potential to significantly affect material behavior represented by the force vs displacement (Soden & Kershaw, 1974). Similarly, in compression tests, friction between the surface of the sample and the testing rig can cause non-uniform stress distribution along the gauge length of the material (Blake, 1985). On the other hand, indentation eliminates these challenges, and can be more suitable for testing rubber-like material properties, especially in cases where local heterogeneities are the focus of investigation (Oyen, 2011). However, numerous challenges arise when applying indentation to measure the mechanics of a material, which include, dependence on the substrate's stiffness in the case of thin samples

(Doerner & Nix, 1986; Nix, 1989); indentation size effect (Burnett & Rickerby, 1987; Farges & Degout, 1989); surface roughness (Menčík & Swain, 1995); and piling up of the tested material around the indenter (Stone et al., 1988).

The main goal of this work is to measure the mechanical response of hydrogels by applying internal deformations in a form of spherical cavity to eliminate complications and challenges that normally accompany conventional techniques. The material used in this work is PVA hydrogels; these hydrogels are known for their nonlinear elastic response under loading (tension (Wan et al., 2002), compression (Li et al., 2016), and indentation (Lin et al., 2009), in addition to their slight compressibility (Chen et al., 2013). The types of stresses generated in expanding cavities are radial and hoop stresses. Accordingly, cavity expansion technique can provide a perspective about the material response to pressure and stretching simultaneously. The analytical work in this paper is based on spherical internal cavity assumption, which is verified using Computed Tomography (CT) imaging.

The paper presents the method of analysis and material models. Material processing conditions, details of the mechanical tests, and CT imaging are also described, in addition to numerical simulations generated by Abaqus® based on the material parameters evaluated using experimental tests for each of the material models.

3.2. Basic Equations

3.2.1. *Preliminaries*

Here the Lagrangian frame of reference to describe deformations is considered. A position vector **X** is defined for a material point in a reference configuration β_o. When loads are applied, the position vector of the material point changes to indicate a new position **x= f(X)** in the deformed configuration β. In this state, the deformation gradient tensor can be defined as

$$\mathbf{F} = \text{Grad}\mathbf{x} \tag{3.1}$$

Where Grad is the gradient with respect to **X**, i.e,

$$F_{ij} = \frac{\partial x_i}{\partial X_j} \tag{3.2}$$

Where x_i and X_j are **x** and **X** components, respectively, and i and j $\in \{1, 2, 3\}$. The deformation gradient **F** is diagonal and associated with the principal stretches λ_1, λ_2, and λ_3.

By using polar decomposition, **F** can be decomposed into

$$\mathbf{F} = \mathbf{R}\,\mathbf{U} = \mathbf{V}\,\mathbf{R} \quad (3.3)$$

Where **U** and **V** are the right and left stretch tensors, respectively. They are symmetric and positive definite. **R** is an orthogonal tensor. Also,

$$\mathbf{U}^2 = \mathbf{C} = \mathbf{F}^{\mathrm{T}}\mathbf{F}, \text{ and } \mathbf{V}^2 = \mathbf{B} = \mathbf{F}\mathbf{F}^{\mathrm{T}} \quad (3.4)$$

Where **C** and **B** are the left and right Cauchy-Green deformation tensors.

The characterization of isotropic hyperelastic materials is done through strain-energy density function W. The energy function W is normally defined by two principal strain invariants I_1, and I_2, i.e., $W = W(I_1, I_2)$.

According to Ogden, 1997, the strain invariants I_1, I_2, and I_3 are defined as

$$I_1 = \mathrm{tr}C = \lambda_1^2 + \lambda_2^2 + \lambda_3^2 \quad (3.5)$$

$$I_2 = \frac{1}{2}[(\mathrm{tr}C)^2 - \mathrm{tr}(C^2)] = \lambda_1^2\lambda_2^2 + \lambda_2^2\lambda_3^2 + \lambda_3^2\lambda_1^2 \quad (3.6)$$

$$I_3 = \det C = \lambda_1^2\lambda_2^2\lambda_3^2 = 1 \quad (3.7)$$

The Cauchy stress as a function of the deformation gradient takes the form

$$\boldsymbol{\sigma} = \mathbf{F}\,\frac{\partial W}{\partial F} - p\mathbf{I} \quad (3.8)$$

Where **σ** is the deviatoric stress, the first term represents the stress, the right term represents the hydrostatic stress, and **I** is the identity tensor. By deriving the strain invariants with respect to **F** (see appendix A), equation 3.8 becomes

$$\boldsymbol{\sigma} = 2(W_1 + I_1 W_2)\mathbf{B} - 2W_2\mathbf{B}^2 - p\mathbf{I} \quad (3.9)$$

Where W_1 and W_2 are the derivatives with respect to I_1 and I_2, respectively.

3.2.2. *Cavity Expansion*

Theoretical considerations of the existing void growth expansion in rubber-like materials can be found in (deBotton et al., 2013; Faye et al., 2017; Fond, 2001; Lev & Volokh, 2016; J. Li et al., 2007). Below, we follow the work of (deBotton et al., 2013). To describe the kinematics of spherical cavity expansion in isotropic hyperelastic materials, consider a thick-walled sphere with inner and outer radii of r_i and r_o, respectively, subjected to an external pressure (P_0) and an internal pressure (P_i). It is more convenient to use the polar coordinate system (R, Θ, Φ) in the reference configuration β_o, where

$$r_i \le R \le r_o,\ 0 \le \Theta \le \Pi,\ 0 \le \Phi \le 2\Pi \quad (3.10)$$

When pressure P_i is applied on the inner surface, $R = r_i$, an expansion occurs and denoted in the current configuration as

$$a \leq r \leq b,\ 0 \leq \theta \leq \pi,\ 0 \leq \varphi \leq 2\pi \tag{3.11}$$

Where (r, θ, φ) are the polar coordinates in the deformed configuration; *a* and *b* are the inner and outer radii of the deformed geometry.

The principal stretches in the polar coordinates are defined as

$$\lambda_1 = \frac{dr}{dR} = \lambda^{-2},\ \lambda_2 = \lambda_3 = \frac{r}{R} = \lambda \geq 1 \tag{3.12}$$

By combining equation 3.12 into 3.5 and 3.6

$$I_1 = 2\lambda^2 + \lambda^{-4},\ I_2 = 2\lambda^{-2} + \lambda^4 \tag{3.13}$$

The components of the stress can be defined by using equation 3.9

$$\sigma_r = 2[W_1\lambda^{-4} + 2W_2\lambda^{-2}] - p \tag{3.14}$$

$$\sigma_\theta = 2[W_1\lambda^2 + W_2(\lambda^4 + \lambda^{-2})] - p \tag{3.15}$$

Where σ_r and σ_θ are the stresses in the radial and tangential directions.

The equilibrium equation of the cavity expansion in terms of these stresses is (deBotton et al., 2013)

$$r\frac{d\sigma_r}{dr} + 2(\sigma_r - \sigma_\theta) = 0 \tag{3.16}$$

Since W_1 and W_2 are defined in terms of I_1, and I_2, respectively, and the strain invariants are defined in terms of λ, it is convenient to define $\widehat{W}$ in terms of λ.

$$\widehat{W} = \frac{dW(I_1,I_2)}{d\lambda} = 4W_1(\lambda - \lambda^{-5}) + 4W_2(\lambda^3 - \lambda^{-3}) \tag{3.17}$$

By combining equations 3.14, 3.15, 3.16, and 3.17 we can define a relationship between the applied pressure and the resulted deformation in a hyperelastic material as

$$P_i = \int_{\lambda_b}^{\lambda_a} \frac{\widehat{W}d\lambda}{(\lambda^3 - 1)} \tag{3.18}$$

Equation 3.18 defines the internal pressure at the cavity wall in terms of the stretch at *a* (λ_a) or equivalently at *b* (λ_b). This equation will be adopted to enable the strain energy functions listed below to capture the hyperelastic mechanical behavior of PVA hydrogels based on the pressure readings. The derivation of equation 3.18 considers the material as incompressible; therefore, it is worth mentioning that the stretch term (λ) in this equation is equivalent to the incompressible stretch term ($\bar{\lambda}$) in the next section.

3.2.3. *Strain Energy Functions*

An efficient hyperelastic model should be able to represent material behavior independently of deformation mode. In this work, three SEFs (Ogden, Yeoh, and Arruda-Boyce) are used based on

their efficiency of representing the behavior of hyperelastic materials in uniaxial, biaxial, and bulge stretching deformations (Sasso et al., 2008a; Shahzad et al., 2015).

- Ogden model

A phenomenological model proposed by Ogden, 1972. This model has been implemented to capture the deformation of rubbers (Sasso et al., 2008b), and biological tissues (Gao et al., 2010a).

$$W = \sum_{i=1}^{N=3} \frac{2\mu_i}{\alpha_i^2} \left(\bar{\lambda}_1^{\alpha_i} + \bar{\lambda}_2^{\alpha_i} + \bar{\lambda}_3^{\alpha_i} - 3\right) + \sum_{i=1}^{N=3} \frac{1}{D_i} (J-1)^{2i} \quad (3.19)$$

Where $\bar{\lambda}_i$ are the deviatoric principal stretches; μ_i and α_i are material constants; D_i are material constants define the bulk compressibility; J is a volume ratio.

- Yeoh model

This model is also phenomenological proposed by Yeoh, 1993, and it is based only on the first invariant I_1.

$$W = \sum_{i=1}^{N=3} C_{i0}(\bar{I}_1 - 3)^i + \sum_{i=1}^{N=3} \frac{1}{D_i}(J-1)^{2i} \quad (3.20)$$

C_{i0} are material constants.

- Arruda-Boyce model

This model is structural with parameters that have a physical link to the chain orientation involved in the network deformation of rubber (Hackett, 2016). It was proposed by Arruda and Boyce (Arruda & Boyce, 1993).

$$W = \mu \sum_{i=1}^{5} \frac{C_i}{\lambda_m^{2i-2}} (\bar{I}_1^i - 3^i) + \frac{1}{D}\left[\frac{J^2-1}{2} \ln(J)\right] \quad (3.21)$$

Where C_i are material constants; λ_m is the stretch at which the polymer chain network becomes locked; μ is the shear modulus.

3.3. Materials, Methods, and Imaging

3.3.1. *Sample Preparation*

To prepare PVA solutions, 99+% hydrolyzed PVA with a molecular weight (M_w) of 146000 - 186000 g•mol^{-1} was used. An 8% w/w PVA solution was prepared by heating and mixing with the use of standard flask/column combination. The solution was poured into cylindrical molds (50 mm in height and 36 mm in diameter) made of brass. The PVA solution in the molds was processed through Freeze-Thaw Cycles (FTC) between -20 ^{o}C and 20 ^{o}C by using ESPEC environmental chamber. A total of ten samples were created. The samples were divided into two batches (five in each batch) based on the number of freeze-thaw cycles. Each cycle represents freezing from 20 ^{o}C

to -20 ^{o}C at a rate of 0.2 ^{o}C/min, holding for 6 hours, then thawing to 20 ^{o}C at a rate of 0.2 ^{o}C/min, and holding for 6 hours. The crosslinking regime is summarized in table 3.1.

Table 3. 1. Crosslinking regime

	No. of cycles	Freezing rate (^{o}C/min)	Thawing rate (^{o}C/min)	Holding time (h) at -20 ^{o}C	Holding time at 20 ^{o}C
Batch 1	2	0.2	0.2	6	6
Batch 2	3	0.2	0.2	6	6

1 cycle = freeze from 20 ^{o}C temperature to -20 ^{o}C, hold for 6 hours, thaw to 20 ^{o}C, and then hold for 6 hours.

3.3.2. *Mechanical Testing*

This section describes the standard tests performed to measure the data required to evaluate the material constants for the strain energy functions.

- **Cavity Test**

The system consists of pressure gauge, pump, syringe, and balloon-on-needle components connected with a Y-shaped tube. A low durometer urethane balloon was used with a radius of 5 mm (Vention Medical Inc, USA), medical needle (0.7 mm x 40 mm), and a digital pressure gauge (model DG 25, Ashcroft Inc., USA). The end opening of the needle was sealed using epoxy to restrict water flow to the balloon through needle's side openings. Effort was made to ensure that there were no air bubbles trapped in the system; the tube, needle, and the pressure gauge inlet were injected individually with water accompanied by gentle tapping to ensure air is expelled out, then they were carefully connected together to ensure no air exists in the system. The test is based on inserting the needle inside the samples, then using the syringe pump to control the volume rate of injected water. Volume rate of 33 μl/sec was used. As the injected water volume increases, the observed pressure increases. The effect of needle insertion was neglected due to the low stresses and strains applied by the needle in addition to the soft nature of the hydrogel, this will be discussed in more details in section 6. The test was conducted at ambient conditions. At the early stage of the investigation, the gel samples were placed between two rigs to assure stability of the samples when water was injected. However, after further investigation, it was concluded that this step was not required because the effect of deformation did not reach the boundaries of the sample as it was absorbed within small thickness (2-4 mm) around the cavity. The test configuration is illustrated in Figure 3.1.

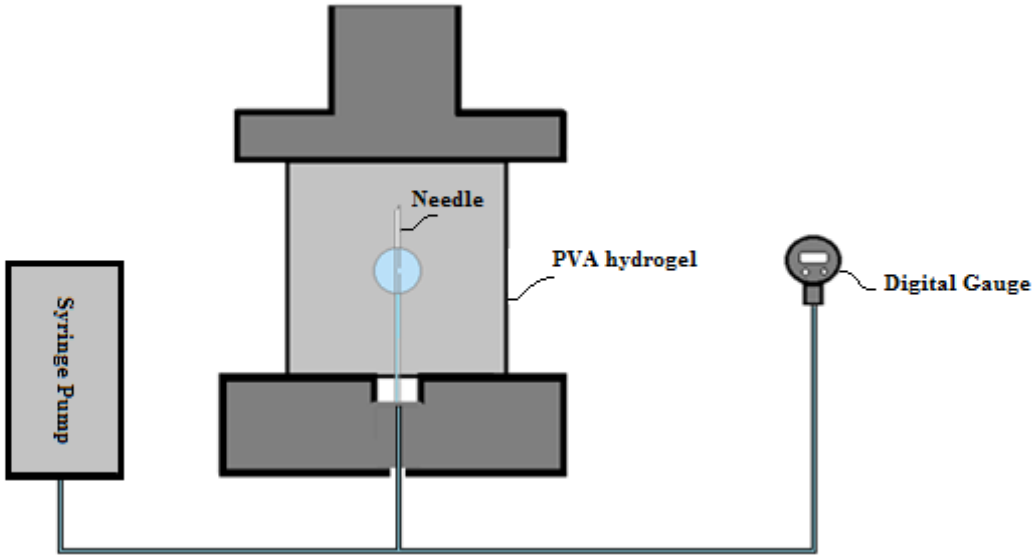

Figure 3. 1. Cavity test system.

- **Volumetric Test**

To investigate the compressibility of the gels, the samples were compressed in a confined configuration, as shown in Figure 3.2. The compression fixture used in this test consists of a special cylindrical mold, machined with an internal diameter that fits the samples and a thickness of 4 mm to provide rigid confinement, and a non-porous metal punch. A 10 mm gap is provided at the top of the fixture to guide the punch. The punch was machined to fit within the diameter of the mold and with similar diameter to that of the gel samples. Instron loading machine (model 4465; Canton, MA, USA) equipped with 5 kN load cell was used to compress the samples. The hydrostatic term in the equations 3.19, 3.20, and 3.21 was derived with respect to "J", and the outcome was fitted to the experimental data using least squares method.

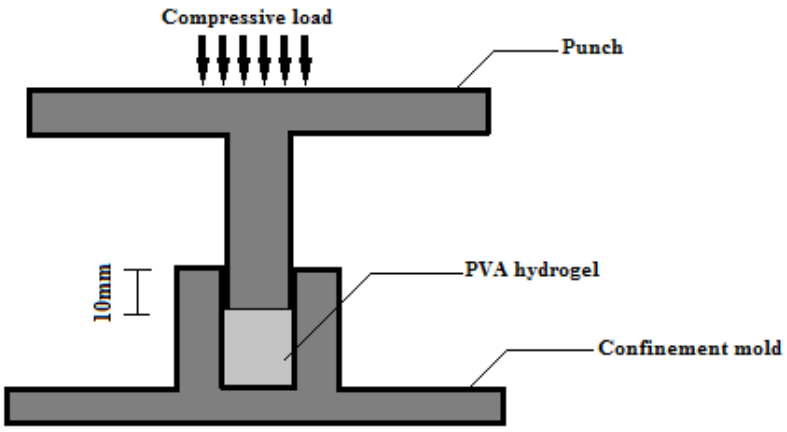

Figure 3. 2. Volumetric test fixture.

- **Sample Imaging**

The micro-focus CT-scans were performed with x-ray inspection system, Phoenix v|tome|x s (General Electeric Sensing and Inspection Technologies, Germany) equipped with a 240 kV micro-focus x-ray tube and a 2048 x 2048 pixels flat panel detector.

The imaging work was performed on the stiffer batch of samples, i.e., 3 FTC. Three samples were scanned, and they were injected with different volumes of 150 µl, 300 µl, and 450 µl. The process was based on inserting the needle-balloon tool from the top of each sample; for convenience, the geometric center of the top surface area was chosen to insert the needle-balloon tool. The balloon was assumed to behave in a similar manner at different locations in the samples due to the isotropy of PVA hydrogels. Then, the balloon was filled with an iodine-based contrast agent made by dissolving Sodium Iodide (NaI) into distilled water at room temperature with a concentration of 0.5 g/ml. The scan parameters applied to all specimens can be found in table 3.2.

Table 3. 2. CT scan parameters.

Acceleration voltage (kV)	Beam Current (µA)	Exposure Time (ms)	Number of projections	Voxel Size $(\mu m)^3$	Scan time (min)	Cu pre-filter (mm)
150	150	333	1000	74.06	22	0.1

3.4. Experimental Results and Analysis

3.4.1. *Experimental Data & Calibration of Constitutive Models*

Given the spherical shape of the balloon, the deformation was evaluated from the radius of the injected volumes. This assumption was adopted because the bulk modulus of water (2.15 GPa) is orders of magnitude higher than that of PVA hydrogels (shown in equation 3.23). This assumption was verified by the CT imaging as will be shown later. Three strain energy functions were used- equations 3.19, 3.20, and 3.21; their material constants were evaluated by the data fitting exercise in which the least squares method was implemented. Before performing the fitting process, equation 3.18 was derived using Leibniz's rule, and then the tangential outcome was used to fit the models with the experimental data. Figure 3 shows the fitted models. The stretch term λ was defined based on equation 3.12 in which R was defined as 0.45 mm (the radius of the needle, 0.35 mm, in addition to thickness of the balloon, 0.1 mm), and r was evaluated as follows:

$$r = \sqrt[3]{\frac{3V}{4\pi}} + 0.45 \qquad (3.22)$$

Where V is the injected volume of water.

The data fitting process is also used to evaluate the compressibility constants in each of the SEFs as shown in Figure 3.4. The material parameters from the cavity and volumetric tests are summarized in tables 3.3 to 3.6 using different energy functions.

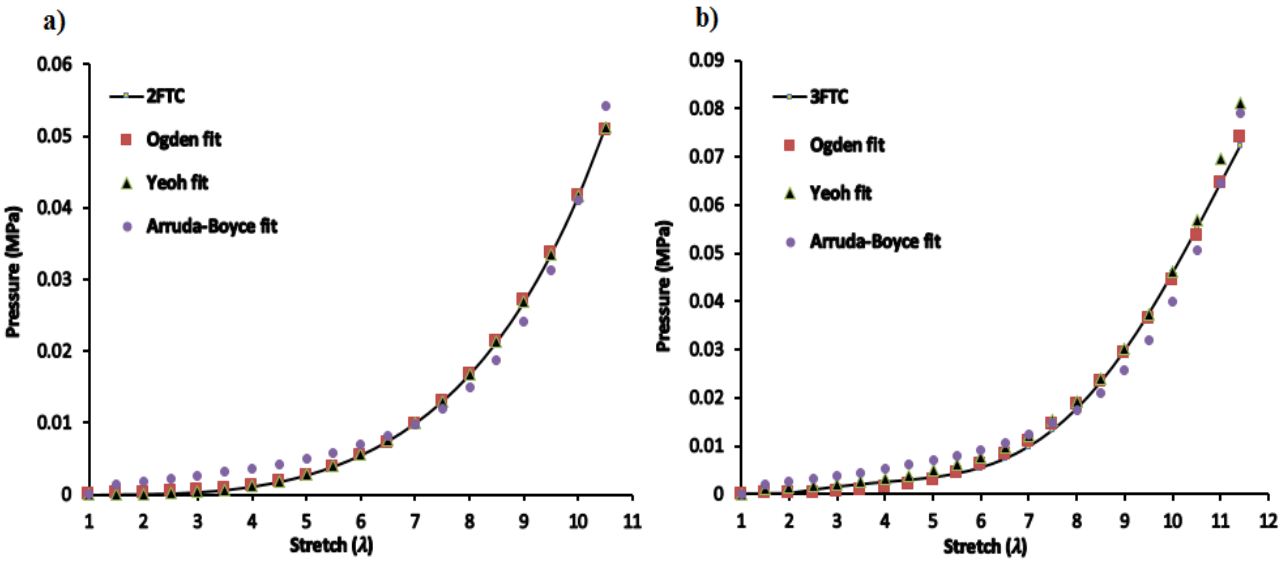

Figure 3. 3. Fitting of different hyperelastic models with cavity data using a) 2FTC and b) 3FTC hydrogels.

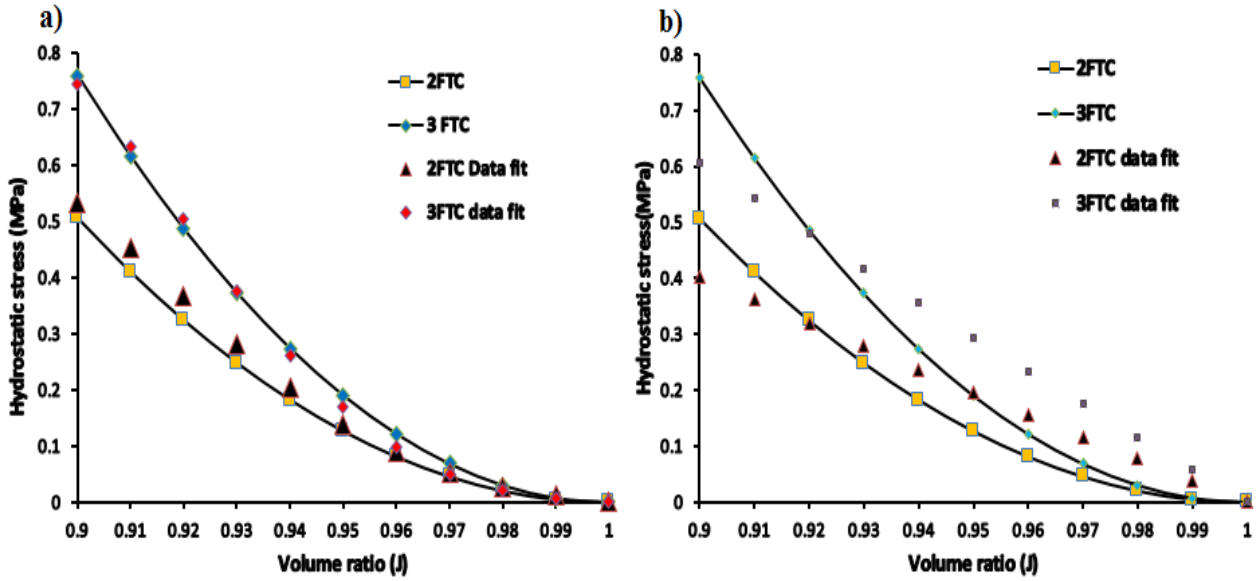

Figure 3. 4. Fitting of the volumetric test data. a) Ogden and Yeoh strain energy functions, b) Arruda-Boyce strain energy function.

Table 3. 3. Coefficients of Ogden, N=3, material model. μ_i are in MPa.

2FTC		3FTC	
μ_i	α_i	μ_i	α_i
1.02622e-02	3.551	1.0098e-02	3.552
-1.02051e-02	3.5622	-1.00831e-02	3.5572
3.7312e-05	4.7096	3.1383e-05	4.7042

Table 3. 4. Coefficients of Yeoh, material model. C_{i0} are in MPa

2FTC			3FTC		
C_{10}	C_{20}	C_{30}	C_{10}	C_{20}	C_{30}
8.658e-05	3.1556e-06	7.168e-09	1.127e-04	3.41e-06	7.65e-09

C_{i0} are in MPa.

Table 3. 5. Compressibility constants in Ogden and Yeoh strain energy functions. D_i are in MPa^{-1}

2FTC			3FTC		
D_1	D_2	D_3	D_1	D_2	D_3
2.818	5.27e-03	-1.785e-04	3.35	3.192e-03	-1.056e-04

Table 3. 6. Coefficients of Arruda-Boyce material model. μ is in MPa.

2FTC				3FTC			
μ	λ_m	μ_0	D	μ	λ_m	μ_0	D
8.53e-04	7.3107	8.62e-04	0.523	1.254e-03	8.09048	1.2658e-03	0.3487

The volumetric functions implemented in Yeoh and Ogden provided better fit to the volumetric test data than the function implemented in Arruda-Boyce because they use three terms, similar to the number of terms used in the hyperelastic functions, while in Arruda-Boyce, only one volumetric term was used. In general, the evaluation of the bulk modulus K is based on the following:

$$K = \frac{2}{D} \tag{3.23}$$

Based on equation 3.23, K can be calculated as 3.82 MPa and 5.74 MPa for 2 FTC and 3 FTC gels, respectively. These values are orders of magnitude less than the bulk modulus of water (2.15 GPa),

and thus the injected water is assumed to cause spherical deformation pattern with a radial displacement equivalent to

$$u = \sqrt[3]{\frac{3V}{4\pi}} \tag{3.24}$$

3.4.2. *Image Reconstruction*

After all two dimensional (2D) image projections were obtained, a three dimensional (3D) volume was constructed by using Volume Graphics (*Volumegraphics.com*). The 3D image visualizations of the hydrogel and the needle-balloon tool are shown in Figure 3.5 (a & b). A simple threshold function based on a gray value threshold allows for visualization of the balloon inside the specimens because the atoms of the contrast agent's chemical elements have a significantly higher atomic number than that of PVA.

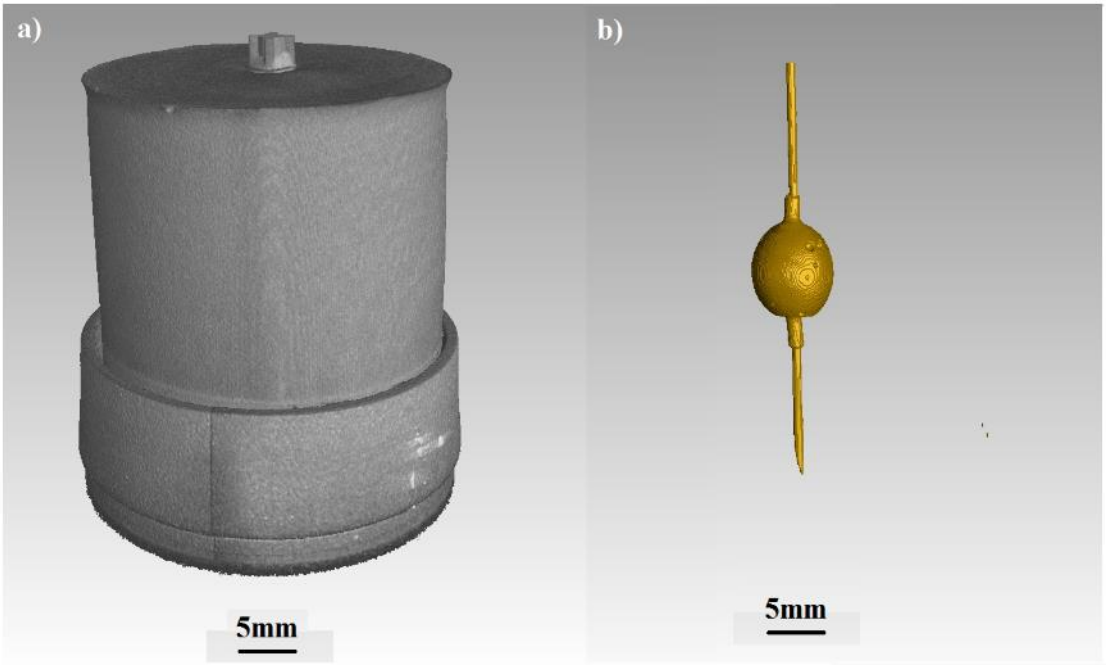

Figure 3. 5. Three-dimensional reconstruction of a hydrogel specimen injected with 450 µl of contrast agent. a) Hydrogel specimen; b) Inflated balloon.

Volume Graphics uses different algorithms to run inclusion analysis. As it can be observed from Figure 3.6, the overall shape of the filled balloon inside the hydrogels is spherical, and the calculated volumes by the algorithm match the injected ones. Figure 3.7c shows comparisons between the injected volumes (actual) and the calculated volumes. The "actual radius" showed in Figure 3.7b was based on calculating the average of the diameters measured by the "Distance" tool. Overall, the average difference between the actual radius and the nominal radius for all

injected volumes is 5%. At lower volumes, the balloon tends to deform in irregular spherical shape; however, as the volumes increase, the shape of deformations follows a uniform spherical configuration. The results presented by Volume Graphics offer a substantial validation to the assumption of spherical configuration of the internal deformations.

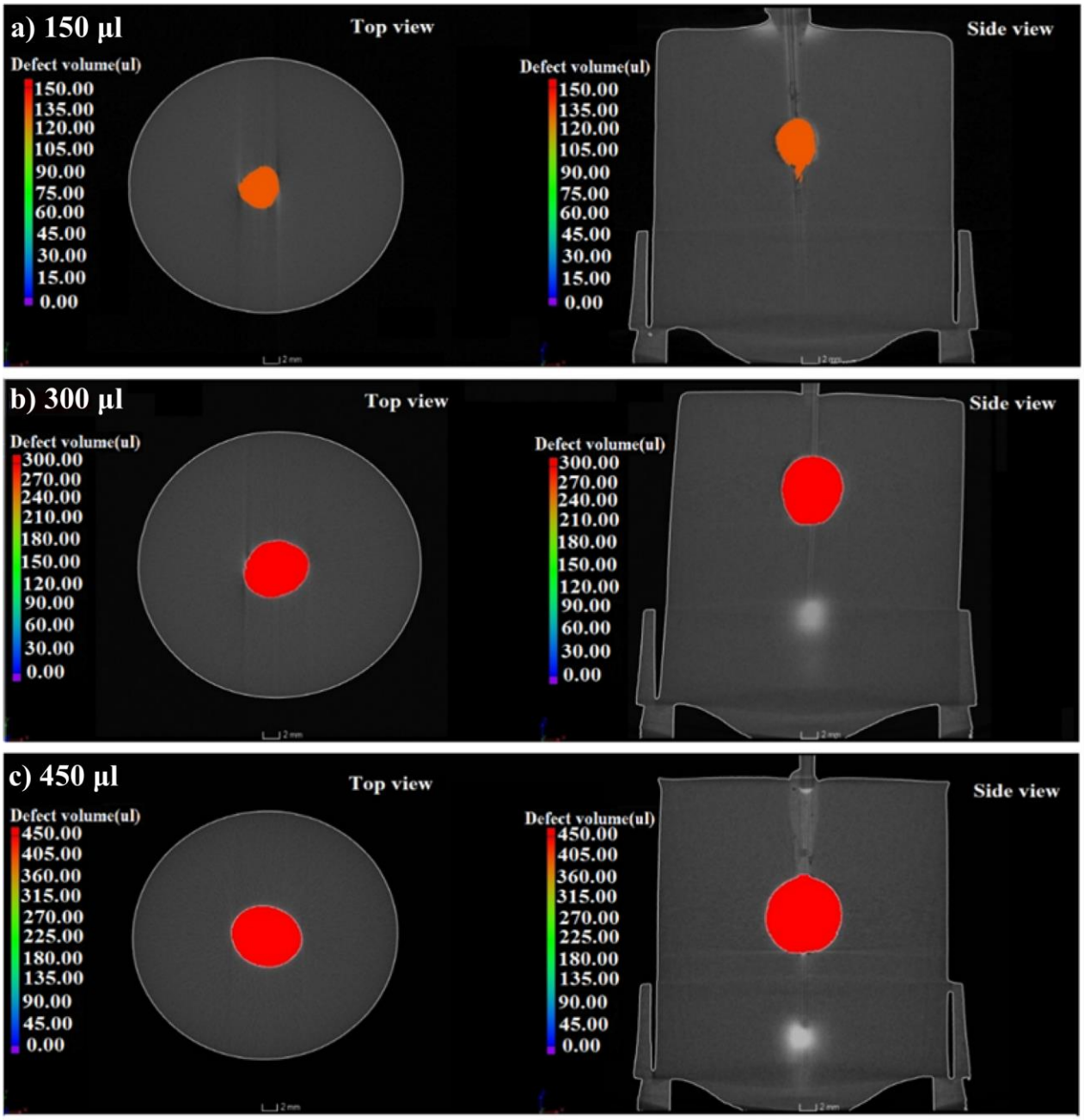

Figure 3. 6. Calculating the volume of the inflated balloon inside the hydrogel specimens. a) 150 µl; b) 300 µl; c) 450 µl.

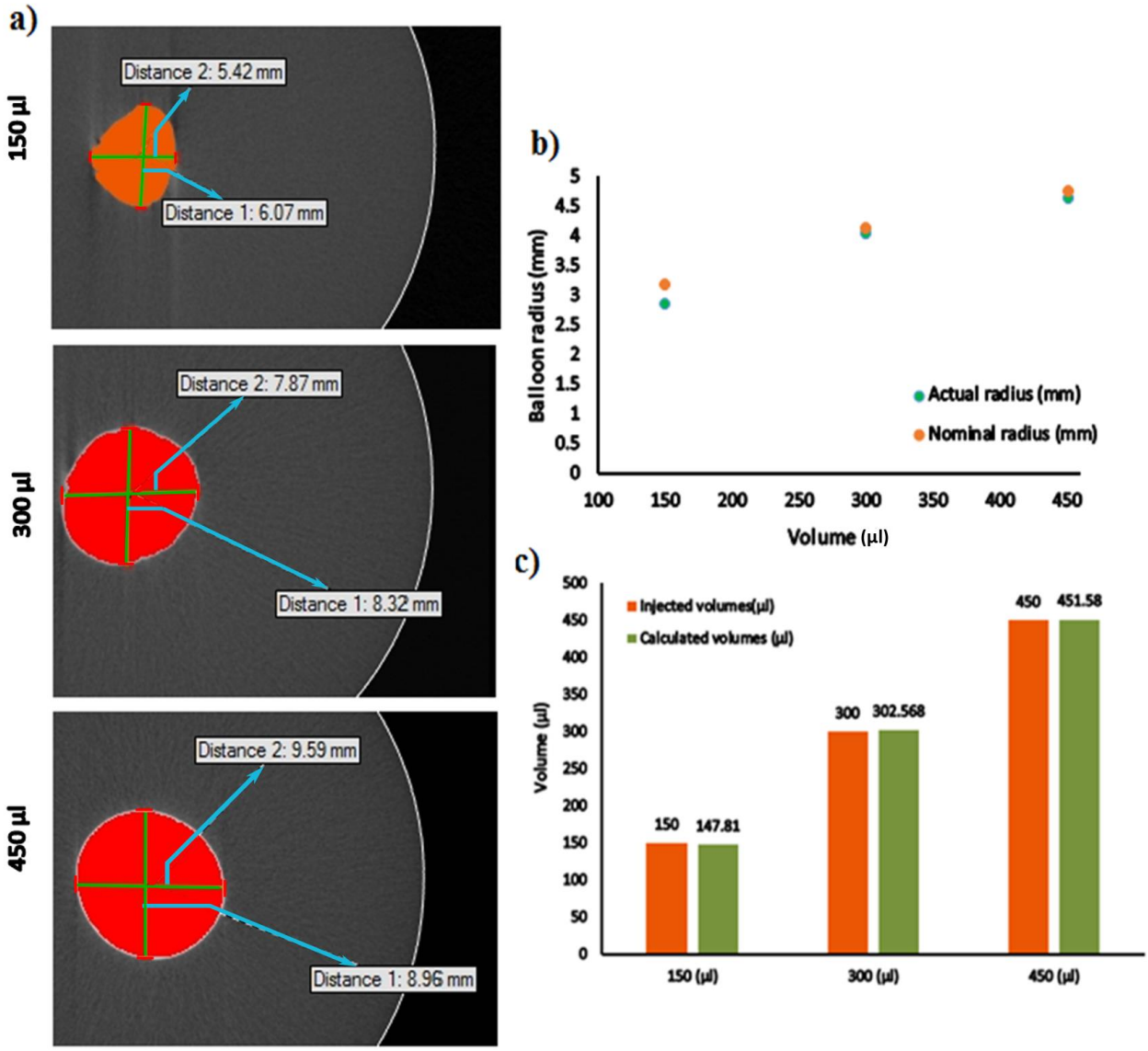

Figure 3. 7. a) Measuring the actual diameter (image based) in 2D scene; b) comparison between the actual radius measured by the "Distance" tool in Volume Graphics and the nominal radius at each applied volume, distances 1 and 2 represent the vertical and horizontal dimensions of the expanded cavity, respectively; and c) comparison between injected volumes and the volumes calculated by the "Only threshold" algorithm.

3.5. Numerical Model

To validate the material constants evaluated from the data fitting, the cavity expansion test was simulated using Abaqus® (ABAQUS/CAE, 2013). An axisymmetric, quadrilateral, and hybrid elements (CAX4H, in Abaqus notation) are used in the numerical simulation. The mesh was created in a radial direction as shown in Figure 3.8. The model was structured to be axisymmetric, and half of the specimen was analyzed. A convergence study has been performed in which stress

outputs, namely the radial stress and hoop stress, at the cavity wall (nodes) were compared against the mesh density until the stress values satisfactorily converged. The elements' size is constant along the circumference and decreases in the radial direction towards the cavity wall. The size of the elements at the circumference is 97 μm x 55 μm, and 2 μm x 55 μm at the cavity wall. The magnitude order of the elements' size is similar to a numerical investigation of spherical cavity expansion in rubber-like materials reported in (Faye et al., 2017). The numerical model dimensions are 40 mm in height and 18 mm in width. These dimensions represent the height and the radius of the PVA hydrogels, respectively. The radial displacement obtained from the cavity test, which matched the nominal displacement according to the CT-imaging investigation, was applied from an initial cavity of 0.45 mm in radius. The boundary conditions (BCs) applied in the simulation resemble those in the cavity test; during the test, the samples were confined at the top and bottom to avoid any movement that could occur during balloon inflation as shown in Figure 3.9a; therefore, a pin constraint was applied on the top and on the bottom of the FE model. In addition, the hydrogel was constrained from moving horizontally along the symmetry axis. The circumference of the model was left with no constraint, as the samples were not confined laterally during the test. BCs are presented in Figure 3.9b.

3.6. FE Simulation Results and Discussion

Before considering the material parameters obtained from the test data as valid representatives of hydrogels behavior, it is necessary to further validate those parameters; one of the common techniques for validation is by modelling the material parameters in different FE solvers. This technique provides a numerical application of the calibrated models. Agreement between the numerical simulation and the experimental data indicates the validity of the material models used in this work (Yeoh, Arruda-Boyce, and Ogden), thus confirms the capability of the cavity expansion test to measure the mechanical behavior of PVA hydrogels. This process has been adopted for tensile (uniaxial and biaxial), and bulge tests (Charlton et al., 1994; Mohan et al., 2011; Sasso et al., 2008a). The general theme of the validation process is based on applying the radial displacement into the FE model, then observing the simulated stresses on the cavity wall of the model. In the hyperelastic solution, the radial displacement is extracted from the injected volumes of water. Equation 3.18 relates the applied pressure to deformation (λ) which enables SEFs to capture the behavior of the hydrogels based on the data obtained from the cavity test.

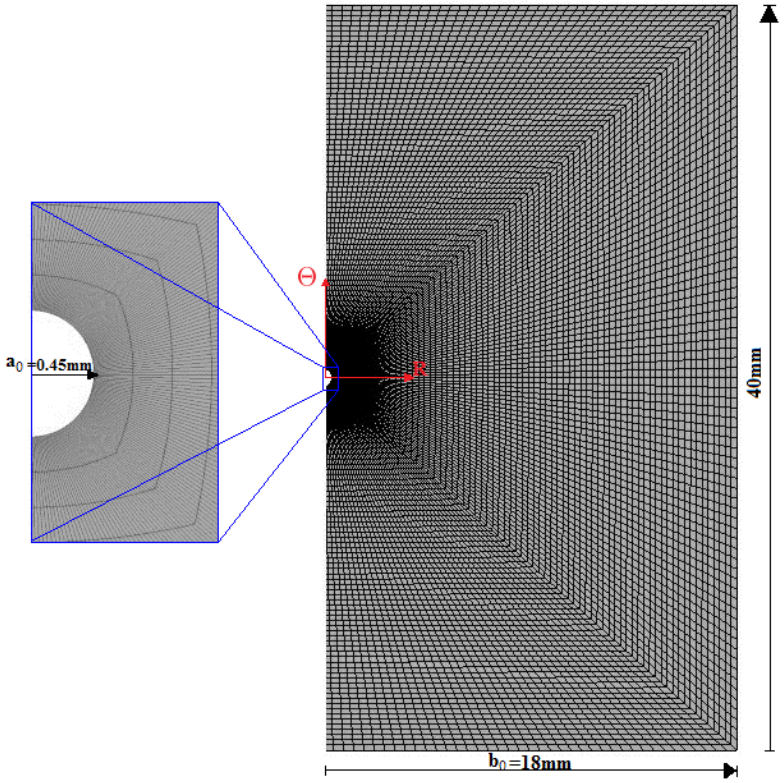

Figure 3. 8. Axisymmetric finite element model developed to analyze spherical cavity expansion.

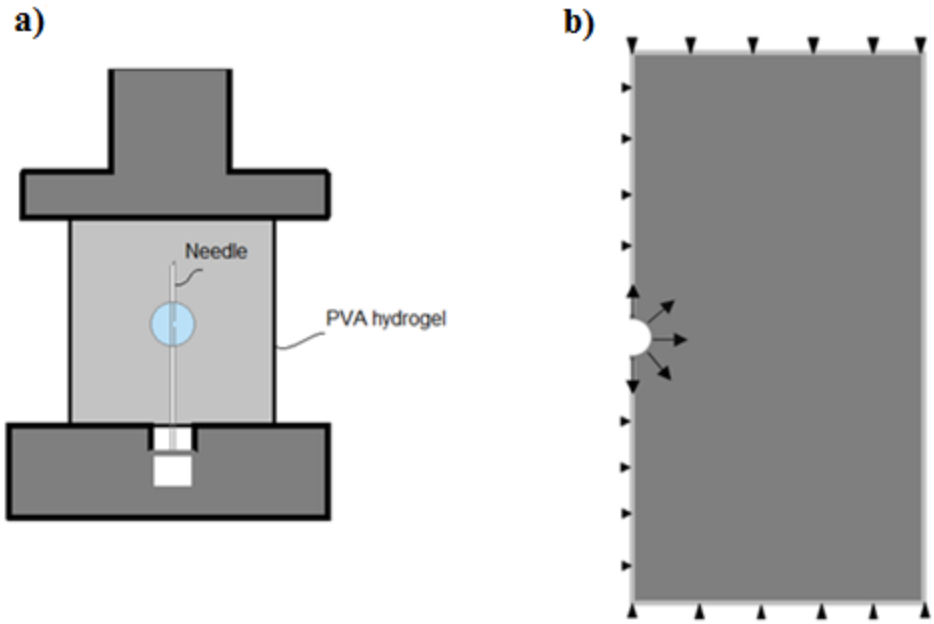

Figure 3. 9. a) Configuration of the cavity test. b) Boundary conditions in the FE model (symmetric plane boundary conditions are applied at left vertical side of the model which include restrictions to horizontal translation and rotations.

The data fitting was conducted using equation 3.18 to evaluate the material constants of the implemented SEFs. Afterwards, material constants were used in the numerical model. A comparison of experimental results with FE simulations of cavity test has shown a good agreement for pressure-deformation data as shown in Figure 3.10. The average root square error (RMS error) was calculated, as per equation 3.25, to measure the difference between the experimental data and the FE simulations; table 3.7 summarizes the difference between the experiment data and FE simulations for both batches of hydrogels. Overall, the three SEFs provided a good agreement with the experimental data. It is interesting to note that the experimental findings are slightly higher than the FE simulations' results.

$$\text{RMS Error} = \frac{1}{N}\sqrt{\sum_{i=1}^{N}\left(\frac{P_{exp}-P_{FE}}{P_{exp}}\right)} \tag{3.25}$$

Table 3. 7. Average RMS error for 2FTC & 3FTC hydrogel. Experimental data vs FE simulation.

2FTC			3FTC		
Ogden	**Yeoh**	**Arruda-Boyce**	**Ogden**	**Yeoh**	**Arruda-Boyce**
7.5%	7.73%	8.01%	6.75%	7.58%	7.65%

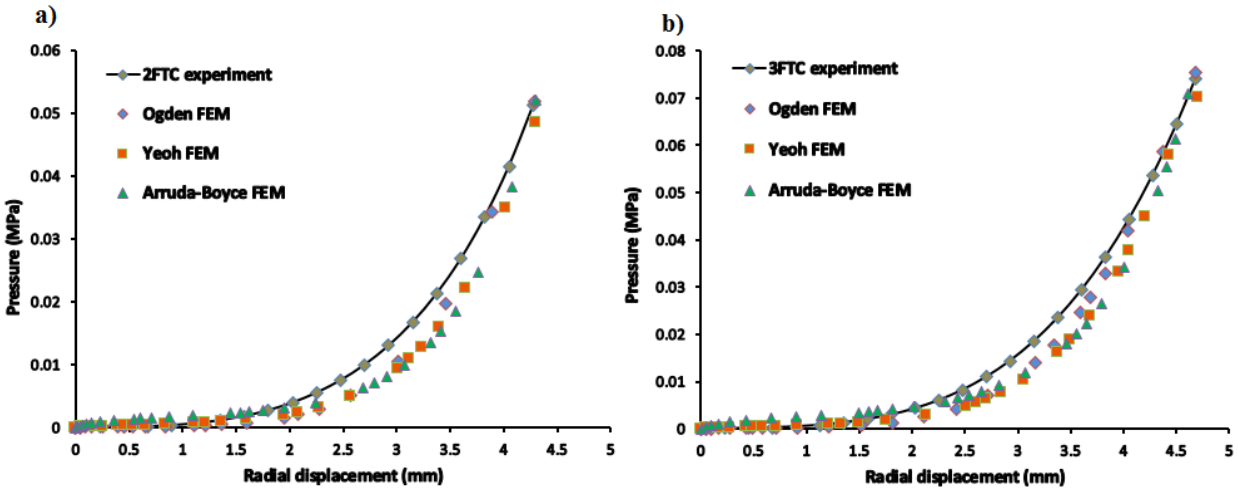

Figure 3. 10. A comparison of FE prediction and experimental data for cavity test. a) 2FTC; b) 3FTC.

To further validate the parameters obtained from the data fitting process, the hoop stresses generated in the cavity test are also compared against the numerical simulation. Equation 3.18 describes the material as incompressible; which is a common assumption for rubber-like materials (Agoras et al., 2009; Elshazly, 2004). PVA hydrogels was also considered as slightly compressible

elastomers with Poisson's ratio that ranges between 0.44 and 0.48 (Urayama et al., 1993) (Lee et al., 2013). Therefore, the mathematical solution was compared against both incompressible and compressible numerical simulations, as illustrated in Figures 3.11 and 3.12. The compressible simulation was conducted by considering D values obtained from the volumetric test in the numerical model. The incompressible simulation was conducted by considering very small D values [D_1 and D (Arruda-Boyce) = 1e-05, D_2= 0, and D_3= 0] to provide very high bulk modulus. In strain energy functions defined based on the strain invariants (Yeoh and Arruda-Boyce), the Cauchy hoop stress is defined mathematically by equation 3.15. On the other hand, Ogden strain function is defined based on the principal stretches, thus equation 3.8 was used to evaluate the Cauchy hoop stress. Equation 3.25 was also used to compare the difference between the mathematical analysis and FE simulation of the hoop stress. The analysis outcomes are summarized in table 3.8. Based on the comparison with the experimental data, in addition to the predictions of hoop stresses, it can be concluded that the material parameters of the adopted SEFs sufficiently represent the hydrogel response to the cavity deformations, and thus prove their capability to represent the hydrogel response under cavity deformations.

Table 3. 8. RMS error for 2FTC & 3FTC hydrogel. Hoop stress mathematical vs FE simulation.

2FTC	**Incompressible**	**Compressible**
Ogden	4.57%	6.92%
Yeoh	6.1%	8.84%
Arruda-Boyce	5.78%	8.67%
3FTC	**Incompressible**	**Compressible**
Ogden	4.73%	6.46%
Yeoh	5.98%	8.75%
Arruda-Boyce	5.63%	8.71%

In this study, it is assumed that any residual stresses due to needle insertion have been dissipated; this assumption was adopted mainly due to low stresses applied by the needle during the insertion process compared to the applied pressure as a result of the soft nature of the hydrogel in addition to the relatively small size of the needle. Similar outcomes were observed by Leibinger et al., 2016 who reported that the peak effective strain resulted on the gel material surrounding the needle was in the range of 10 % - 14 %. This is relatively very low strain when it is compared with the applied strains presented in this study, in which, the peak effective strains due to the cavity expansion were

470% and 486% for 2 FTC and 3 FTC hydrogels, respectively. Therefore, the needle effect was considered insignificant and was neglected in the numerical simulations.

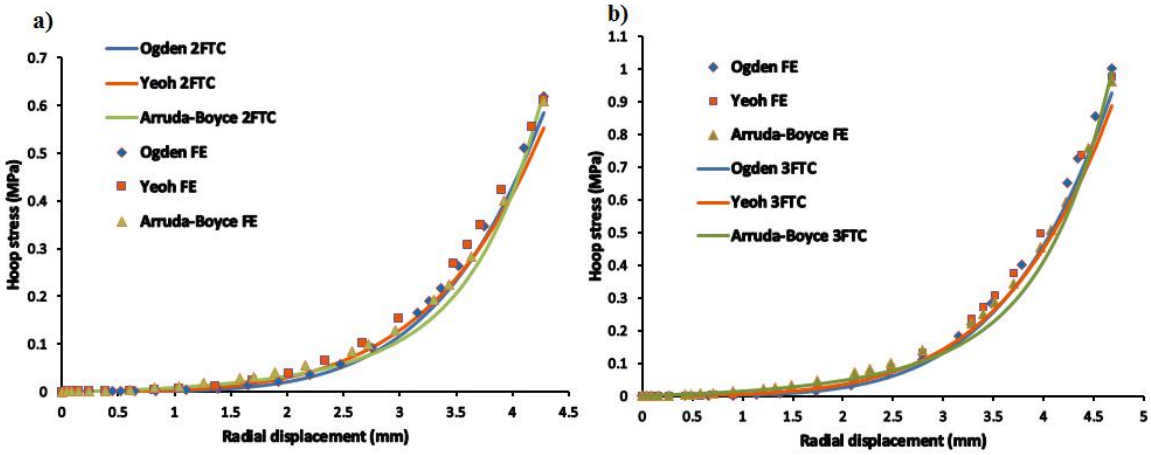

Figure 3. 11. A comparison of incompressible FE prediction with the mathematical prediction of the strain energy functions for a) 2FTC and b) 3FTC gels.

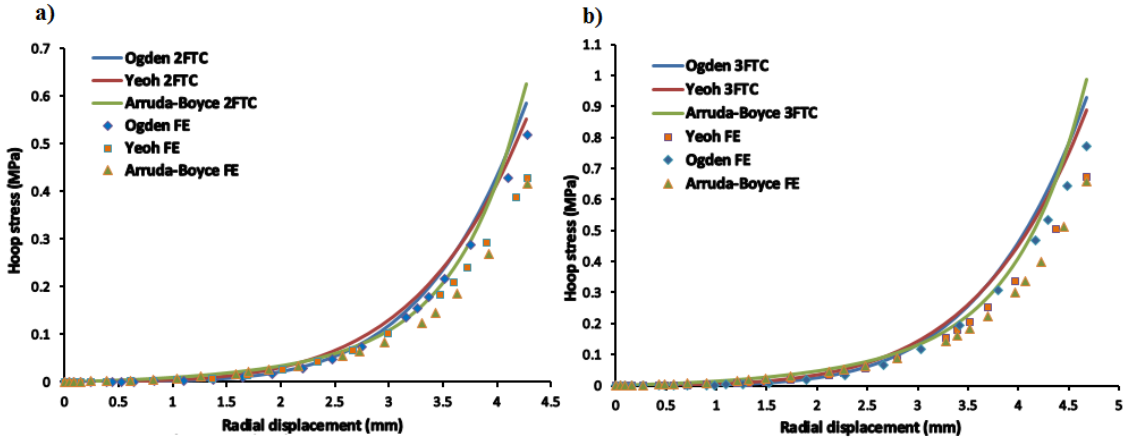

Figure 3. 12. A comparison of compressible FE prediction with the mathematical prediction of the strain energy functions for a) 2FTC and b) 3FTC gels.

Furthermore, similar investigations were performed on other types of soft materials, such as agarose gels (Urrea et al., 2016), and brain tissues (Casanova et al., 2014). These studies reported peak radial stresses of 0.6 kPa - 1.2 kPa, and 0.1 kPa - 0.3 kPa for agarose gels and brain tissues, respectively. The reported stresses are significantly lower than the radial stresses reported in this study due to cavity expansion; in the cavity test, the maximum pressures applied radially on the cavity wall were 55 kPa, and 75 kPa in 2 FTC and 3 FTC hydrogels, respectively. Therefore, these relatively very low strains and stresses generated due to needle insertion are significantly smaller than the ones generated during the cavity test and can be ignored.

The CT imaging indicated that the balloon usually expands in a regular spherical shape in most of the injected volumes except at low volumes, where the shape of the balloon deviates slightly from the regular spherical shape. However, it is still valid to consider the applied volume to be perfectly spherical, including at low volumes, as it does not influence the accuracy of determining the hyperelastic material parameters. To verify the accuracy of the obtained material parameters, a numerical simulation for an irregular cavity that had a starting shape of a square with circular edges was performed. The outcome of this simulation indicated that the behavior remains similar to the original spherical cavity, as shown in Figure 3.13. The results indicate that knowing the total volume of the cavity is sufficient to perform the fitting process.

Incompressibility of hydrogels is attributed to their high water content (Elshazly, 2004), but there is no experimental evidence that supports considering these materials as perfectly incompressible. Several methods have been proposed to consider the low compressibility of these materials, most prominently, the decomposition of the strain energy function into deviatoric and hydrostatic terms, which was implemented in this work. Although the decomposition is not physically realistic (Ní Annaidh et al., 2013), it works well with isotropic materials and mathematically convenient (Gilchrist et al., 2014) (Weiss et al., 1996), which makes the decomposition method an ideal analytical option. The incompressible simulation provided a very good agreement with the mathematical solution. In addition, the compressible simulation provided, to some extent, good agreement as well, which indicates that the small differences between the mathematical solution and numerical simulation are due to the slight compressibility of the hydrogels. Overall, both of compressible and incompressible simulations of PVA hydrogels provided relatively similar behavior. Based on the comparison outcomes, obtaining material parameters from the cavity expansion experiment can be considered valid for compressible and incompressible hyperelastic media.

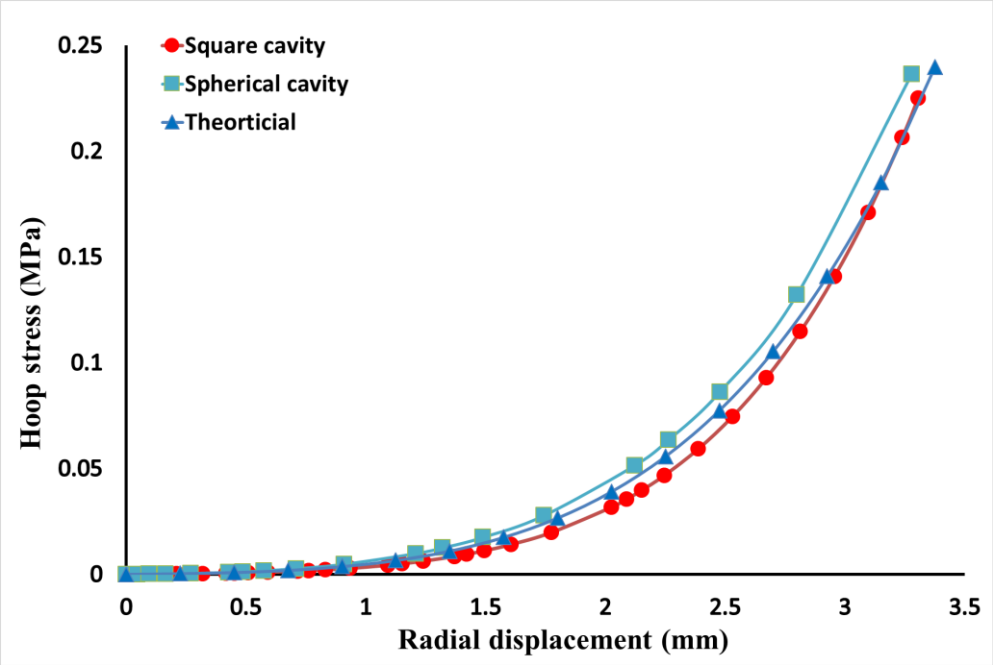

Figure 3. 13. A plot of Hoop stress versus the radial displacement. The radial displacements in this plot are obtained from injected volumes up to 150 µl.

3.7. Conclusion

In this work, experimental data obtained from a new technique that is based on expanding cavity deformations. The data was used to calibrate material constants of three SEFs (Yeoh, Ogden, and Arruda-Boyce). The material constants were input into Abaqus® to simulate the cavity test. Based on the RMS Error analysis, the SEFs provided an excellent prediction of the material response to cavity deformations. A direct comparison between the FE simulations and the experimental data have shown that the cavity expansion technique is a valid approach to measure the mechanical response of rubber-like materials such as PVA hydrogels. In addition, CT imaging was implemented to observe the deformations applied through the needle-balloon tool. The spherical shape of the internal deformations has shown the potential of using the needle-balloon tool to control the applied deformations. The balloon configuration at low volumes tend to deviate from a perfect spherical configuration; however, FE simulation of irregular cavity showed that the overall volume of the cavity is sufficient to evaluate the material parameters of the hyperelastic SEFs. In conclusion, considering the gels' response to balloon inflation is sufficient to study their mechanics under cavity deformations. Overall, the technique provided excellent means to measure the mechanics of hyperelastic materials without experiencing the conventional challenges that accompany common techniques.

Chapter 4

Measuring the Hyperelastic Response of Porcine Liver Tissues In-Vitro Using Controlled Cavitation Rheology

Abstract

Measuring the mechanical properties of biological tissues *in-vitro* by using conventional methods is prone to external testing and sample preparation factors. For example, sample slippage affects the measurement accuracy of mechanical properties of biological tissues. In addition, samples have to go through a complex cutting process to be prepared in specific shapes, which increases the post-mortem time spent before testing. The purpose of this study is to investigate the capability of a new technique to measure the mechanics of biological tissues without experiencing the conventional challenges. It measures the mechanical behavior of soft materials by introducing and expanding cavity deformations within materials' internal structure while generating two stresses simultaneously, radial and hoop stresses. In this study, two porcine livers were tested; the experimental data were used to calibrate the material parameters of three hyperelastic models, namely: Yeoh, Arruda-Boyce, and Ogden. Numerical simulations were performed to validate the material parameters; the outcome of these simulations showed that hyperelastic models were able to predict the material response to cavity loading. The technique assumes spherical configuration of the applied deformations. This assumption was verified via Computed Tomography (CT) imaging technology. From the experimental results, numerical simulations and the CT imaging, it can be concluded that the cavity expansion test is capable of measuring the mechanics of biological tissues without experiencing the difficulties encountered in conventional techniques.

4.1. Introduction

The experimental investigation of biological tissues' mechanics is significantly important in several branches of the medical and biomedical engineering fields, such as diagnostic and therapeutic applications, tissue engineering, and clinical simulations for surgical training. The mechanical response of tissues is an indicator of their biological condition as the mechanical behavior translates the state of their inner (macroscopic and microscopic) structures. Changes in structure could indicate the onset of pathological conditions such as breast cancer (Krouskop et al., 1998; Paszek et al., 2005; Samani & Plewes, 2007), fibrosis (Yeh et al., 2002), and glaucoma

(Last et al., 2011). Also, mechanical properties of tissues have been presented as an excellent solution to challenges associated with image-guided therapeutic applications such as localization of tumors during respiratory motion (Al-Mayah et al., 2008; Eom et al., 2009b), deformable image registration of head-and neck (Al-Mayah et al., 2015), brain shift (Wittek et al., 2007), and image-guided liver surgery and therapy (Al-Mayah et al., 2009; Cash et al., 2007). Therefore, acquiring accurate quantitative information about the behavior of tissues plays a significant role in developing solutions to tackle these challenges.

Currently, indentation is a very reliable technique to quantify material properties of biological tissues as it has the potential to be applied *in-vivo*; however, it is commonly implemented during surgical works (Carter et al., 2001), or it requires surgical interventions (Tay et al., 2006). Alternatives to *in-vivo* indentation are the soundwave based techniques such as ultrasound indentation; nonetheless, challenges related to its clinical applications are arising due to wide variety of parameters and techniques proposed by manufacturers (Franchi-Abella et al., 2013), in addition to the complexity of transforming the local strains into local moduli (Varghese et al., 2001).

The majority of the mechanical information are quantified from *ex-vivo* techniques such as tension and compression tests. Generally, these techniques are effective in measuring material properties; however, the investigated tissues using these techniques are extracted from their biological environment and preserved for a considerable amount of time before testing. The common preservation techniques such as freezing and refrigeration were reported to change the mechanical properties of biological tissues (Nguyễn et al., 2012; Dương et al., 2015; Lu & Untaroiu, 2012b; Brands et al., 2000); in addition, complex cutting processes adopted to prepare the samples into specific shapes (dumbbell/dog-bone) increase the postmortem time spent before testing. Some of these techniques require gripping the sample while loading. However, the aqueous nature of biological tissues is commonly the cause of slippage (Ng et al., 2005). To overcome this issue, several techniques based on roughened grip surfaces have been developed to overcome slippage such as pneumatic clamps (Matthews et al., 1996), serrated jaws (Herzog & Gal, 1999), and sand paper (Nafo & Al-Mayah, 2018). Nonetheless, for the roughened surfaces to be effective, pressure has to be applied by the clamps, which may develop stress concentrations at the clamping region, affecting the stress distribution through the gauge length significantly. Gluing the samples to the

gripping surfaces attenuates the stress concentrations problem, however, this is only effective when the samples are thin; thicker samples will experience shear that causes complex strain distribution at the gripping region, where the sample core experiences less deformation compared to the interface between the sample surface and the gripping surface (Riemersa & Schamhardt, 1982; Soden & Kershaw, 1974). The gravity of the slipping problem is represented in its potential to significantly affect the test data such as the force vs displacement data (Soden & Kershaw, 1974). In compression tests, friction can be a daunting challenge, in particular, between the surface of the sample and the testing rig, which affects the stress distribution along the gauge length of the specimens (Bergstrom, 2015).

This study aims to examine a testing technique that has the potential to eliminate the aforementioned difficulties that accompany testing tissues in ex-vivo conditions. In addition, it has the potential to be implemented *in-vivo* with minimal intervention and feasibility in terms of measuring the mechanics of the tested tissues, which will be addressed in a different study. In this study, two porcine livers will be tested ex-vivo by applying deformations in the form of spherical cavitation. The tissues are assumed to be isotropic and characterized as hyperelastic materials. Three Strain Energy Functions (SEFs) will be used to capture the tissues behavior, namely: Yeoh, Arruda-Boyce, and Ogden. The material parameters of the SEFs will then be validated via FE simulations by using Abaqus®. The test generates two types of stresses, namely, radial and hoop (circumference) stresses simultaneously, which will be analyzed analytically and numerically. The validation of this technique is based on reaching a robust agreement between the experimental and numerical stresses (pressure readings), in addition to stresses predicted analytically and numerically. The analysis in this work is based on the assumption of spherical configuration of the applied deformations. This assumption will be verified using Computed Tomography (CT) imaging.

4.2. Materials and Methods

4.2.1. *Specimen Preparations*

Two fresh porcine livers from two 24 weeks old pigs, weighing about 60 kg were used. The livers were collected within 4 hours postmortem from a local slaughterhouse.

They were preserved and transported to the laboratory in an icebox at 4°C-5°C. During the test, the livers were placed on an aluminum tray, as shown in Figure 4.1, on which they maintained their natural shape.

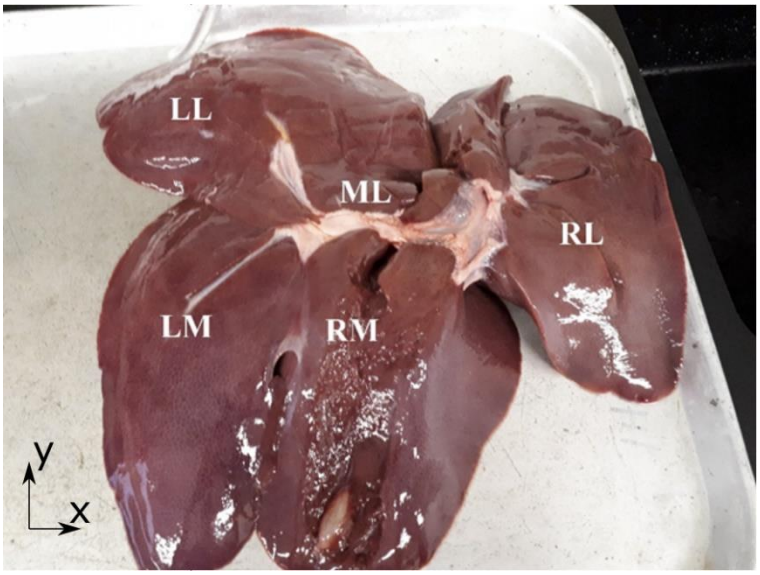

Figure 4. 1. Porcine liver and its main lobes.

4.2.2. *Experimental Setup*

The cavity expansion tests were conducted by using a system of five components (Figure 4.2). It comprises of a needle-balloon tool, pressure sensor (Model PRESS-S-000, PENDOTECH, USA), pressure reader (Model PMAT-S, PENDO TECH, USA), and a syringe pump (Model 75900-00, Cole-Parmer Instrument CO, USA), in addition to a personal computer to record the pressure-time data acquired from the tests. Y-shaped tube was used to connect the syringe, the pressure sensor, and the needle-balloon tool. No air was entrapped in the system; the design of the pressure sensor allows bleeding the air out of the system readily.

The concept of the test is based on injecting a controlled and continuous stream of water into the balloon to generate an expanding cavity within the structure of the specimen. The experiments were performed by inserting the needle–balloon tool into the liver samples. To collect data from various regions of the liver samples, the tool was inserted at six different locations in each of the samples: two locations in the median lobe (ML), and one location in each of the right lateral (RL), right median (RM), left median (LM), and left lateral (LL) lobes. A minimum distance of 3 cm in the x and y directions was kept between needle insertions. The tests were conducted at room temperature ~ 21 °C. All tests were conducted at a fluid injection rate of 5µl s^{-1}.

Also, the balloon response was investigated by using the loading system; the pressure was observed by inflating the balloon with water while the balloon is free from constraints (no boundary conditions were applied). The balloon showed no tangible resistance within the range of injected volumes in which the liver tissues ruptured. A further verification to this observation was conducted by using a more sensitive load cell (MDB-75, Transducer Techniques, USA) and Intron loading frame. A schematic diagram of the investigation apparatus is shown in Figure 4.3 where the collective response of syringe, needle and balloon assembly was investigated.

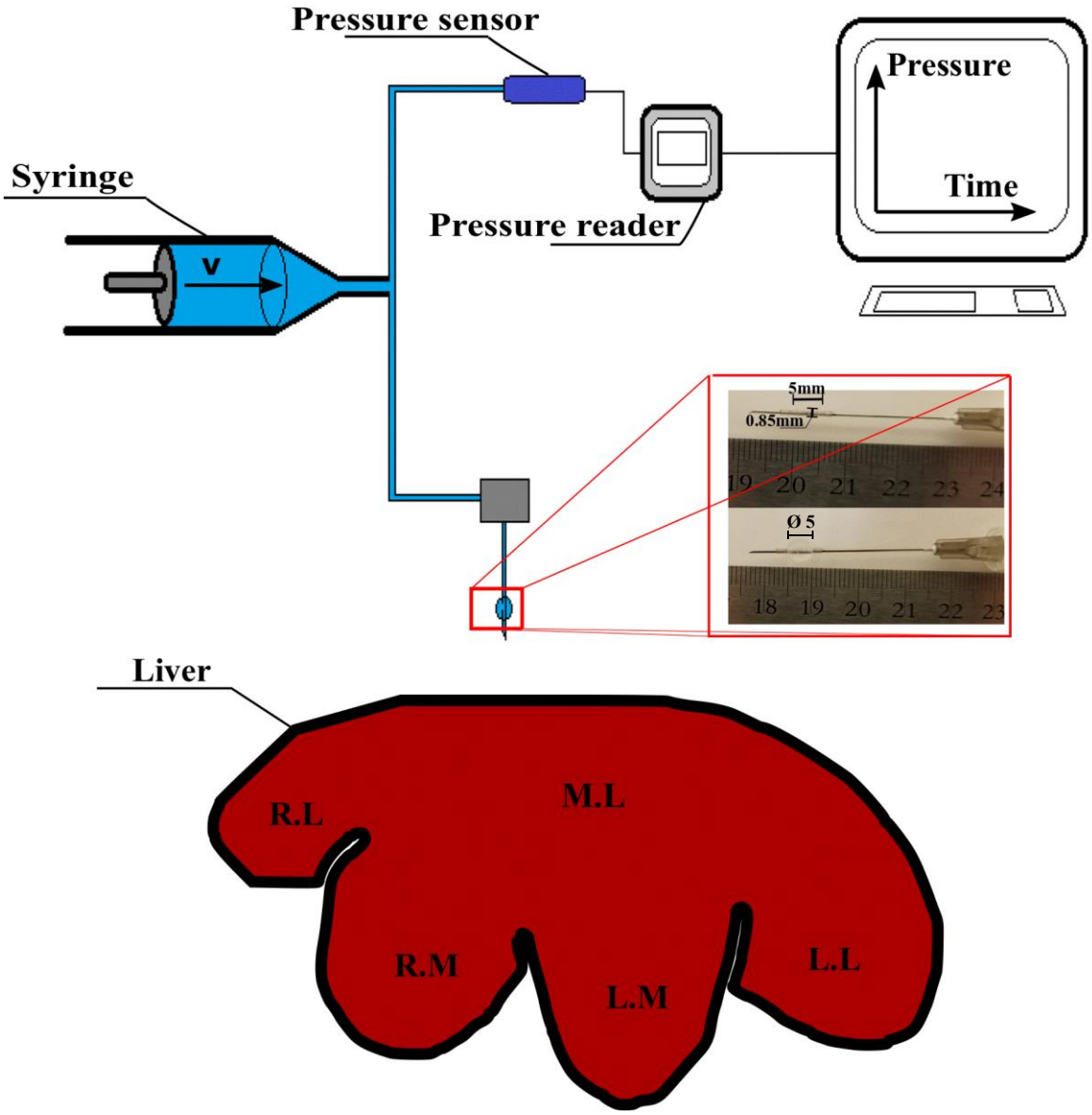

Figure 4. 2. Experimental set up; the system is comprised of a syringe to inject incompressible fluid (water) to the pressure sensor to measure the pressure in the pressurized fluid, and to the needle balloon tool to inflate the balloon. The dimensions of the balloon region before inflation are 5.0 mm in length and 0.85mm in diameter.

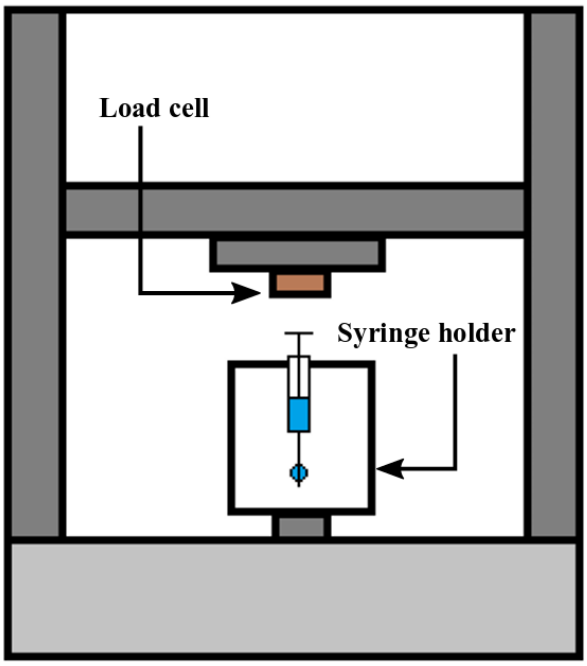

Figure 4. 3. Schematic diagram of the apparatus used to measure the balloon inflation pressure.

4.3.1. Samples Imaging

To observe the configuration of the applied deformations, a micro-focus CT-imaging was performed with x-ray inspection system, Phoenix v|tome|x s (General Electric, Germany) equipped with a 240 kV micro-focus x-ray tube and a 2048×2048 pixels flat panel detector.

Two samples were scanned; the investigation used two different injection volumes, 50 µl, and 100 µl. An iodine-based contrast agent was used in this study, produced by dissolving Sodium Iodide (Nal) into distilled water at room temperature. Each sample was injected with an individual volume and then scanned. The scan parameters applied to all specimens are shown in table 4.1.

Table 4. 1. CT scan parameters.

Acceleration voltage (kV)	Beam Current (µA)	Exposure Time (ms)	Number of projections	Voxel Size (µm)	Scan time (min)	Cu pre-filter (mm)
130	130	333	1000	142	22	0.1

4.3. Constitutive Models

Three hyperelastic models are used in this investigation, namely Yeoh (Yeoh, 1993), Arruda-Boyce (Arruda & Boyce, 1993), and Ogden (Ogden, 1972).

• Yeoh model is a phenomenological model based on the first strain invariant I_1. The incompressible version of Yeoh model is written as

$$W = \sum_{i=}^{N=3} C_{i0}(I_1 - 3)^i \quad (4.1)$$

Where C_{i0} are the material constants.

• Ogden model is also a phenomenological model. It has been used to capture the mechanical behavior of rubber-like materials, including rubbers and biological tissues (Rashid et al., 2014b; Shahzad et al., 2015).

$$W = \sum_{i=1}^{N=3} \frac{2\mu_i}{\alpha_i^2}\left(\lambda_1^{\alpha_i} + \lambda_2^{\alpha_i} + \lambda_3^{\alpha_i} - 3\right) \quad (4.2)$$

Where μ_i and α_i are material constants.

• Arruda-Boyce model is a mechanistic model. It captures the behavior of rubber-like materials precisely by using two material constants, initial shear modulus and extensibility limiter. The model is based on I_1 and defined as

$$W = \mu \sum_{i=1}^{5} \frac{C_i}{\lambda_m^{2i-2}}(I_1^i - 3^i) \quad (4.3)$$

Where C_i are model constants; λ_m is the extensibility limiter; and μ is the shear modulus.

These hyperelastic models can be calibrated using

$$\frac{d\sigma_r}{d\lambda} = \frac{\hat{W}}{(\lambda^3 - 1)} \quad (4.4)$$

Equation 4.4 is derived by combining equations 3.13, 3.15, 3.16, and 3.17.

4.4. Results and Discussion

The tests were conducted by introducing cavitation within the structure of the liver. Cavities were induced by injecting controlled volumes of water, and the pressure readings due to expanding cavities were collected simultaneously. Overall, twelve cavity expansion tests were performed on various regions of the two livers to investigate the tissues' behavior at the applied volumes. The data obtained from each lobe of both livers are shown in Figure 4.4. These data represent the range of pressure readings to the maximum pressure before a drop was observed signaling tissues rupture. The average pressure-volume curve is shown in Figure 4.5. The average data curve was evaluated until a volume (V) of 65µl, at which the majority of the tested samples failed or showed signs of failure. The reported pressure readings are the ones observed during the experiment.

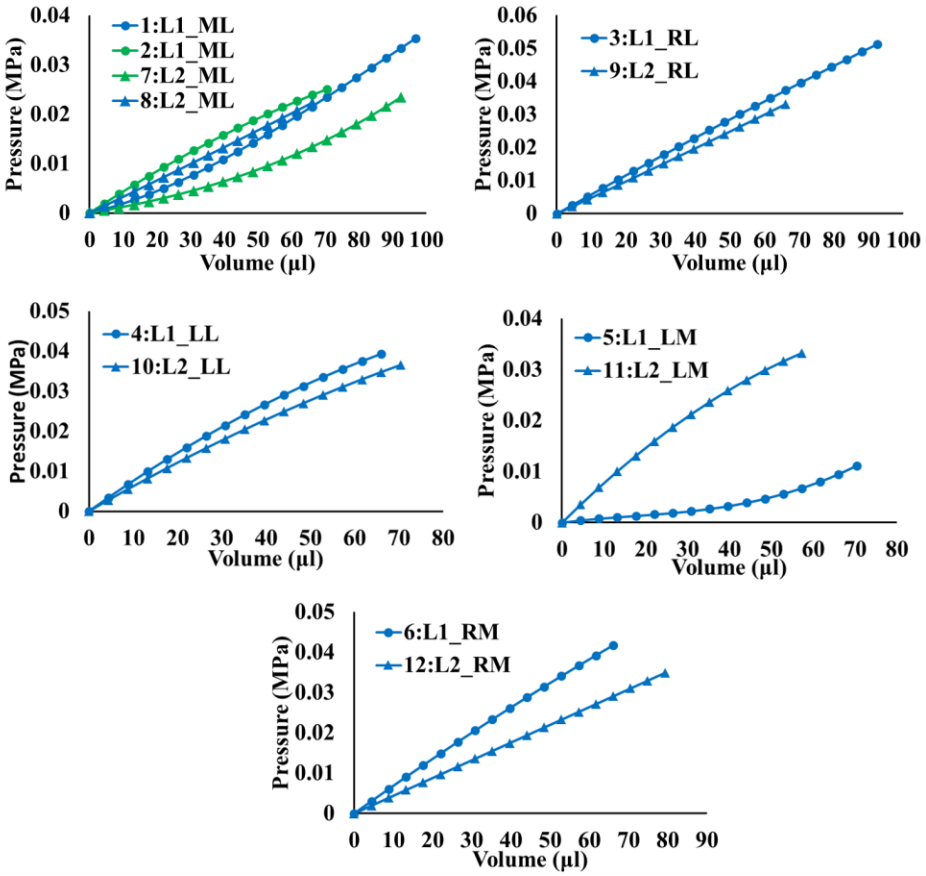

Figure 4. 4. Pressure – Volume data for each lobe in both of the liver samples. The numbers in front of each test represents its order.

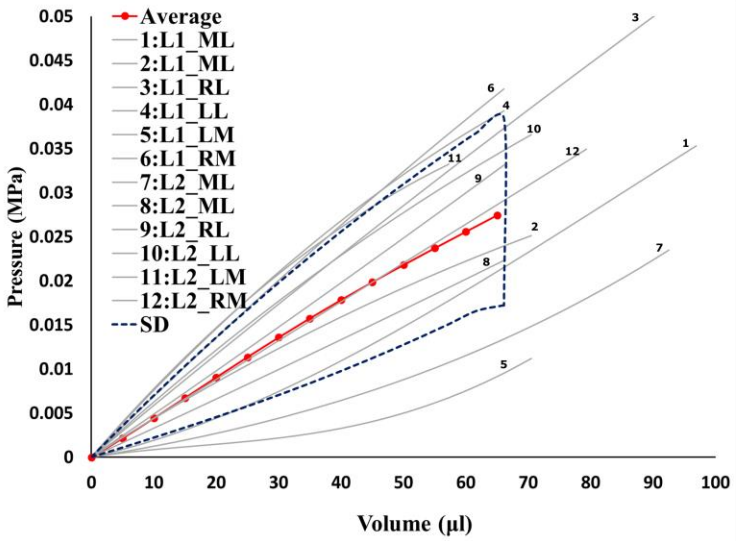

Figure 4. 5. Average mechanical response and the variation corridor (standard deviation) of the liver tissues subjected to cavity deformation. Pressure-Volume data were labeled based on the liver sample (L1 or L2), and based on the region or lobe, for example, L1_ML represents the median lobe of liver sample No.1. Two experiments were performed in the median lobes of both samples, and one experiment was performed in each of the other lobes.

The data showed an expanding standard deviation corridor (±1.08e-03 MPa at V= 5µl, up to ±1.05e-02 MPa at V= 65 µl) as shown in Fig. 5. The pressure-volume data showed a spectrum of behaviors that range from linear response, similar to that observed in other soft materials (Zimberlin et al., 2007, 2010), to non-linear response.

For full evaluation of the system including syringe and balloon, the effects of the syringe-needle-balloon components were investigated separately before needle insertion in tissue using force-displacement frame shown in Figure 4.3. The selection of the force-displacement method for syringe behavior was to provide a common ground for comparison with previously reported works that were based on force-displacement theme (Brostow et al., 2007; De Bardi et al., 2018; Kasem et al., 2019; Zhang et al., 2018). Initially, an instant increase in force data occurred due to the friction (static) of the rubber stopper on the barrel's inner wall followed by a constant friction response as the stopper broke loose, and the injection entered the dynamic phase. During this process, the balloon showed no response, nevertheless, it started to show tangible stiffening after the stopper moved for 2.25 mm representing a balloon inflation volume of 116 µl (180% of the volume at which the tissues showed signs of failure). The balloon force-displacement data was converted into pressure-volume form by using the barrel's inner radius (4.05mm), see Figure 4.6. The region highlighted in green shows the amount of volume corresponding to the averaged experimental pressure. The segment marked in red represents a stiffening of the balloon as it starts to resist inflation. It is worth mentioning that the syringe effect (static and dynamic frictions) does not affect the sensor's pressure readings in the original technology as shown in Figure 4.7, where a pilot study was conducted on L2_RM liver sample. The pressure sensor and the load cell collected data sets simultaneously. Both sets showed similar rate of change and pressure range as a result of tissue resistance to cavity expansion.

For convenience, the deformation term in Figure 4.5 was converted into the stretch term λ. The definition of λ is presented as r/R in which R was set to be 1.42 mm (See Appendix B), while r was evaluated as

$$r = \sqrt[3]{\frac{3(V_i+V_{app})}{4\pi}} \tag{4.5}$$

Where V_i is the initial volume which includes the volume of the balloon region before inflation, and the water volume introduced into the balloon before the tissues start to resist balloon inflation.

V_{app} is the injected volume of water introduced into the balloon when tissues start to resist balloon inflation.

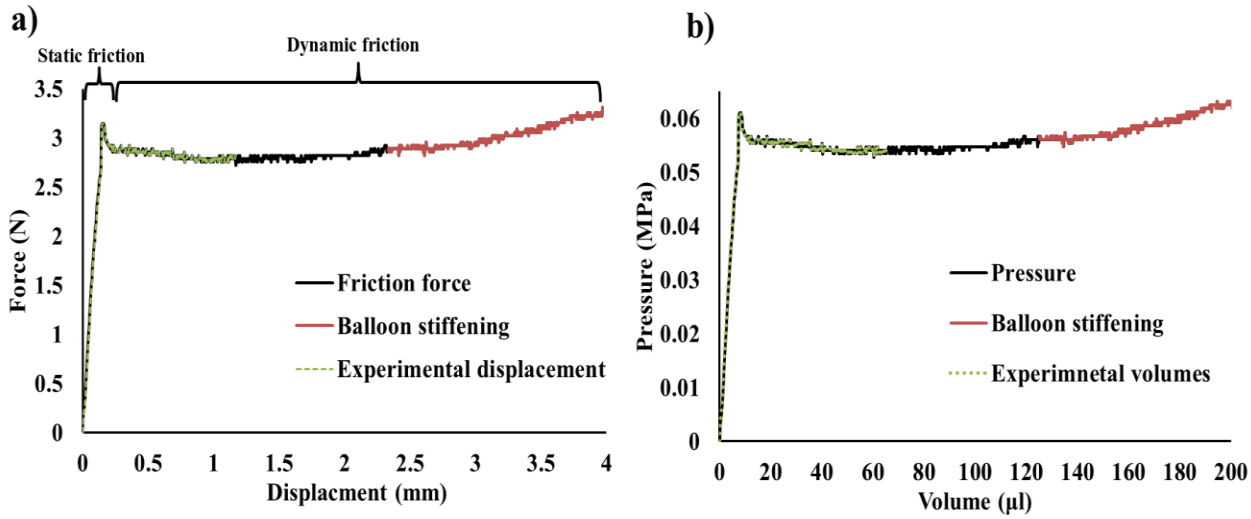

Figure 4. 6. Balloon response. The overall response is similar to a typical force mechanism of syringes 146; it starts with a static (breakaway) friction force followed by dynamic (gliding) friction force. a) The force-displacement data; b) the pressure-volume data.

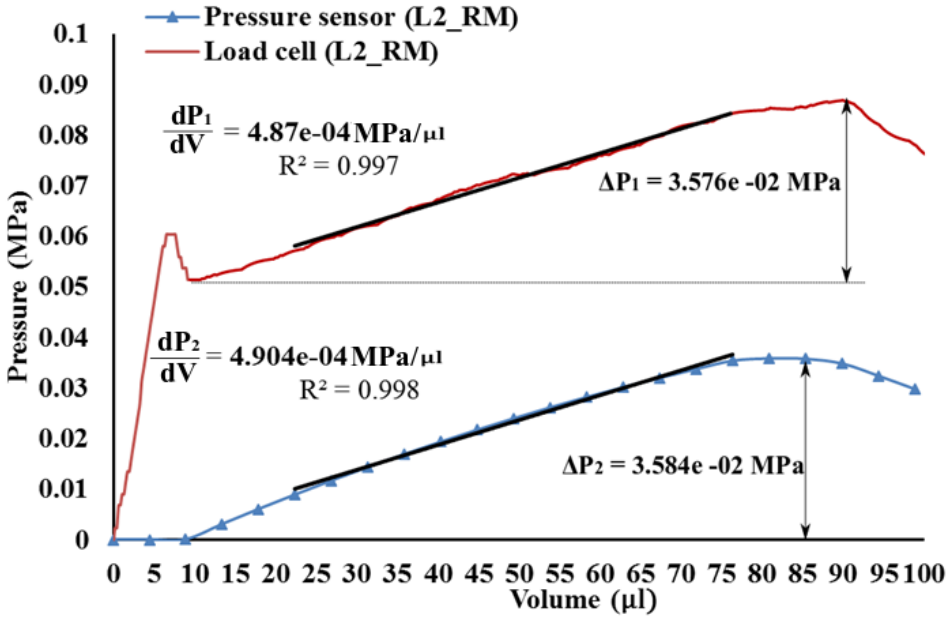

Figure 4. 7. Data sets obtained by the pressure sensor and the load cell.

The instantaneous rate of change of the P-λ data was calculated at numerous data points to allow the calibration process through equation 4.4. The material constants of the models were calibrated by the least squares method.

A good agreement between the experimental data and the calibrated models can be observed in Figure 4.8. The material constants of the three models are summarized in tables 4.2. The quality of fit is represented by R^2 shown in Figure 4.8, which represented as $R^2 = \frac{T_t - T_r}{T_t}$, where T_t is the total summation of the squared residuals of the mean and data points; T_r is the summation of squared residuals around the regression line.

Table 4. 2. Materials constants of the Yeoh, Ogden and Arruda-Boyce models.

Material coefficient	
Yeoh Model	
C_{10} (MPa)	2.1e-03
C_{20} (MPa)	4.18e-03
C_{30} (MPa)	-5.83e-05
Ogden Model (N=3)	
μ_1	1.61e-02
α_1	-2.128
μ_2	1.225e-01
α_2	-1.521
μ_3	-1.345e-01
α_3	-1.36
Arruda-Boyce model	
μ	4.06e-03
λ_m	1.081

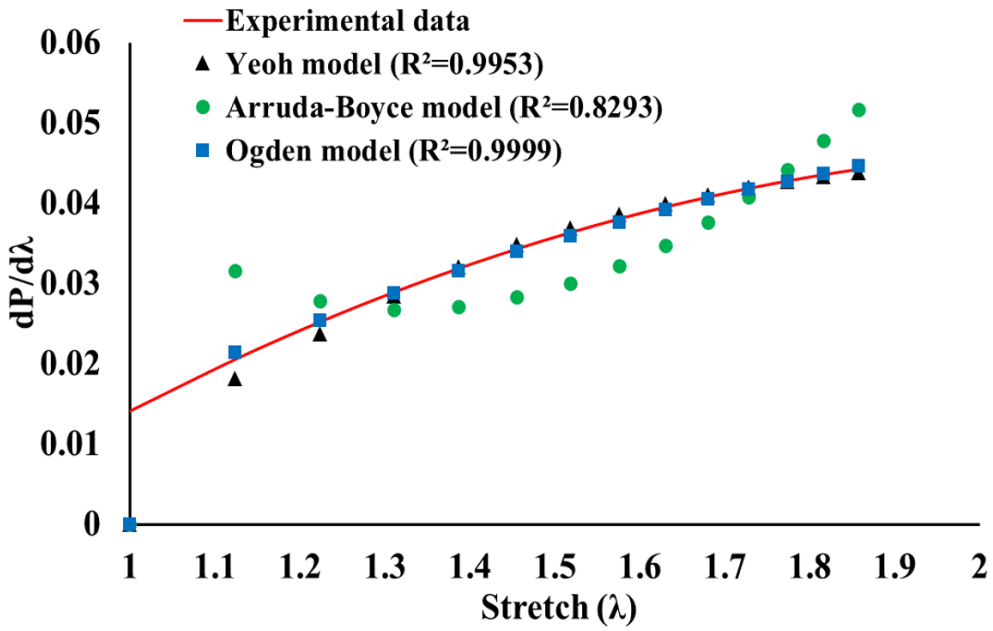

Figure 4. 8. Calibration of the hyperelastic models.

All three models provided an excellent fit to the averaged experimental data. The material parameters from the calibration process will be used in FE simulations.

Once the micro-CT data (2D projections) were collected, Volume Graphics (VG) (*Volumegraphics.com*), an image analysis software was used to visualize the data by volume rendering, as shown in Figure 4.9. VG offers two tools that were adopted in this work to verify the configuration of the injected volumes, "Inclusion Analysis" and "Distance Tool". The verification process is based on comparing the calculated volumes with the injected ones, in addition to comparing the measured radii with the nominal ones.

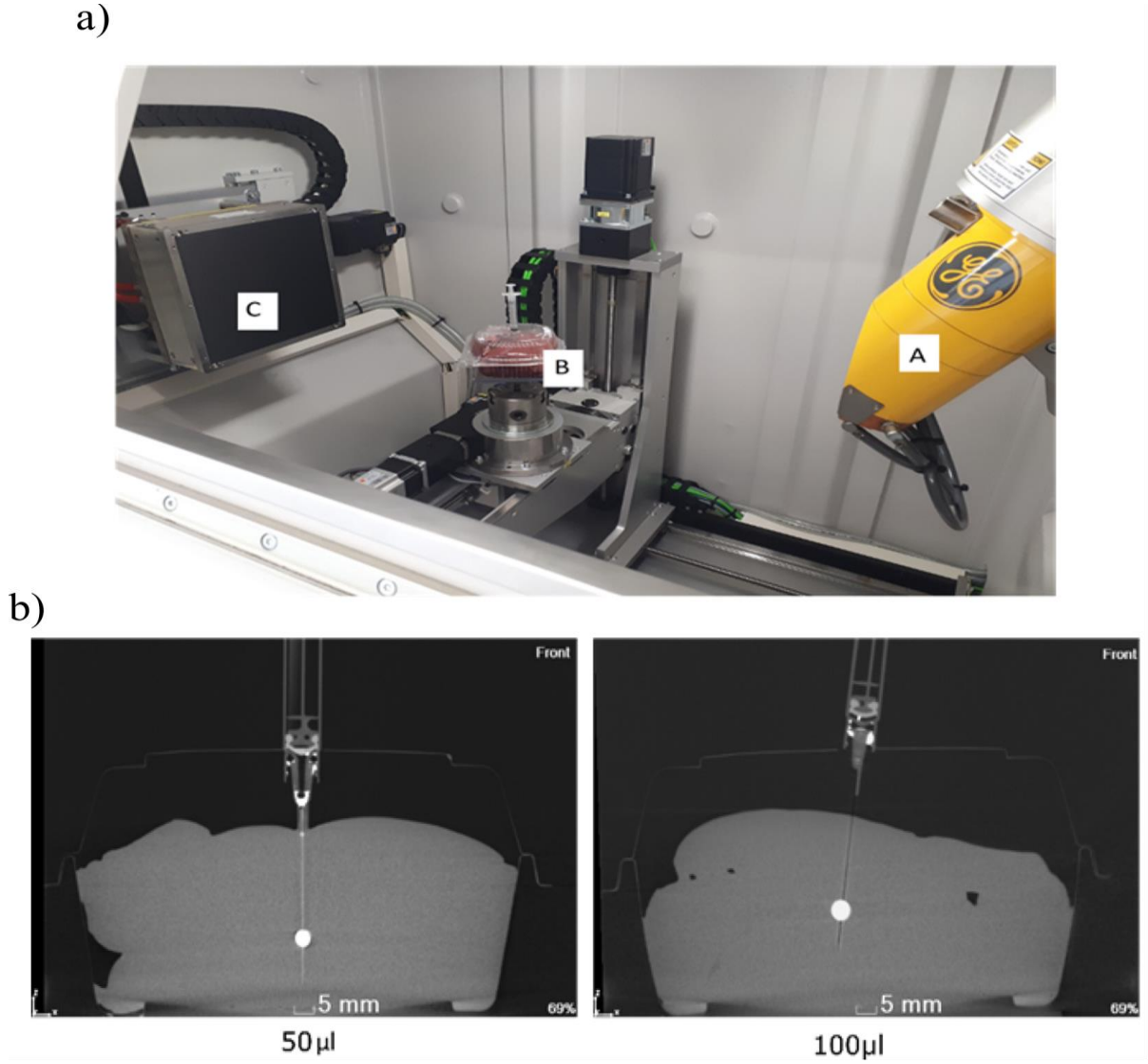

Figure 4. 9. a) A photograph of the micro-CT scanner used during the study, including the x-ray tube (A), the sample (B), and the detector (C). b) The configurations of spherical cavities within the liver tissues' internal structural. The higher volume (100 µl) imposes higher pressure on the liver tissues.

The outcome of the analysis indicated that the calculated volumes match the injected volumes inside the balloon, as illustrated in Figure 4.10 (a, b). The analytical radii (from VG) were calculated by taking the average of the balloon radii in x-axis and z-axis. Overall, the actual radii matched the nominal ones, as shown in Figure 4.10 (c). The verification process conducted by VG offers a strong validation to the assumption of spherical configuration of the applied cavities.

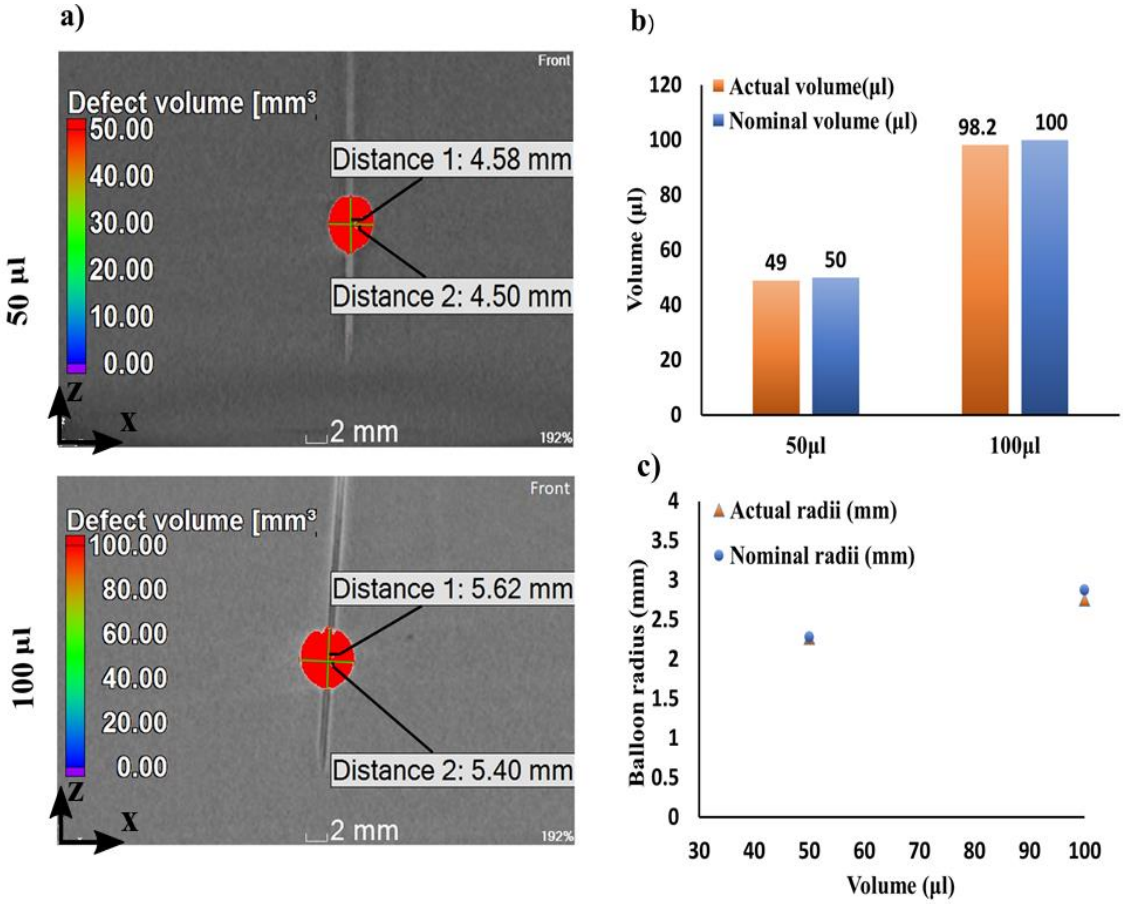

Figure 4. 10. a) Image-based diameters and volume measurements in two different volume injection values. The term "Distance 1" represents the diameter in the z-direction, and the term "Distance 2" represents the diameter in the x-direction. b) Match between the injected volumes and the volumes calculated by VG. c) Comparison between actual and nominal radii.

The calibrated hyperelastic models are implemented in numerical simulations. These simulations are carried out using Abaqus® (ABAQUS/CAE, 2013). During the experiments, the cavity expands in a medium that has no external restraining boundary conditions. The tissue volume around the tool is significantly large relative to the balloon size thereby a thick sphere scenario was adopted to simulate the cavity expansion inside the liver tissues where a large outer radius b_o was selected to be a hundred times the inner radius a_o (b_o=100 a_o), see Figure 4.11 (a and b); this reflects the fact that stresses induced by the cavity are distributed within close proximity to its wall. The

numerical model was created by 4-node axisymmetric quadrilateral elements with hybrid formulation (CAX4H). The mesh configuration is based on distributing the elements radially with gradual change of dimensions; the elements' size is 1 μm × 50 μm at the cavity wall and 100 μm × 50 μm at the circumference.

These dimensions were determined based on a convergence study, in which, the radial and hoop stresses converged satisfactorily. The loading process was based on applying the pressure observed during the experiments at the cavity wall, see Figure 4.11 (a). Due to the local nature of the cavity test, the stresses from the numerical model at the cavity wall were compared against the experimental data and the analytical solution (equation 3.15).

A good agreement between the average experimental pressure and the numerically predicted radial stress was achieved; see Figure 4.11 (c). Moreover, the material parameters of the three energy functions, which were used to predict the hoop stress analytically, were further validated against a corresponding stress predicted numerically; a good agreement between analytical hoop (equation 3.15) stresses and numerical hoop stresses was achieved, see Figure 4.11 (d).

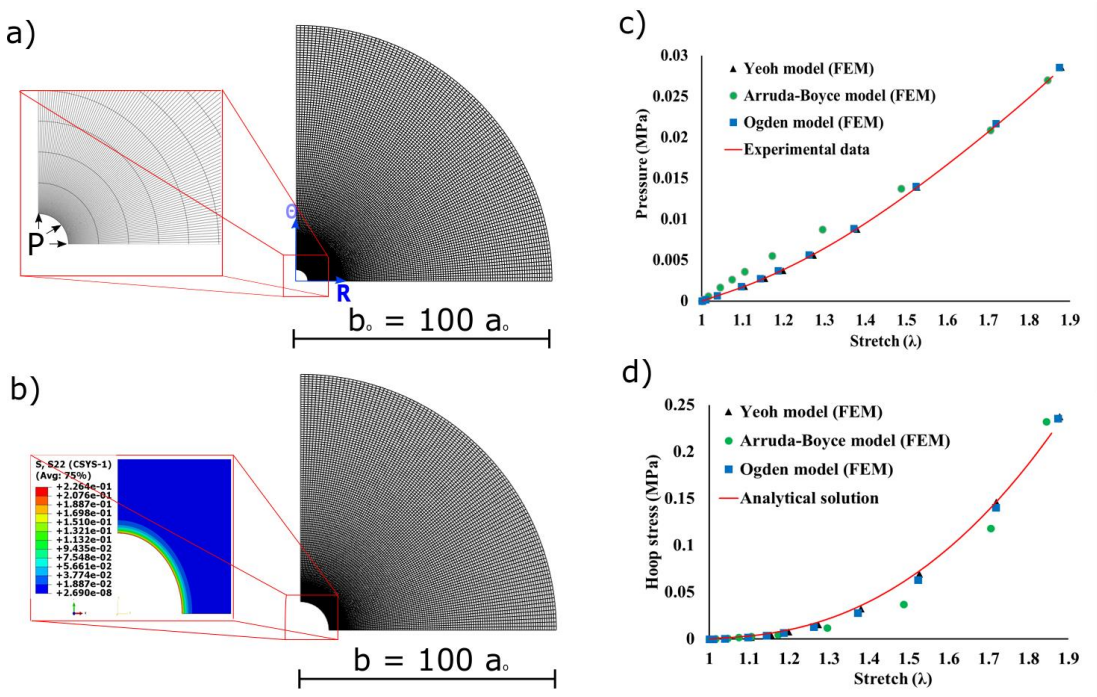

Figure 4. 11. a) An axisymmetric finite element model to analyze spherical cavity expansion in hyperelastic medium; b) Radial deformation applied at the cavity wall; c) Experimental and numerical pressure results; d) Analytical and numerical hoop stress results.

During the expansion of the balloon within the tissues' structure, radial and hoop stresses were generated simultaneously. These stresses were analyzed statistically by one-way ANOVA test. While Arruda-Boyce strain energy function (SEF) was the least accurate, yet sufficient, in predicting the experimental pressure, Yeoh and Ogden showed no significant difference between the experimental pressure and the numerically predicted pressures: p=0.8235, p=0.9877, p=0.9428, respectively, as shown in Figure 4.12 (a). Similarly, the three models successfully predicted the hoop stresses; there was no significant difference between the hoop stresses predicted analytically by equation 3.15 and the numerical hoop stresses: p= 0.9705, p= 0.8124, and p=0.9513 when Yeoh, Arruda-Boyce, and Ogden strain energy functions were used, respectively, as shown in Figure 4.12 (b). In addition, the three SEFs measured similar initial shear moduli of the liver tissues: μ_Y= 4.2 kPa, $\mu_{AB=}$ 4.06 kPa, and μ_{OG} = 4.17 kPa, for Yeoh, Arruda-Boyce, and Ogden models, respectively. The shear moduli measured by the three SEFs fall within the range of moduli of porcine liver (3 kPa – 5 kPa) reported in (Samur et al., 2007). The deformation level at which the liver tissues showed signs of failure λ_{ult} was 1.85, this magnitude also agrees with deformation levels reported in literature due to stretching (1.3 – 1.86) (Dương et al., 2015; Gao et al., 2010b). The reported magnitude of the ultimate hoop stress (≈0.25 MPa) is also acceptable. Although no data are reported for liver tissues tested under bi-axial tensile or tri-axial loading, fresh porcine liver tissues were reported to experience an ultimate tensile stress (Cauchy stress) magnitude of 0.182 MPa in uniaxial stretching (Dương et al., 2015), which makes the results in this work reasonable as the ultimate stresses in biaxial-loading are normally higher than in one-directional loading. The good agreement between the experimental, analytical, and numerical results indicates that the implemented SEFs (Yeoh, Arruda-Boyce, and Ogden) are capable of capturing the mechanical behavior of the liver tissues. Furthermore, the technique is efficient to characterize the hyperelastic behavior of soft biological tissues.

The findings from this study strongly indicate to the capability of the cavity technique to measure the mechanical behavior of the biological tissues. The pressure generated in this test was measured experimentally, and the stresses were efficiently predicted by numerical and analytical means.

The CT images showed that the balloon expands spherically when inflated within the liver tissues by a relatively incompressible fluid (water). This was proved by analyzing a subset of the injected volumes (50 μl and 100 μl). The VG analysis results showed that calculated volumes are similar

to those injected (nominal volumes). In addition, radii measured by VG were similar to the nominal radii of the injected volumes. The spherical configuration of the deformations validates the use of equation 13 to calibrate the material parameters for each of the SEFs.

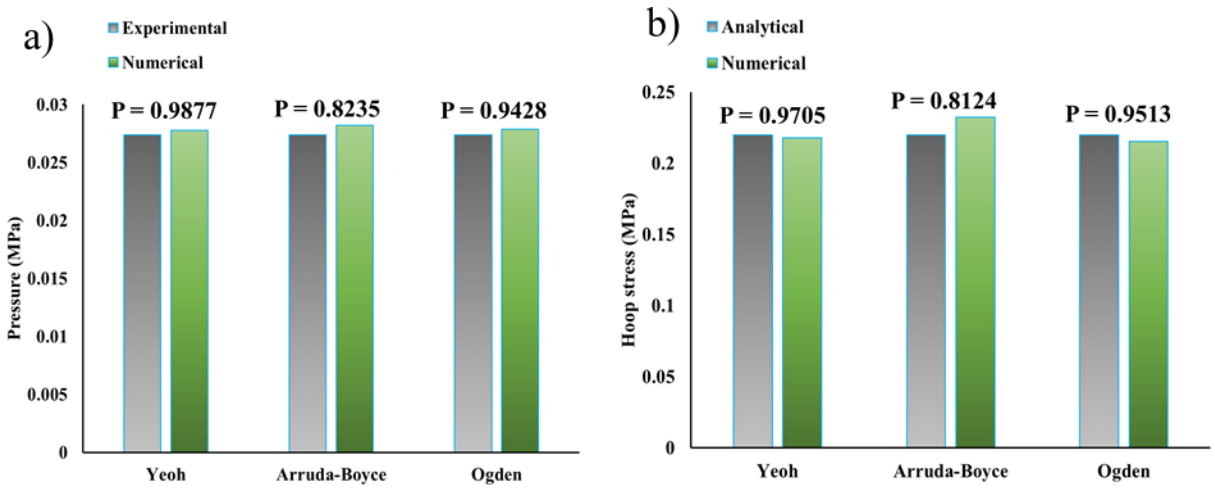

Figure 4. 12. Excellent agreement between the experimental, analytical, and numerical results based on one-way ANOVA tests.

The effect of the needle insertion into the liver tissues was neglected in this study as the stresses and strains generated during the insertion process are significantly smaller than the stresses and strains generated during the cavity expansion test (Nafo & Al-Mayah, 2019).

The statistical analysis showed that the parameters obtained from calibrating the SEFs provided a response that is similar to the one observed during the experiments. The FEM results presented in this work addressed the stresses at the cavity wall; beyond it, they immediately decline in a sharp manner. This is obvious when the stresses were numerically calculated at various locations beyond the cavity wall when a pressure corresponding to a volume of 65 µl was applied, which indicates to the local nature of the cavity expansion technique, see Figure 4.13.

A limitation in this study is the material parameters of the SEFs were estimated based on an average experimental data. The variations of the experimental data might be due to the random distribution of arteries, veins, and ducts within the tissues, which was not considered in this study. Nonetheless, the material parameters are still useful to model an approximate behavior to that of liver tissues subjected to cavitation rheology. Average experimental data were used to define the mechanical properties of several biological tissues (Dương et al., 2015; Kemper et al., 2010; Miller & Chinzei, 1997; Rashid et al., 2014b) thus it was adopted in this study.

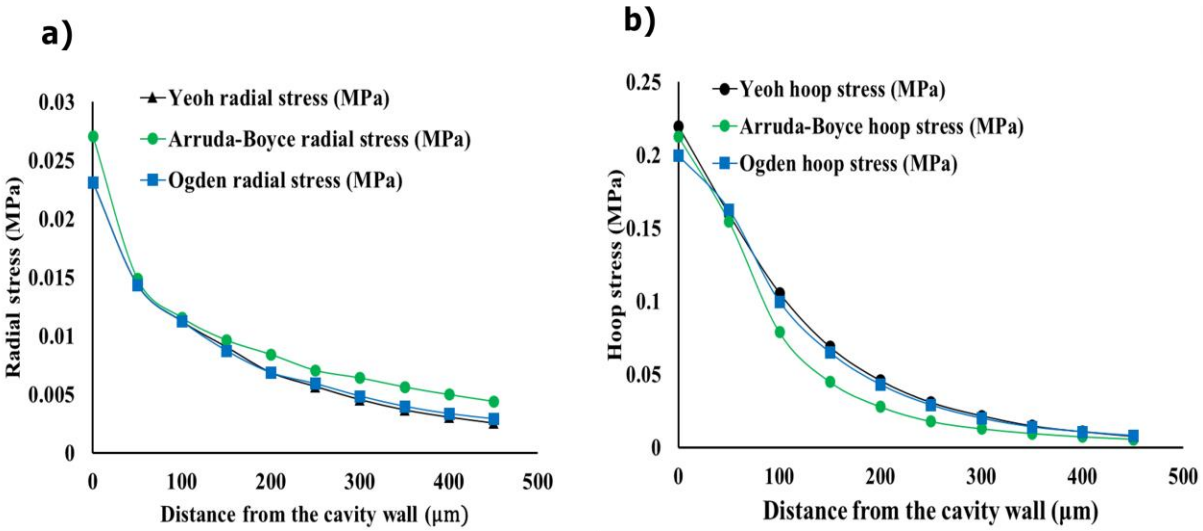

Figure 4. 13. The local nature of the cavity expansion test: Significant drop in the stresses magnitudes beyond the cavity wall: a) radial stresses, b) hoop stresses. The three-hyperelastic models predicted that the radial and the hoop stresses sharply diminished at 450 μm beyond the cavity wall.

The cavity expansion technique proved to be efficient in predicting the initial shear modulus of the liver tissues. It also reported a stretch magnitude that agrees with the stretch levels reported in literature. In addition, the cavity expansion technique successfully predicted the ultimate tensile stresses at which the tissues ruptured.

4.5. Conclusions

This study presented twelve cavity expansion tests performed on two porcine livers. The following results can be concluded from this study:

(i) Yeoh, Arruda-Boyce, and Ogden models provided excellent fitting to the experimental data ($0.8235 \leq R^2 \leq 0.9877$).

(ii) The CT investigation results indicated that using a spherical balloon to apply cavity deformations results in deforming the tissues around the balloon spherically.

(iii) Excellent agreement between the experimental and numerical results at the cavity wall, in addition to the agreement between hoop stresses predicted analytically and numerically indicate that the three SEFs are capable to characterize the behavior of liver tissues subjected to cavitation rheology.

Based on these results, the cavity expansion test is capable of measuring the mechanical behavior of liver tissues without experiencing the difficulties that normally accompany conventional techniques.

Chapter 5

Characterization of PVA Hydrogels' Hyperelastic Properties by Uniaxial Tension and Cavity Expansion Tests

Abstract

The mechanical behavior of rubber-like materials is dominantly non-linear elastic. Their mechanical response is measured by numerous conventional techniques including the universal loading machines (tension and compression) and indentation. Recently, an unconventional technique based on cavitation rheology has been implemented to measure the mechanics of these materials. The loading mechanism of this technique is different from the axial force-displacement mechanism observed in the other techniques thus the aim of this study is to investigate the difference between the cavity expansion technique and one of the conventional techniques, uniaxial stretching, to understand the difference in material responses under each loading mechanism. PVA hydrogel was used as a representative of hyperelastic materials. The gels were loaded by both techniques, and hyperelastic models (Yeoh, Ogden, and Arruda-Boyce) were used to model their behavior. FE simulations were performed to reproduce the experimental data. It was observed that the tension stresses generated during the cavity expansion test were similar to those generated in the uniaxial tension to a strain level of 45%, afterward, the cavity tension stresses increased exponentially exceeding those generated in the uniaxial tension. When the von Mises stresses, from both tests, were compared against the major tension stress data, it was observed that the cavity test imposed tension stresses that were twice of those generated during the uniaxial tensile test. In addition, the hoop stresses were significantly larger than the applied pressure. These observations indicate to the equi-biaxial nature of the cavity expansion test.

5.1. Introduction

Numerous techniques have been developed to investigate the mechanics of rubber-like materials such as polymers, gels, and soft biological tissues. These techniques include stretching (uniaxial and biaxial) (Rashid et al., 2014b; Shahzad et al., 2015), compression (confined and unconfined) (Buschmann et al., 1997; Cornelius O. Horgan & Murphy, 2009; Nafo, 2016), and indentation (Ashrafi & Tönük, 2014; Giannakopoulos & Triantafyllou, 2007; Nafo & Al-Mayah, 2018).

Cavity expansion associated mechanics have attracted a significant research effort in the past decades. In late 1950s, Gent and Lindley applied cavity expansion mechanics to investigate the elastic modulus measurement of rubber (Gent & Lindley, 1959). Over the past decade, a number of studies exploited the concept of cavitation rheology to measure the mechanics of soft materials, in which cavities were introduced into different materials by compressing a compressible fluid (air) while it was in direct contact with the material (Kundu & Crosby, 2009; Poulain et al., 2017; Zimberlin et al., 2007; Zimberlin & Crosby, 2010), and an incompressible fluid (water) (Zimberlin & Crosby, 2010) into the tested medium. The induced cavity was created using arbitrarily nucleated open-cavity that was monitored using imaging to measure the volume. An enclosure to the injected fluids was used to apply pre-determined volumes and a geometric configuration to isolate the fluids from the tested medium (Nafo & Al-Mayah, 2019).

The cavity expansion technique combines two unique features of the conventional tensile and indentation tests. While the tension test examines the material mechanics by stretching, indentation provides a local perspective about the material response to deformations; the cavity expansion technique stretches the material structure within a controlled region which allows measuring its mechanics locally (Nafo & Al-Mayah, 2019). The stresses generated by the spherical cavity expansion technique are radial and hoop stresses. The radial stresses are generated in the form of pressure orthogonal to the cavity wall, and the circumferential hoop stresses are generated tangential to the cavity wall in the form of tensile stresses due to resisting expansion. Hoop stresses are larger than the radial stresses in soft materials (Nafo & Al-Mayah, 2019). Most of the previous work on mechanical characterization of materials using cavitation rheology considered the mechanical response of the rubber-like materials as linear elastic, and only addressed the radial stresses as an indicator to material behavior. Nafo & Al-Mayah, 2019 considered the rubber-like materials as hyperelastic and implemented three strain energy functions (SEFs) to characterize the mechanics of this type of materials, in addition, they analytically quantified the hoop stresses generated during the cavity expansion process. However, the relationship between stresses generated due to expanding cavities and conventional tensile tests is not fully established. Therefore, in this study, the performance of the cavity expansion test is compared with that of the conventional uniaxial tensile test to investigate the stretching mechanics induced during the cavity expansion test.

The analysis of rubber-like materials is based on calibrating hyperelastic models to reproduce the experimental data. The SEFs are calibrated based on the experimental data from both tests (cavity expansion and tension). An FE solver, Abaqus®, is used to simulate the non-linear behavior of rubber-like materials. Among various SEF models are Yeoh, Ogden, and Arruda-Boyce models that proved to be efficient in fitting the experimental data in uniaxial and biaxial stretching (Sasso et al., 2008a; Shahzad et al., 2015), therefore, they are used in this study.

PVA hydrogel is used in this study. This type of hydrogels is known for its isotropic nature and low compressibility. Urayama et al 1993 (Urayama et al., 1993) reported Poisson's ratio magnitudes in the range of 0.45-0.48 for PVA hydrogel. In addition, Nafo & Al-Mayah, 2019 reported that there is no significant difference in the material's mechanical behavior between incompressible and compressible assumptions. Therefore, an incompressible assumption is considered in this work.

In this study, cylindrical and sheet specimens of PVA hydrogels were prepared and tested by the cavity expansion and uniaxial tensile tests, respectively. Moreover, the experimental data were used to calibrate the material constants of Yeoh, Ogden, and Arruda-Boyce models. Lastly, FE simulations were performed to reproduce the experimental data and to investigate the material response under the two types of loading.

5.2. Materials and Methods

5.2.1. *Preparations of PVA hydrogels*

A 10% w/w PVA solution was made by mixing 99+ % hydrolyzed PVA (molecular weight of 160000 – 186000 $g.mol^{-1}$) with deionized water. The mixing process was performed at 90 ^{o}C by the use of standard flask/column combination. The solution was poured into cylindrical molds (40 mm in height and 36 mm in diameter), and prism molds (150 mm x 150 mm x 2 mm) to create cylindrical and sheet specimens of PVA hydrogels. The solution was frozen at -20 ^{o}C for 6 h, and then thawed at room temperature ~21 ^{o}C for 6 h. This freeze-thaw cycle (FTC) was repeated two times. Subsequently, the samples were taken out of the molds and rinsed with deionized water. The cylindrical samples (five samples) were directly tested by the cavity technique. The gel sheet was cut into specific shapes (to make five samples) and then tested by a uniaxial tensile machine. Figure 5.1 shows the preparation of the PVA hydrogel samples.

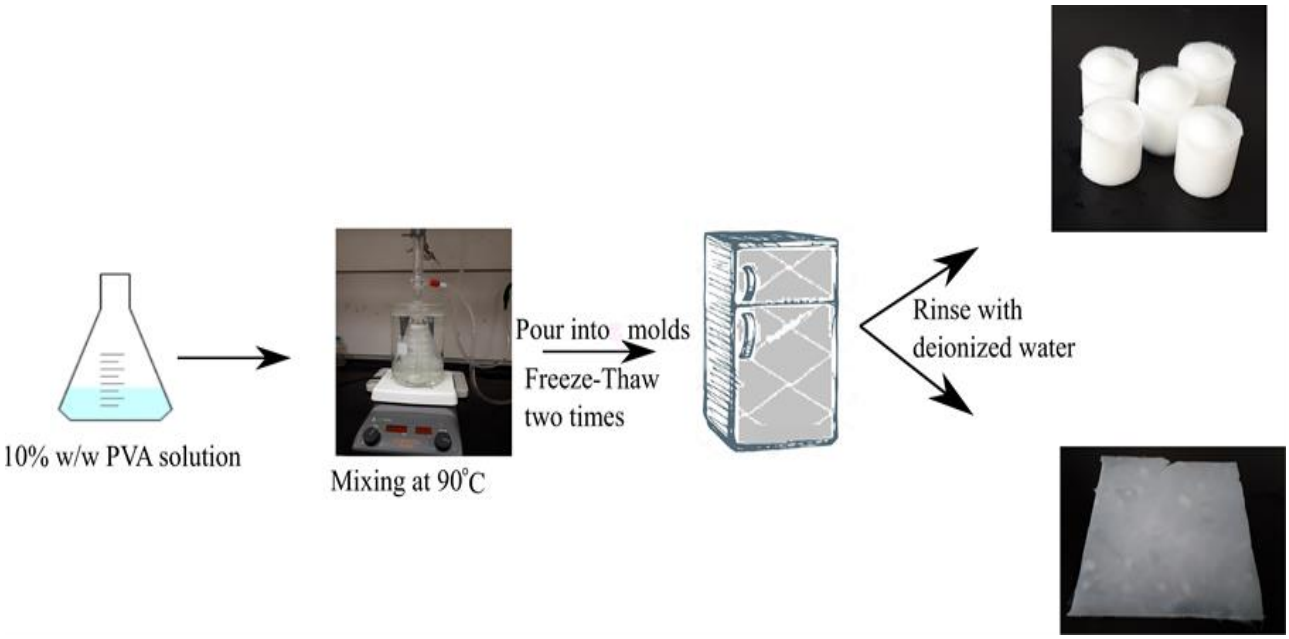

Figure 5. 1. Schematic diagram for the preparation process of PVA hydrogel.

5.2.2. *Uniaxial Tensile Test*

A standard uniaxial tensile test was performed on PVA hydrogel sheet specimens. The gauge zone of the specimens was 30 mm in length, 15 mm in width, and 2 mm in thickness. The gauge length was defined by two black markers spaced at 15 mm apart. A Nikon D90 high resolution CCD camera was used to record sample deformation during the loading process. The deformation (displacement) was measured by tracking the markers using Tracker software (*Tracker Video Analysis and Modeling Tool for Physics Education*). The test was performed using Instron loading machine (model 4465; Canton, MA, USA) equipped with 5 kN load cell. The deformation was applied at a strain rate of $0.1s^{-1}$. Sand paper was used at the clamping regions to prevent potential slippage due to the aqueous nature of the PVA hydrogels. Moderate clamping pressure was applied during the fixation of the sample to avoid complex stress distributions at the clamping regions and to ensure the failure occurs within the gauge length; the experiment set up is shown in Figure 5.2.

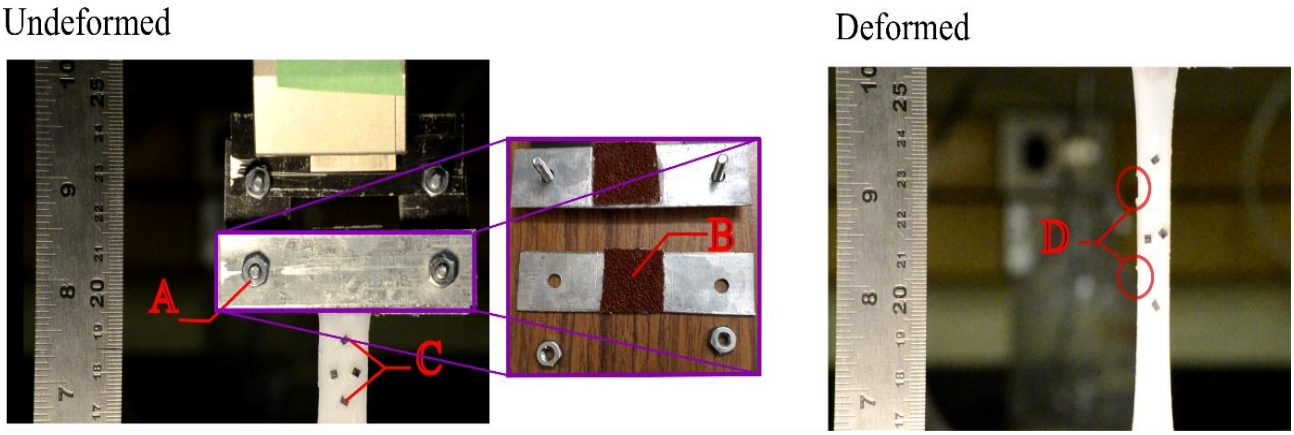

Figure 5. 2. Illustration of the tensile test performed on a PVA hydrogel specimen; A) screws used to apply moderate pressure at the clamping region; B) Sand paper glued to the metal clamp; C) black markers to allow tracking deformations; D) the onset of failure within the gauge length.

5.2.3. *Cavity Expansion Test*

The test was performed using a system that consisted of a custom-made frame to hold a 3 ml syringe during the loading process, silicon tubes connected the syringe with a needle-balloon tool, pressure sensor (Model PRESS-S-000, PENDOTECH, USA); and pressure reader (Model PMAT-S, PENDO TECH, USA). The water was injected by the Instron machine through the tubes into the tool at a rate of 5 μls^{-1} to apply internal cavity deformations to the structure of the hydrogels. The applied pressure on the syringe was measured using the pressure sensor that is directly attached to the needle tube. In addition, the pressing force on the syringe was measured using a load cell. This is mainly motivated by capturing all elements associated with the cavity test system including friction inside the syringe. An effort was made to ensure no air was trapped inside the tool by submerging it into a 250 ml glass breaker filled with water until the tool sank, then it was connected to the tube while submerged under the water. A schematic diagram of the system is shown in Figure 5.3.

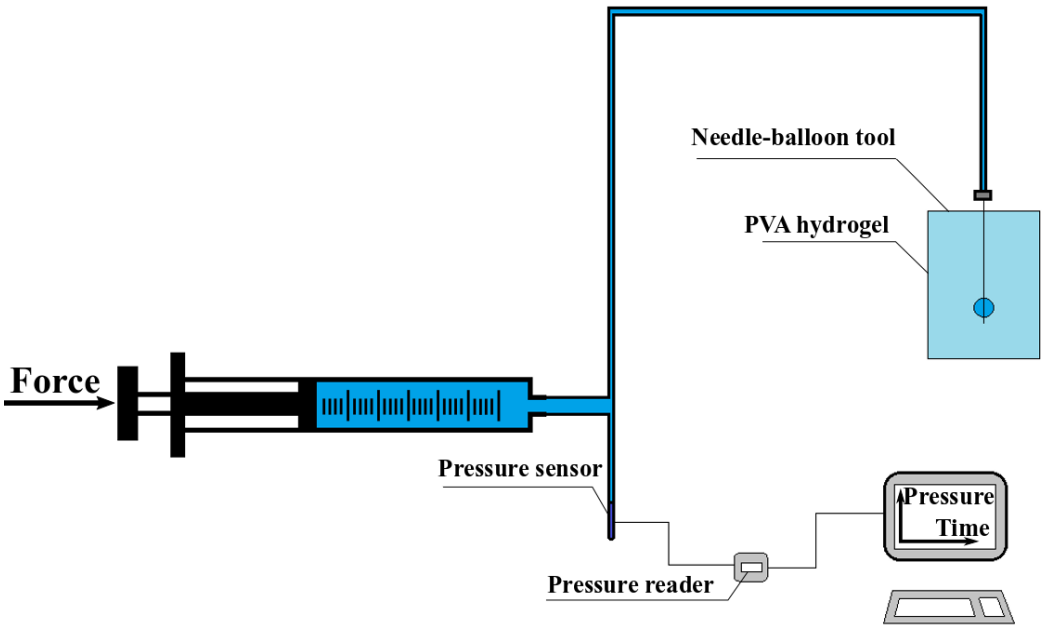

Figure 5. 3. The loading setup: the system utilizes the Instron machine to inject water into the needle-balloon tool, and it utilizes the pressure sensor to measure the pressure in the system.

5.2.4. *Hyperelastic Constitutive Models*

Hydrogel materials are known for their "hyperelastic" behavior; they exhibit very large deformation and non-linear stress-strain relationship. In order to numerically reproduce the mechanical response of the hyperelastic materials, data obtained from the experimental work are used to calibrate the hyperelastic constitutive models. Numerous hyperelastic models are proposed in the literature; this work focuses on two types of models: strain invariant-based (Yeoh and Arruda-Boyce) and stretch-based (Ogden) models.

Yeoh model has been used in characterizing the behavior of several hyperelastic materials such as reinforced natural rubber (Shahzad et al., 2015), hydrogels (Nafo & Al-Mayah, 2019), and biological tissues (Safshekan et al., 2016). The Yeoh model for incompressible rubber-like materials is expressed as

$$W = \sum_{i=1}^{3} C_{i0} \, (I_1 - 3)^i \qquad (5.1)$$

Where I_1 is the first strain invariant, C_{i0} are the material parameters.

Ogden model is a principal stretch based model and commonly used to characterized the hyperelastic properties of rubber-like materials that exhibit large deformations (ε=600%) (Ogden

et al., 2004). In addition, this model is used to define the nonlinear elastic response of biological tissues (Rashid et al., 2014b). The Ogden model is expressed as

$$W = \sum_{i=1}^{N=3} \frac{2\mu_i}{\alpha_i^2} \left(\lambda_1^{\alpha_i} + \lambda_2^{\alpha_i} + \lambda_3^{\alpha_i} - 3\right) \quad (5.2)$$

Where μ_i and α_i are the material parameters. λ is a stretch term.

Arruda-Boyce model is a molecular chain network-based model. It was proposed by Arruda and Boyce (Arruda & Boyce, 1993), and it is commonly used to characterize rubber like materials (Nafo & Al-Mayah, 2019; Sasso et al., 2008; Shahzad et al., 2015). This model is expressed as

$$W = \mu \sum_{i=1}^{5} \frac{C_i}{\lambda_m^{2i-2}} (\bar{I}_1^i - 3^i) \quad (5.3)$$

Where μ is the initial shear modulus, λ_m is extensibility limiter and C_i are material constants demonstrated in equation 5.6.

The calibration process was based on fitting the Cauchy stress of the three models to the true stresses obtained from the experimental work ($\sigma_{True} = \sigma_{Engineering}\ [1+ \varepsilon_{Engineering}]$). The uniaxial cauchy stresses of the three models are expressed as

$$\sigma_{Yeoh} = (C_{10} + 2C_{20}\,(I_1 - 3)^2 + 3C_{30}\,(I_1 - 3)^3)\,(2\lambda^2 - 2\lambda^{-1}) \quad (5.4)$$

$$\sigma_{Arruda\text{-}Boyce} = \mu\,\left(\frac{1}{2} + \frac{I_1}{10\lambda_m} + \frac{33I_1^2}{1050\lambda_m^4} + \frac{76I_1^3}{7050\lambda_m^6} + \frac{519I_1^4}{134750\lambda_m^8}\right)(2\lambda^2 - 2\lambda^{-1}) \quad (5.5)$$

$$\sigma_{Ogden} = \sum_{i=1}^{3} \frac{2\mu_i}{\alpha_i}\,\left(\lambda^{\alpha_i} - \lambda^{-\frac{\alpha_i}{2}}\right) \quad (5.6)$$

The mechanism of cavity expansion test is different from conventional stretching techniques. It is based on stretching the cavity wall on the circumferential direction while a compressive pressure is applied in the radial direction from the same wall. A relation that relates the applied pressure (P), which is equivalent to σ_r at the cavity wall, and the tangential deformation term (λ) can be defined as

$$\frac{d\sigma_r}{d\lambda} = \frac{2(\sigma_\theta - \sigma_r)}{(\lambda^4 - \lambda)} \quad (5.7)$$

σ_r and σ_θ are evaluated from equations 3.14 and 3.15. The stretch (λ) in the cavity test is defined as the ratio between the current radius and the original radius of the cavity (r/R). R was set to be 1.393 mm (see Appendix B), and r was evaluated as

$$r = \sqrt[3]{\frac{3(V_i + V_{app})}{4\pi}} \tag{5.8}$$

Where V_i is the initial volume which considers the volume of the balloon region before inflation in addition to the water volume that is introduced into the balloon before the hydrogel starts to resist inflation as will be discussed in the discussion section. V_{app} is the injected volume of water during the injection process.

5.3. Results

5.3.1. *Experimental Results*

This section presents the experimental results obtained from the uniaxial tension and the cavity expansion tests. Five specimens were tested in both tests. Due to the isotropy of the PVA hydrogels, the specimens showed relatively similar response with low standard deviation, thus only the averaged experimental data from both tests were reported in this section. In both tests, the material parameters of the SEFs were evaluated using the least squares method.

In the tensile test, the data obtained from the experiment was in force-displacement form; this data was converted into true stress (σ) - stretch (λ). The PVA hydrogel showed an ultimate stress (σ_{ult}) of 0.6 MPa at an ultimate deformation (λ_{ult}) of 2.1. The stress-stretch data was then used as a reference for calibrating equations 5.4, 5.5, and 5.6, see Figure 5.4 (a and c).

The data obtained from the pressure sensor (Pressure vs time) was used as a representative of the gel response. The data was collected until a drop in the pressure readings was observed at an injected volume ($\approx$105 µl) far higher than the balloon's designed volume (64 µl), which indicated the rupture of the cavity wall at an ultimate pressure (P_{ult}) of 0.098 MPa. The P-V data was converted into P-λ by using equation 5.8 and $\lambda = \frac{r}{R}$, Figure 5.4 b. The initial radius "R" was calculated as the radius of an initial volume that combines the volume of water introduced into the balloon before the gel starts to resist inflation, which was 8.502 µl, in addition to the volume of the balloon region as will be discussed in the discussion section. Lastly, a range of tangent moduli were calculated along the P-λ data to allow calibrating the hyperelastic models through equation 5.7, see Figure 5.4 d. The material parameters of the SEFs from both tests are summarized in table 5.1.

Table 5. 1. Coefficients of the three SEF in uniaxial tension and cavity expansion tests.

Material coefficient	Uniaxial test	Cavity test
Yeoh Model		
C_{10} (MPa)	1e-02	1.075-02
C_{20} (MPa)	2.456e-02	3.916e-03
C_{30} (MPa)	-3.332e-03	7.234e-04
Ogden Model (N=3)		
μ_1	-2.434	0.345
α_1	0.422	3.312
μ_2	1.413	4.63e-04
α_2	1.237	10.768
μ_3	1.042	-0.319
α_3	-0.313	2.368
Arruda-Boyce model		
μ	2.2e-02	1.36e-02
λ_m	1.124	1.21

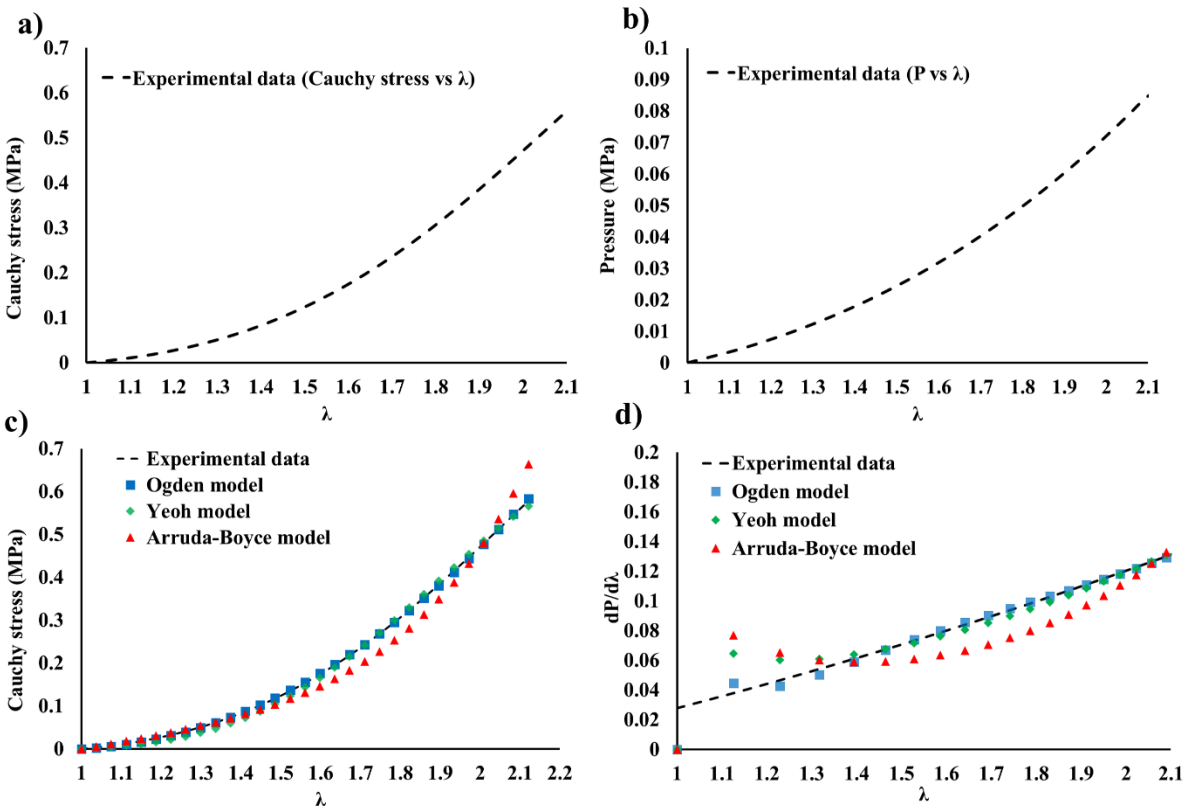

Figure 5. 4. Calibrating the hyperelastic models. a) Uniaxial tensile test. b) Cavity expansion test. c) Calibrating the three SEFs based on the uniaxial tension test data. d) Calibrating the three SEFs based on the cavity expansion test data.

5.3.2. *Numerical simulations*

Finite Element Method (FEM) is commonly used to provide an application to the calibrated hyperelastic models. In this section, two simulations are described. Abaqus® was used to reproduce the experimental results obtained from uniaxial tension and cavity expansion. The material parameters of Yeoh, Ogden, and Arruda-Boyce models were calibrated and then input into Abaqus FEM models.

In uniaxial tension simulations, three dimensional standard 8-node linear brick elements (C3D8 in Abaqus notations) were used to model the hydrogel specimens. A fixed displacement was applied to the nodes located at the top clamping region while the bottom-clamping region was fixed by ENCASTRE constraint. The load corresponding to the imposed deformation was obtained by summation of reaction forces at nodes located in the lower gripping region. The comparison between the numerical and experimental data is shown in Figure 5.5.

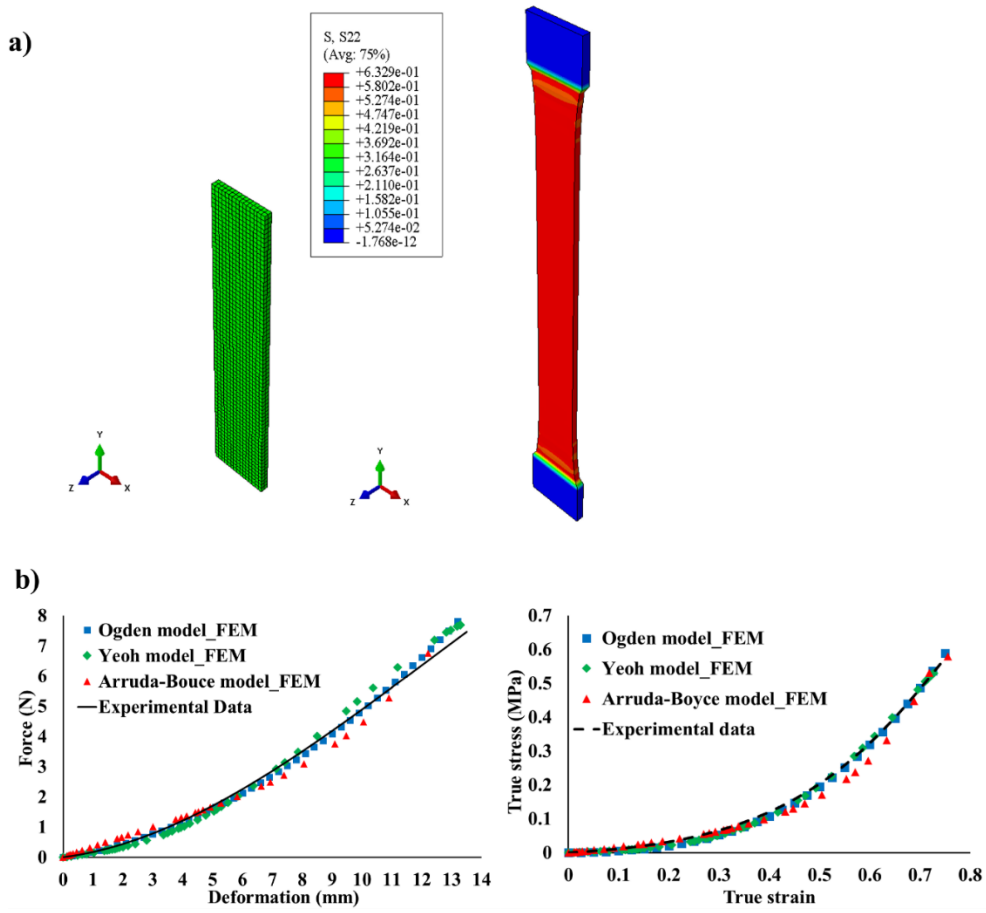

Figure 5. 5. a) FEM simulation of the uniaxial stretching. b) A comparison between experimental and numerical data.

In the cavity expansion test simulation, the hydrogel was modeled using axisymmetric quadrilateral elements with hybrid formulation (CAX4H). The model dimensions were 40 mm by 18 mm representing the height and radius of the actual specimens. The model had an initial cavity on which the pressure observed during the experiment was applied. The bottom surface of the model was constrained by using pin constraint. Along the symmetry axis, the hydrogel was prevented from moving horizontally. In addition, the lateral circumference was not constrained as no confinement was applied to the specimens during the test. Experimental and numerical results were compared based on P-λ and σ_θ-ε_θ data, where ε_θ is the hoop logarithmic strain (ln λ). See Figure 5.6.

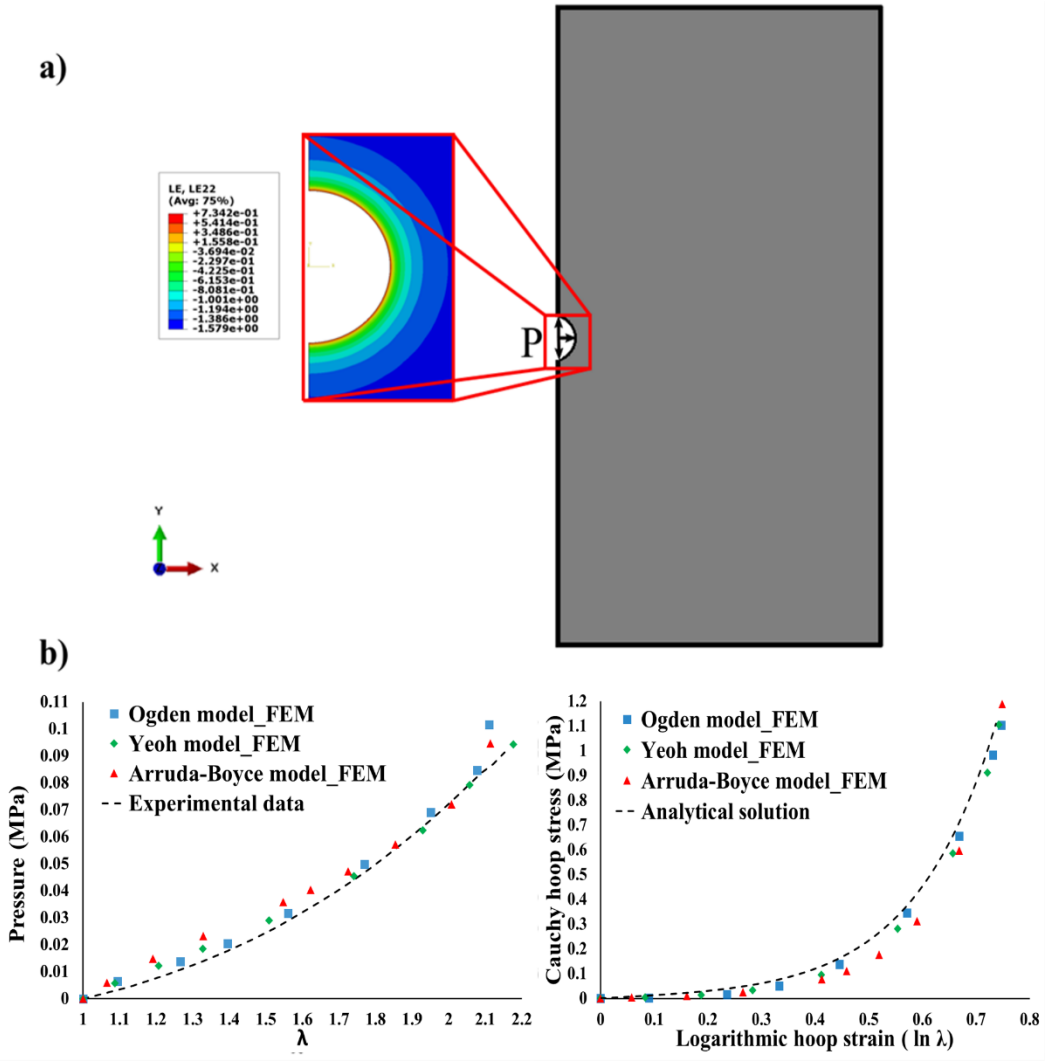

Figure 5. 6. a) FEM simulation of the cavity expansion. b) A comparison between experimental, analytical and numerical data.

In both of the investigated deformation states, the fitted models gave a numerical description that was in a robust agreement with the experimental data and the analytical solution described in section 4.

5.4. Discussion

In this work, PVA hydrogels were tested using two techniques, cavity expansion method and standard uniaxial tensile test. The experimental data were used to calibrate three SEFs. To validate the material parameters of the SEFs, FE simulations were performed to reproduce the experimental results numerically. The three models predicted consistent initial shear moduli (20 kPa – 26 kPa) in both tests. However, Arruda-Boyce model predicted an initial shear modulus from the cavity test that was less than that predicted by the other models, see table 5.2. Comparison of the tension stresses observed in both techniques shows that PVA hydrogels experienced the same level of stresses up to a strain level of 45 %. At this level of deformation, the gels showed similar response in both of the loading mechanisms. As the strain level increased, the gels subjected to expanding cavities experienced an exponential increase in hoop stresses, as shown in Figure 5.7 a using Yeoh model. Similar response was observed in other rubber-like elastomers when tested by uniaxial and equi-biaxial tensile tests (Alexander, 1968; Mansouri & Darijani, 2014); during the expansion of the cavity, the cavity wall creates a confinement equivalent to that in the equi-biaxial stretching which results in large stresses in two directions along the circumference of the cavity wall.

Table 5. 2. Values of initial shear modulus predicted by SEFs from Uniaxial tension, and cavity based biaxial tension.

	Initial shear modulus, μ (kPa)	
	Uniaxial tension (kPa)	**Biaxial tension (kPa)**
Ogden model	21	26.5
Yeoh model	20	21.5
Arruda-Boyce model	22	13.6

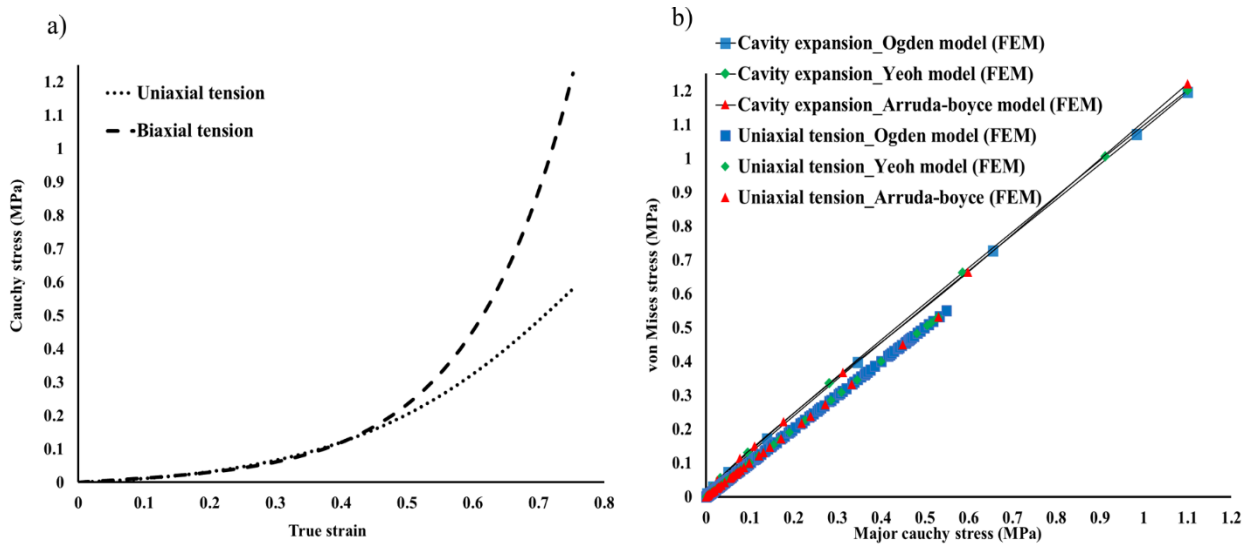

Figure 5. 7. a) Cauchy stress vs Logarithmic strain using Yeoh model. b) Stretching stresses generated in the uniaxial tensile test and the cavity expansion test. The term major refers to the tension stresses in both tests. Von Mises was used as an equivalent stress in both techniques.

The maximum stretching deformation was over 200% ($\lambda \approx 2.1$) in both tests. This magnitude agrees with the range reported in (Afghan, 2016) ($\lambda = 1.8 – 2.8$) for 10% w/w PVA hydrogels. The maximum stretching stress in the cavity expansion test was found to be twice the maximum stretching stress in the uniaxial tensile test, a common behavior of isotropic rubber-like elastomers when loaded in uniaxial and biaxial (equal) directions (Kim et al., 2010; Song et al., 2004; Szabó & Váradi, 2018; Uddin & Ju, 2016). This can be observed by comparing the equivalent (von Mises) stress against the major stress of both tests, see (Figure 5.7 b). This ratio indicates that the cavity expansion test is capable of measuring the stretching mechanics of the PVA hydrogels by stretching its material into two orthogonal directions simultaneously at the cavity wall. The three-hyperelastic models predicted the maximum hoop stress to be significantly larger than the maximum observed pressure. Thus, the effect of the pressure is insignificant in determining the equivalent stress, which indicates that the cavity expands by stretching the material structure leading to a tension-controlled rupture on the cavity wall.

For a comprehensive evaluation of all components including syringe, balloon and needle used in the cavity expansion test, force-displacement data was also collected using the Instron machine to compress the syringe plunger while monitoring its movement using the machine built-in LVDT. As shown in Figure 5.8 a. The friction response of the rubber stopper on the syringe's barrel started with a typical break loose (static friction) force followed by the gliding force (dynamic friction),

similar to the syringe force mechanism reported in (Chan et al., 2012). A stiffening was observed at the tail of the gliding force (t = 26 sec) due to the resistance of the balloon material to expansion at a volume of 120 μl representing ≈180% the design spherical volume of the balloon. It is also worth mentioning that, the stiffening occurred at a volume beyond that at which the gels' cavity walls have ruptured, which indicates that the balloon material had no effect on the data observed during the cavity expansion test.

The pressure observed from the load cell and the pressure sensor showed similar behavior, as shown in Figure 5.8 b. The analysis of the obtained data was based on the range of data at which the observed pressure started to increase until an ultimate magnitude where failure occurred.
The definition of the stretch term (λ) was based on the magnitude of the initial radius (R = 1.393 mm). This magnitude was found to be dependent on an initial volume, which consists of the volume of water that was introduced into the balloon until the gel started to resist balloon inflation (V_p = 8.502 μl), in addition to the volume of the balloon region ($V_{n\text{-}b}$ = 2.837 mm^3). No pressure loads were observed by the pressure sensor as V_p was introduced into the balloon. This could be due to the displacement of the channel walls created by the needle shaft along the balloon region, which initially relieves the restriction imposed by the gel structure on the balloon. Thus, it encounters no resistance during initial inflation. At this low volume, the balloon is still, predominantly, in its cylindrical form, however, as the injected volume increased, the balloon started to take on its spherical shape imposing spherical cavity deformations on the hydrogel's structure. This hypothesis can be verified by observing the balloon expansion inside a transparent polymer using an optical microscope (e.g. Keyence Model VHX 5000), which will be addressed in a future study.

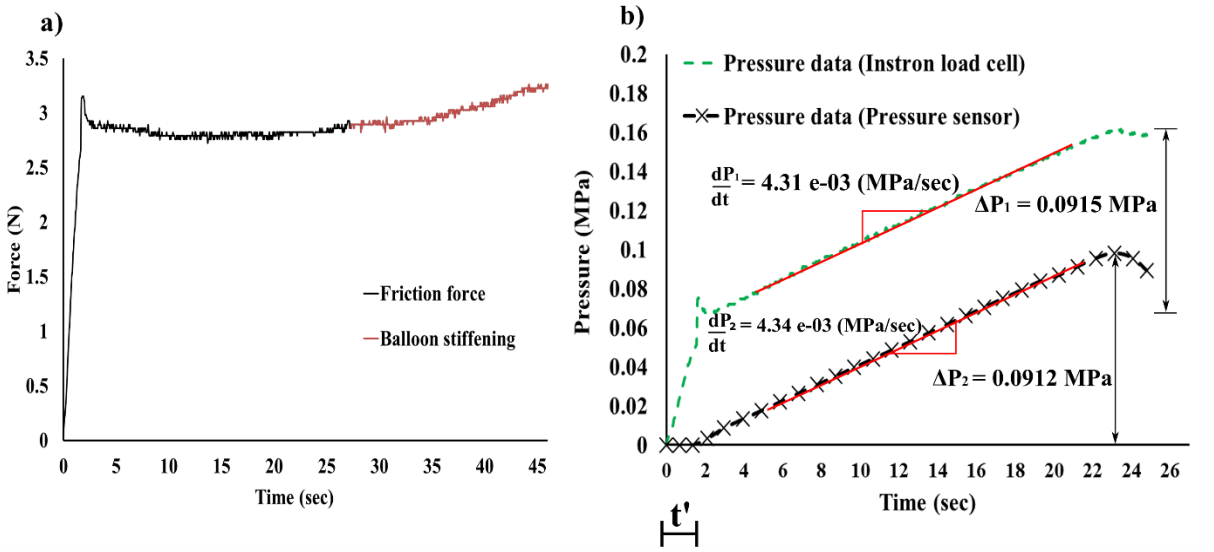

Figure 5. 8. a) The balloon response during the inflation process. b) Comparison between the data obtained from the pressure sensor and the Instron machine's load cell. The observed pressure: $\frac{\Delta P_1}{\Delta t}$ represents the rate of change of the pressure calculated from the force data, the barrel's inner radius was used to convert the force data into pressure; $\frac{\Delta P_2}{\Delta t}$ represents the rate of change of the pressure observed by the pressure sensor; the time (t') at which the gel started to resist the balloon inflation was 1.7 sec.

5.5. Conclusions

The mechanical properties of PVA hydrogels were characterized by uniaxial tension and cavity expansion tests. The purpose of implementing these two techniques was to understand the mechanism of the cavity expansion technique by comparing it to a reference conventional method (uniaxial tensile test). The experimental data from both tests were used to calibrate Yeoh, Ogden, and Arruda-Boyce models. The parameters of these models were used in FE simulations and reproduced the experimental data numerically. In addition, the material parameters were used to predict the hoop stresses analytically and numerically to compare the behaviour of the PVA hydrogels under two different types of loading. It was found that the cavity expansion test generated similar initial shear moduli to those generated in the uniaxial tensile test. In addition, maximum hoop stresses generated in the cavity expansion test were twice those generated during the uniaxial tensile test. Moreover, the observed pressure was insignificant compared to the hoop stresses, thus, the cavity expansion test can be considered as an equi-biaxial tensile test.

Chapter 6

Mechanical Characterization of PVA Hydrogels' Rate-Dependent Response Using Multi-Axial Loading

Abstract

The time-dependent properties of rubber-like synthesized and biological materials are crucial for their applications. These properties determine the efficiency of their performance and function. Currently, this behavior is mainly measured using axial tension and compression loading, or indentation. Limited studies addressed multi-axial loading (loads applied in more than two directions) to measure time-dependent material behavior exist in the literature. Therefore, the aim of this study is to investigate the viscoelastic response of rubber-like materials under multi-axial loading using cavity expansion and relaxation tests. The tests were conducted using PVA hydrogel specimens. Three hyperelastic models and one term Prony series were used to characterize the viscoelastic response of the hydrogels. FE simulations were performed to verify the validity of the calibrated material coefficients by reproducing the experimental results. The excellent agreement between the experimental, analytical and numerical data proves the capability of the cavity expansion technique to measure the time-dependent behavior of viscoelastic materials.

6.1. Introduction

Rubber-like materials are known for their viscoelastic behavior. Elaborate characterization of this behavior is crucial to numerous applications in a variety of engineering fields and industries. The time-dependent properties of these materials control their mechanical response, not only under thermal conditions (Kiss et al., 2009; Lu & Shinozaki, 2010), but also when large deformations are applied at different rates (Rashid et al., 2014b; Siviour, 2017). Thus, these properties have been the focus of numerous studies that utilized different mechanical characterization techniques.

In the biomedical field, studying the viscoelastic properties of biological tissues indicated that their mechanical properties change based on their pathological conditions. For instance, fibrosis was reported to change the viscoelastic behavior of liver tissues (Deffieux et al., 2015). This change occurs at early stages of fibrosis mainly due to degeneration of fatty tissues (Salameh et al., 2009). The mechanical quantification of such diseases at early stages is very critical for remedy processes. Currently, the measurement of the mechanical properties of diseased and healthy tissues in-vivo is

commonly achieved using transient elastography (TE) (Kennedy et al., 2018; Zhao et al., 2017). Although this technique is capable of measuring the mechanics of the tissues, it is only capable of quantifying their Young's modulus. While this physical property is meaningful in small deformations, it does not fully represent the non-linear elastic response of the biological tissues. On the other hand, TE proved to be efficient in measuring the viscous (relaxation) response of these tissues in-vivo (Chatelin et al., 2011).

In general, numerous theories have been developed to describe the time-dependent response of different materials. Those theories describe materials as linear viscoelastic (LVE) (Ian Macmillan Ward, 1983), quasi-linear viscoelastic (QVL) (Fung, 1993), and non-linear viscoelastic (NVE) (Findley et al., 1976; Yannas, 1974). The LVE description is the most common due to its simplicity in addition to the validity of the superposition principal it utilizes. Moreover it has been thoroughly examined mathematically (Christensen, 2012), and experimentally (Ward & Sweeney, 2004). It is also available in all commercial FE packages. Therefore, it is the focus in this study.

The implementation of the LVE theory is based on combining the instantaneous elastic response of a given material with its viscous behavior. This behavior is commonly measured by the creep test (Leng et al., 2019), or the relaxation test (Dong et al., 2017), including in-vivo characterization in cases of biological tissues (Chatelin et al., 2011). The elastic behavior is measured commonly by using axial loading and indentation (Kendall & Siviour, 2015; Nafo & Al-Mayah, 2018; Zhai & McKenna, 2014). These conventional techniques are used to measure the material response under different deformation rates. Although uniaxial loading is very common when studying the mechanics of viscoelastic materials, little attention, to our knowledge, has been paid to viscoelasticity characterization using multi axial loading. Thus, in this work, we aim to investigate the viscoelastic properties of a rubber-like material under different rates by using cavity-based multi-axial loading (pressure + equi-biaxial tension). This technique is based on inducing an expanding cavity within the structure of soft materials by using a balloon and an incompressible fluid. This technique was found to be efficient in measuring the hyperelastic properties of rubber-like materials and biological tissues (Nafo & Al-Mayah, 2019; Nafo, 2016). Therefore, it represents a good option to investigate the rate-dependent behavior of such materials under the effect of multi-axial loading.

A hyperelastic material that exhibits the LVE behavior is PVA hydrogel as will be demonstrated in this study. These hydrogels are considered excellent candidates to be alternatives to biological tissues due to their high hydrophobicity (Lee et al., 2005; Stammen et al., 2001), biocompatibility (Shi & Xiong, 2013), mechanical strength (S.-Y. Lee et al., 2009; D. Zhang et al., 2012), physical integrity under large deformation (Nafo & Al-Mayah, 2019; Wan et al., 2002), viscoelastic properties (Ahsanizadeh & Li, 2015; Hernández et al., 2004), thermal stability and non-toxicity (Liu et al., 2012). Thus, they are the most suitable material for this study. Cavity expansion tests and simple shear relaxation tests are conducted to measure the instantaneous and long term behaviors of PVA hydrogels, respectively. The data obtained from these tests will be used to calibrate the material constants of hyperelastic models (Yeoh, Arruda-Boyce and Ogden), and the Prony series viscoelastic model coefficients. Finally, FE simulations are going to be performed to reproduce the time dependent behavior of PVA hydrogels.

6.2. Material and Methods

6.2.1. *Samples Preparations*

This study is based on using the cavity expansion and the relaxation tests to measure the instantaneous and time-dependent behaviors of the PVA hydrogels, respectively; thus, twelve cylindrical (40mm in height and 36 mm in diameter). The synthesis process was based on physically crosslinking a PVA solution. The solution was made by mixing 99+% hydrolyzed PVA (molecular weight of 146000-186000 $g.mol^{-1}$ with deionized water (10% w/w ratio) at 90 ^{o}C by using standard flask/column combination. Thereafter, the solution was poured into cylindrical molds. The hydrogels were formed by freezing the solution at -20 ^{o}C for 3 hours and then thawing at room temperature $\sim$ 21 ^{o}C for 3 hours. This freeze-thaw cycle (FTC) was repeated two times. Thereafter, three gel cylinders were cut into smaller cylinders (5mm in height) then punched in the middle to create rectangular cuboid samples with dimensions of 20 mm in length, 10 mm in width and 5 mm in thickness. Figure 6.1 shows the samples' geometry for both cavity expansion and shear tests.

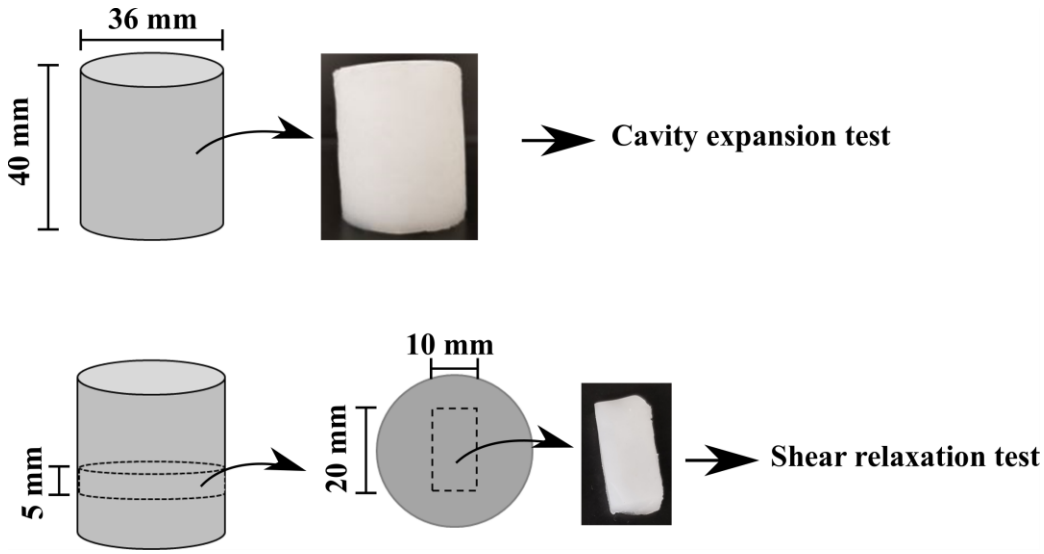

Figure 6. 1. PVA hydrogels samples' geometry. The cylindrical samples will be used in the cavity test, and the cuboid samples will be used in simple shear relaxation tests.

6.2.2. *Experimental Setup*

- **Cavity Expansion Test**

The procedure followed in (Nafo & Al-Mayah, 2019) was adopted to perform the cavity test. However, few changes were made to the system that was used: pressure sensor (Model PRESS-S-000, PENDOTECH, USA) and pressure reader (Model PMAT-S, PENDOTECH, USA) were used to observe the pressure due to the pressurized incompressible fluid (water). In addition, an Instron machine (Model 4465; Canton, MA, USA) was used to introduce the water into the needle-balloon tool. A new design needle-balloon tool was used in this study, the balloon is silicon based with smaller dimensions and has softer mechanical behavior than the one used in chapter 3. To ensure no air was entrapped inside the system, its elements (syringe, needle-balloon tool and Y-shaped tubes) were filled with water and submerged under water until they sank and assembled together. Afterwards, the tubes were connected to the pressure sensor with a water inlet and outlet, which allows depleting any remaining air in the system. Nine hydrogels were investigated by this test at three different deformation rates: 5 µl/s, 20 µl/s and 50 µl/s. A schematic diagram for the system is shown in Figure 6.2. In addition, the balloon response was evaluated separately using the Instron machine.

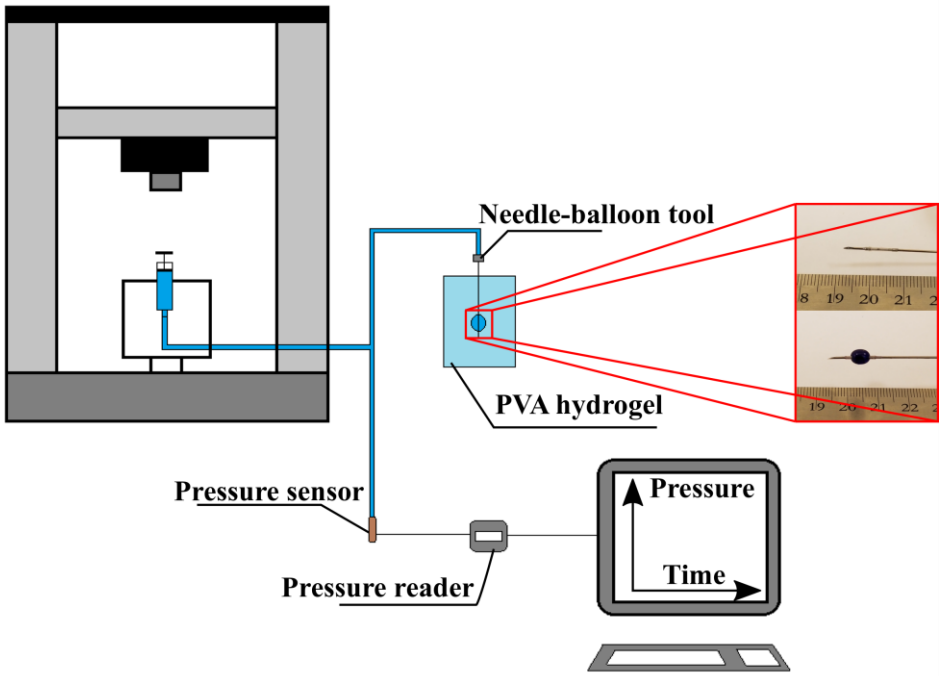

Figure 6. 2. The loading set up of the cavity expansion test.

- **Relaxation Test**

This test was performed on the gel cuboids; they were subjected to simple shear relaxation test. Acrylic platens (50 mm x 20 mm x 2.5 mm) were machined with spacers glued to the platens to ensure a good alignment as well as to avoid overstressing of the gel specimens. The top and the bottom surfaces of the cuboid specimens were placed and glued between the platens with a thin layer of a fast-acting adhesive. The assembly was then mounted on the Instron machine and loaded at a rate of 0.1 s^{-1}. The relaxation test was performed at various shear strains: 10 %, 20 %, 30 %, 40 %, 50 %, 60 %, 70 % and 80 % to investigate the behavior of the hydrogels in a step-like strain at various magnitudes. Figure 6.3 shows the loading configuration for the simple shear relaxation test.

Figure 6. 3. The loading configuration for the shear relaxation tests: the cuboid was subjected to 50 % shear strain and left to relax for 300 seconds.

6.3. Analytical Framework

In this work, the time-dependency of the PVA hydrogel behavior is modelled as LVE. This description is considered accurate for the tested gels as will be shown in section 6.4. A general description of the LVE material stress in large deformations at time (t) can be given as (Bergstrom, 2015)

$$\sigma(t) = \sigma_0\,(\varepsilon(t)) - \int_0^t \dot{g}(t-\boldsymbol{\tau})\;\sigma_0\big(\varepsilon(t)\big)\mathrm{d}\boldsymbol{\tau} \tag{6.1}$$

The first term represents the hyperelastic stress function ($\sigma_{h.el}$). The second term represents Prony series expression of stress relaxation function ($\sigma_{v.el}$).

At time t+Δt, and by using "N" number of terms in the Prony series, equation 6.1 can be expressed as

$$\sigma(t+\Delta t) = \sigma_{h.el}(t+\Delta t) - \sum_{i=1}^{N} \sigma^{i}_{v.el}(t+\Delta t) \tag{6.2}$$

$\sigma_{h.el}(t+\Delta t)$ can be evaluated by using material parameters of a calibrated strain energy function (SEF),

And, $\sigma^{i}_{v.el}(t+\Delta t)$ can be expressed as

$$\sigma^{i}_{v.el}(t+\Delta t) = e^{-\frac{\Delta t}{\tau_i}} \cdot \sigma^{i}_{v.el}\,(t) + g_i \cdot \sigma_{h.el}(t)\left[1 - e^{-\frac{\Delta t}{\tau_i}}\right] + g_i\,\frac{\Delta\sigma_{h.el}}{\Delta t}\left[(\Delta t - \tau_i) + \tau_i\, e^{-\frac{\Delta t}{\tau_i}}\right] \tag{6.3}$$

Where g_i and $\boldsymbol{\tau}_i$ are the relaxation parameters. See (Bergstrom, 2015) for full derivation.

A number of strain energy functions (SEFs) are reported in literature. In this work, we focus only on three SEFs, namely: Yeoh, Ogden and Arruda-Boyce. These models are available in most of commercial FE software packages; in addition, they proved to be efficient in capturing the non-linear elastic response of rubber-like materials subjected to uniaxial loading, biaxial loading (Shahzad et al., 2015), and cavitation (Nafo & Al-Mayah, 2019). Yeoh, Ogden, and Arruda-Boyce models are expressed, respectively, as

$$W = \sum_{i=}^{N=3} C_{i0}(I_1 - 3)^i \tag{6.4}$$

$$W = \sum_{i=1}^{N=3} \frac{2\mu_i}{\alpha_i^2}\left(\lambda_1^{\alpha_i} + \lambda_2^{\alpha_i} + \lambda_3^{\alpha_i} - 3\right) \tag{6.5}$$

$$W = \mu \sum_{i=1}^{5} \frac{C_i}{\lambda_m^{2i-2}}\,(I_1^i - 3^i) \tag{6.6}$$

Where μ_i, α_i, C_{i0} and C_i are material constants; λ_m is the extensibility limiter.

In the cavity expansion test, the pressure applied on the cavity wall generates an equivalent radial stress normal to the wall and hoop circumferential stresses along the wall. These stresses can be expressed in Cauchy hyperelastic from as

$$\sigma_r = 2[W_1\lambda^{-4} + 2W_2\lambda^{-2}] \quad (6.7)$$

$$\sigma_\theta = \sigma_\varphi = 2[W_1\lambda^{2} + W_2(\lambda^{4} + \lambda^{-2})] \quad (6.8)$$

Where W_1 and W_2 are the SEF derivatives with respect to I_1 and I_2, respectively. Equation 6.8 can be used to calculate $\sigma_{h.el}(t+\Delta t)$.

For material calibration of equation 6.4, 6.5 and 6.6 in the cavity loading, we can use a tangential relationship that relates the radial stress (σ_r) and the hoop deformation (λ), see (deBotton et al., 2013; Nafo & Al-Mayah, 2019) for derivation

$$\frac{d\sigma_r}{d\lambda} = \frac{\widehat{W}}{\lambda^3 - 1} \quad (6.9)$$

Where $\widehat{W}$ is the derivative of W with respect of λ. Inputting the derivatives of equations 6.4, 6.5 and 6.6 into equation 6.9 will allow calibrating the hyperelastic term of equation 6.2.

6.4. Results

6.4.1. *Cavity Expansion Experiments*

The cavity tests were performed on cylindrical specimens at each injection rate of 5 µl/s, 20 µl/s and 50 µl/s up to a volume of 110 µl in order to investigate the behavior of the gel at particular loading rates as shown in Figure 6.4. The pressure (MPa) and time (s) data were measured directly by the system. The volume data shown in Figure 6.4 was calculated through multiplying the time data by each of the injection rates. It was observed that at the initial stage of the balloon inflation, the gels did not show any resistance for 1.96 s, 0.45 s and 0.16 s at injection rates of 5 µl/s, 20 µl/s and 50 µl/s, respectively. Multiplying these short periods of times by their corresponding volume rates will result in initial volumes (V_i) of 8.635 µl, 8.23 µl and 8.24 µl, respectively. The lack of resistance to these volumes can be due to the displacement of the channel wall created by the needle during the insertion process, which relieves any constraints against balloon inflation at early stages. Afterwards, the gel starts to resist deformation as the balloon starts to inflate spherically. During the test, the hydrogels were internally deformed to a volume of 110 µl. At this volume, the balloon material started to participate in resisting the inflation. Thus, to avoid the effect of the balloon's silicon material, all tests stopped at 110 µl. The syringe and needle-balloon tool responses were investigated separately at the lowest rate (5 µl/s) by the Instron machine, using the

built-in linear variable differential transformer (LVDT) and the load cell, see Figure 6.5. At this rate, the balloon material showed no contribution in resisting the inflation. However, at a volume of 110 µl, the force data showed hardening due to balloon material participation in resisting inflation. The effect of the friction between the rubber-stopper and the syringe plunger was also investigated, see Figure 6.6. It can be noticed that at the slow rate (5 µl/s), the dynamic friction is overall steady. However, when the injection velocity is increased, the friction between the rubber-stopped and the inner wall of the plunger makes the data more volatile.

6.4.2. *Relaxation Test*

The cuboid specimens were loaded at various shear strain levels (10 % - 80 %) and held for 300 second to record the relaxation force. The force data was then converted into stress form using the cuboid dimensions, as shown is Figure 6.7 a. The long-term shear stresses and their correspondent strains were plotted and it was found that the gel exhibited a linear long-term behavior, see Figure 6.7 b, which indicates to the validity of the LVE assumption. It is worth mentioning that stress-strain data in the simple shear test represents plane stress-plane strain behavior, i.e., the initial area (20mm x 10mm) that was used to calculate the shear test from the force data remains unchanged after loading the specimens.

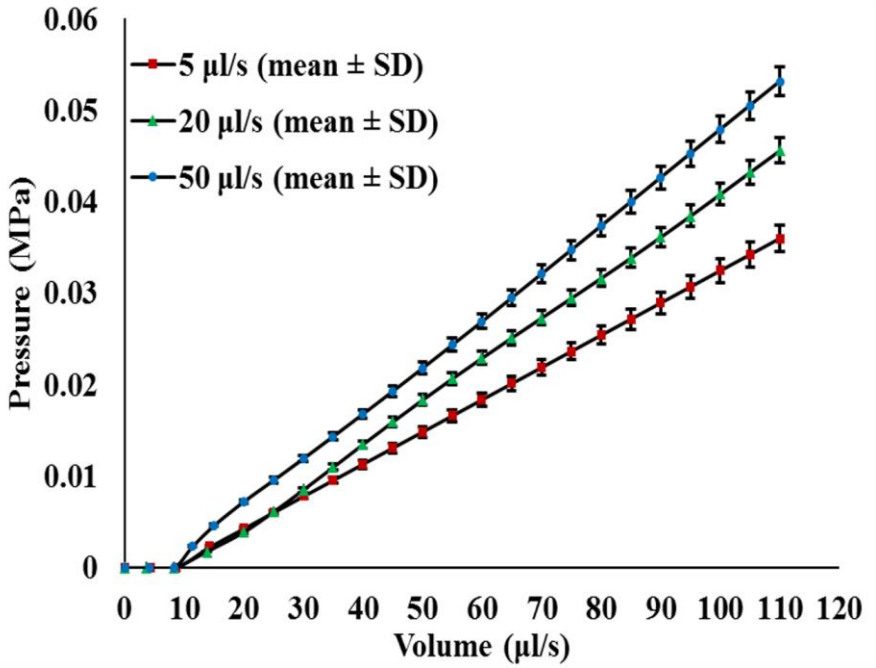

Figure 6. 4. Cavity tests performed on PVA hydrogel specimens up to 110 µl injection volume at loading velocities of 5 µl/s, 20 µl/s and 50 µl/s.

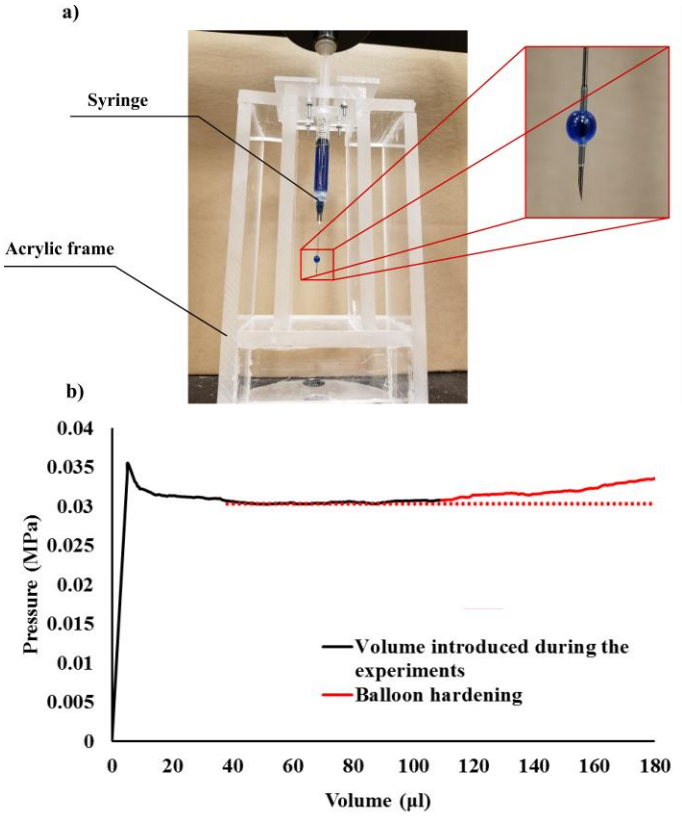

Figure 6. 5. a) Acrylic frame used in the cavity expansion test, and the balloon configuration during the inflation process. b) Balloon response.

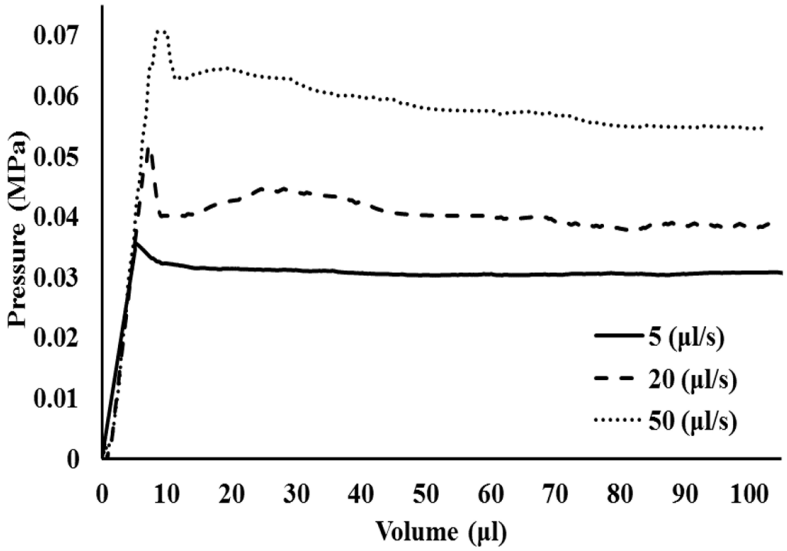

Figure 6. 6. The friction response under the three volume rates used in the cavity expansion test: the overall response starts with instantaneous increase in the friction resistance (static friction), followed by a drop and continuous resistance (dynamic friction). The dynamic friction response at the lowest rate is steady, and volatile at higher injection velocities.

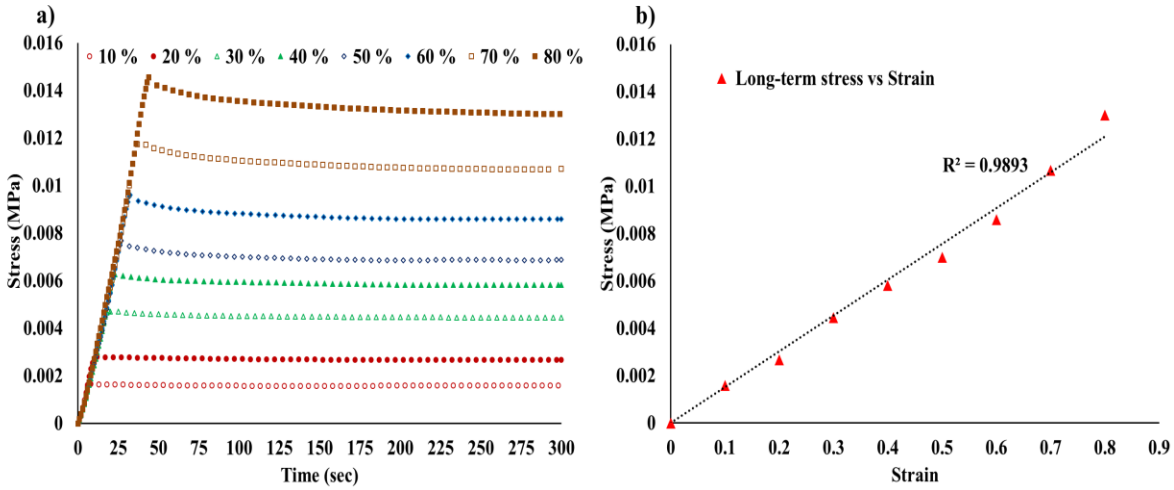

Figure 6. 7. a) Long-term shear stress at various strain magnitudes; b) the long-term shear stress-strain relationship. The high value of R^2 (0.9893) indicates to the validity of considering the material as linear viscoelastic.

6.4.3. Calibration of SEFs and Prony Series

The experimental data obtained from the cavity expansion tests were in pressure (P) – volume (V). The deformation term (V) was converted into a hoop stretch term (λ), which was calculated as $\frac{r}{R}$. "R" values were found to be 1.399 mm, 1.382 mm and 1.383 mm at injection rates of 5 µl/s, 20 µl/s and 50 µl/s, respectively. These magnitudes were calculated using the concept of Equivalent Volume Diameter (EVD) (DeCarlo et al., 2004) as follows:

$$R = \frac{\sqrt[3]{\frac{6\,V_i}{\pi}}}{2} \tag{6.10}$$

V_i can be evaluated as

$$V_i = V_{n\text{-}b} + V_p \tag{6.11}$$

Where $V_{n\text{-}b}$ is cylindrical volume (5 mm in length and 0.85 mm in diameter) of the balloon region before inflation; V_p are the volumes of water introduced into the balloon, 8.635 µl, 8.23 µl and 8.24 µl (calculated in section 4.4), before the hydrogel started to resist balloon inflation at each of injection rates, 5 µl/s, 20 µl/s, 50 µl/s, respectively.

The magnitude of "r" was calculated as

$$r = \sqrt[3]{\frac{3(V_i + V_{app})}{4\pi}} \tag{6.12}$$

Where V_{app} is the injected volumes of water during the cavity expansion test.

Figure 6.8 a. shows the experimental data in the form of P – λ of the three injection rates. The instantaneous rate of change of the three curves was calculated. Before the commencement of the calibration process, it is worth mentioning that due the local nature of the cavity expansion test, equation 6.9 can be expressed as

$$\frac{dP}{d\lambda} = \frac{\widehat{W}}{\lambda^3 - 1} \tag{6.13}$$

Which indicates that the radial stress at the cavity wall, where the material parameters are calculated, is equivalent to the applied pressure.

The resulting theoretical curves exhibited strong agreement with experimental data. Arruda-Boyce model showed the least fit, yet it is still valid, Figure 6.8 (b, c and d). The material parameters are summarized in tables 6.1, 6.2 & 6.3.

Table 6. 1. Material parameters of Yeoh model (Ci are in MPa).

	Yeoh model		
µl/s	**C_{10}**	**C_{20}**	**C_{30}**
5	1.3e-03	1.798e-03	1.594e-04
20	2.75e-03	2.57e-03	2.35e-04
50	3.5e-03	2.9e-03	3e-04

Table 6. 2. Material parameters of Arruda-Boyce model (µ is in MPa)

	Arruda-Boyce model	
µl/s	**µ**	**λ_m**
5	2.5e-03	1.127
20	5.7e-03	1.203
50	7.1e-03	1.215

Table 6. 2. Material parameters of Arruda-Boyce model (μi is in MPa).

	Ogden model					
μl/s	**μ_1**	**μ_2**	**μ_3**	**α_1**	**α_2**	**α_3**
5	5.14e-02	1.106e-02	-6e-02	0.0378	6.126	0.679
20	1.6e-02	4.09e-02	-5.15e-02	6.24e-02	5.147	2.833
50	3.39e-02	3.83e-02	-6.5e-02	0.5402	5.317	2.059

The initial shear moduli of the PVA hydrogels can also be estimated from the calibrated material parameters at each deformation rate. These moduli are summarized in Table 6.3.

Table 6. 3. Initial shear moduli estimated by the SEFs at the three deformation rates.

μl/s	**$\mu_{Yeoh} = 2C_{10}$ (MPa)**	**$\mu_{Arruda\text{-}Boyce} = \mu$ (MPa)**	**$\mu_{Ogden} = \sum \mu_i$ (MPa)**
5	2.6e-03	2.5e-03	2.46e-03
20	5.5e-03	5.7e-03	5.4e-03
50	7e-03	7.1e-03	7.2e-03

In this work, Abaqus® software package was used to evaluate the Prony series coefficient using its built-in calibration tool. The long-term shear stress data, shown in Figure 6.7, was converted into shear moduli data, and then normalized and input in Abaqus® to run the calibration process. One term Prony series achieved an excellent fit to the relaxation response of the hydrogel, see Figure 6.9. The Prony series coefficients were g = 7.837e-02 and $\boldsymbol{\tau}$ = 47.845 s.

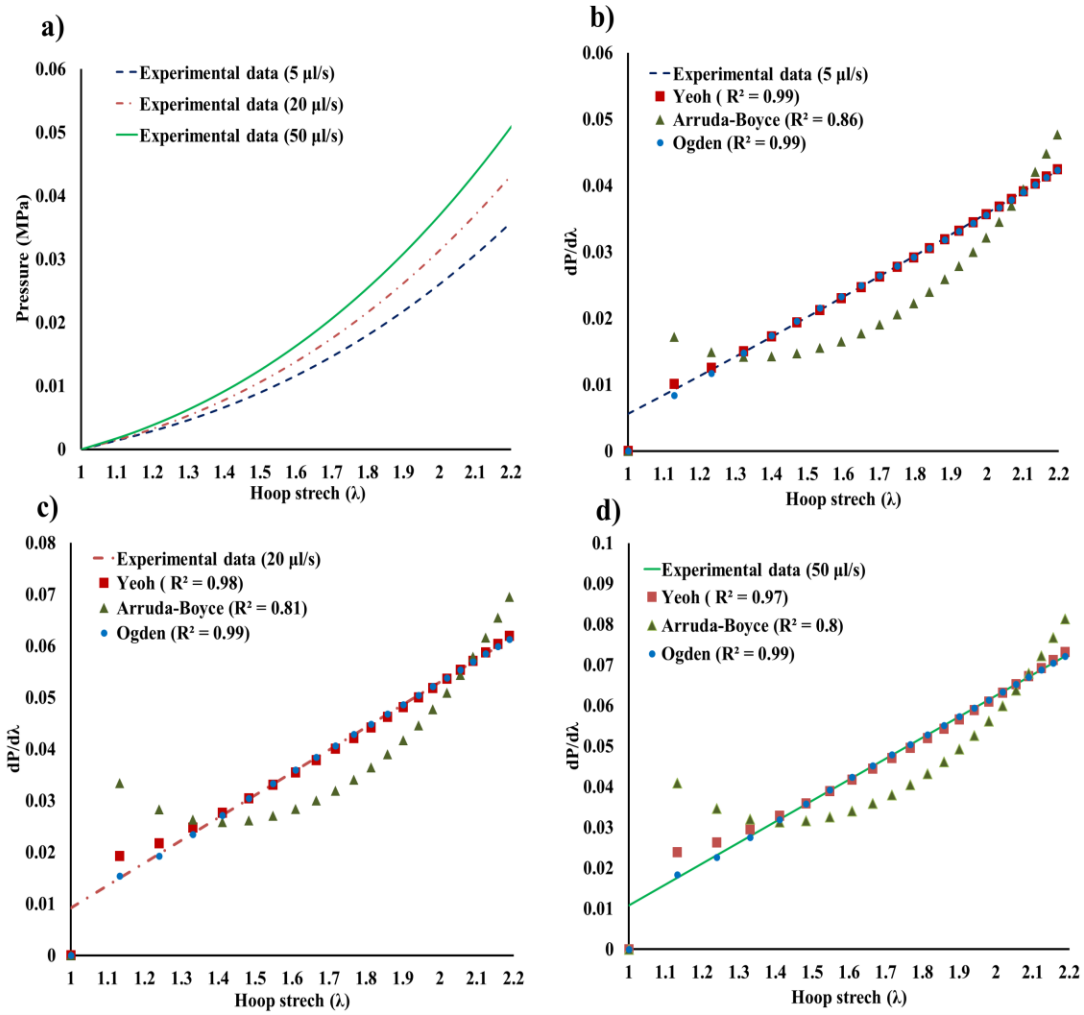

Figure 6. 8. a) Experimental data (P – λ). Segments b, c and d show the agreement between the SEFs and the instantaneous rate of change derived from the experimental data at injection rates of 5 µl/s, 20 µl/s and 50 µl/s, respectively.

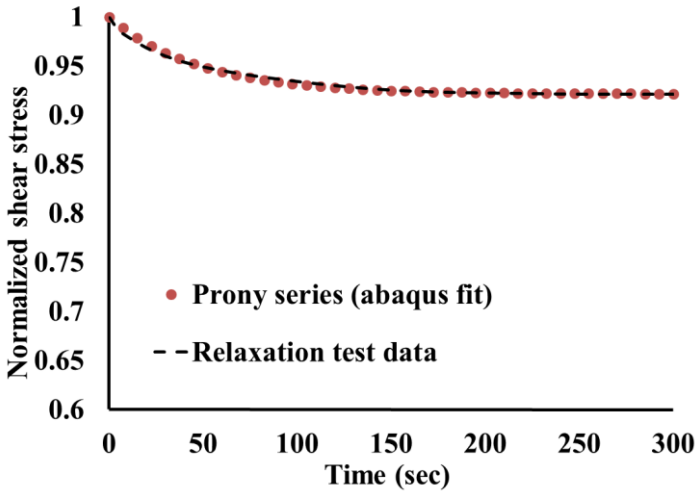

Figure 6. 9. Comparison between the relaxation test data and the Prony series function.

6.5. Finite Element Analysis

Most of the reported work on the viscoelasticity of PVA hydrogels was describing the material as QLV (Karimi et al., 2014; Li et al., 2018). Thus, it was necessary to validate the predictable behavior of the LVE description adopted in this study (using the material parameters of the SEFs and the coefficients of Prony series) using numerical simulations, an analytical solution and measured experimental data.

In order to reproduce the experimental results, FE simulations were performed using Abaqus® by implementing the model described in (Nafo & Al-Mayah, 2019), and the material parameters obtained in section 6.4. A mass density of 1030 kg/m^3 ($\pm$ 65 kg/m^3) was used for the model's elements (CAX4H). This magnitude was estimated by using Archimedes principal. The observed pressure during the experiments was applied in the FE simulations.

The numerical results showed an excellent agreement with the experimental data. In addition, they predicted numerical hoop stresses that are in robust agreement with the analytical hoop stresses, see Figure 6.10. Analytical hoop stresses were calculated using equation 6.2 which was implemented using Matlab®, see Appendix C for an example solution using Yeoh model for 50 µl/s data. The two agreements at each of the deformation rates indicate to the strong validity of the calibrated material parameters of the implemented SEFs.

The data obtained from the cavity tests were experimental P-λ. The SEFs' parameters, used to fit experimental data as well as to predict the σ_θ - ε_θ data analytically, were verified by using FE. The root mean square (RMS) error was calculated to evaluate the difference between the realistic data (experimental and analytical) and the reproduced data (numerical). The error values are summarized in table 6.4.

$$\text{RMS error} = \frac{1}{N}\sqrt{\sum_{i=1}^{N}\frac{\text{Load}_{\text{experimental or analtical}} - \text{load}_{\text{FE}}}{\text{Load}_{\text{exp}}}} \tag{6.14}$$

Table 6. 4. RMS error values for each of the SEFs.

µl/s	Yeoh model		Arruda-Boyce model		Ogden model	
	Pressure data	Hoop stress data	Pressure data	Hoop stress data	Pressure data	Hoop stress data
5	3.1 %	4.1 %	7.7 %	9.5 %	3.5 %	2.4 %
20	1.9 %	3.8 %	9.8 %	8.6 %	2.4 %	3.6 %
50	2 %	4.1 %	9.1 %	9 %	3.4 %	3.4 %

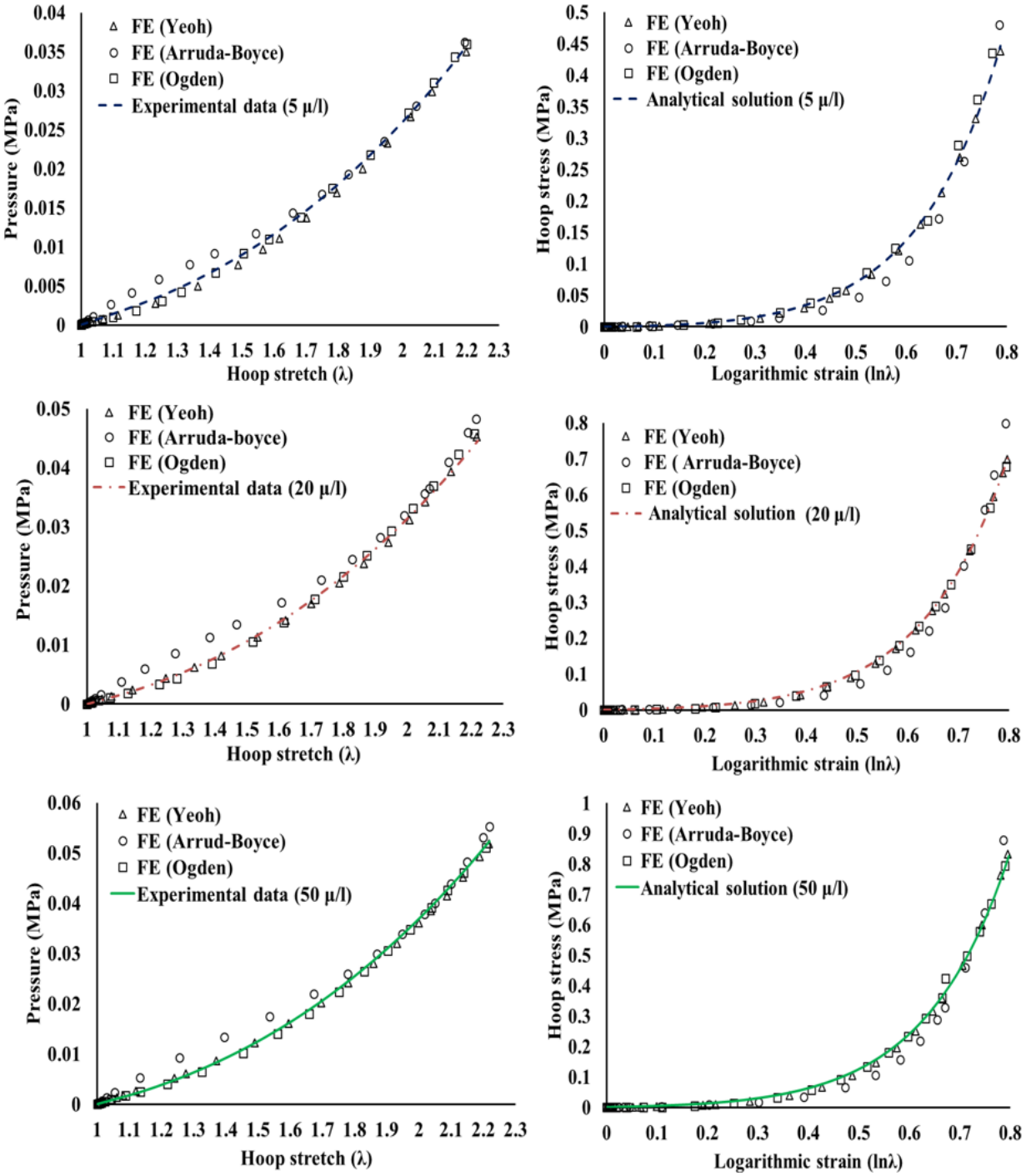

Figure 6. 10. The numerical results compared against the experimental pressure and the analytical hoop stress at each deformation rate.

6.6. Discussion

The characterization of PVA hydrogel using cavity expansion at different deformation rates allows measuring the rate-dependent response of rubber-like materials in multi-axial loading. In this research, the properties of PVA hydrogels subjected to cavitation have been characterized up to 80 % hoop logarithmic strain at deformation rates of 5 μl/s, 20 μl/s and 50 μl/s. Force relaxation experiments in simple shear were also performed at various strain magnitudes (10 % - 80 %).

The parameters of the three SEFs were calibrated through equation 6.9, while the time-dependent Prony coefficients were calibrated using Abaqus' calibration tool. Overall, the good agreement between the numerical, experimental and analytical results indicates that the three SEFs are suitable to model the viscoelastic behavior of the PVA hydrogels up to 80 % strain.

The initial shear moduli of the PVA hydrogels were estimated by the SEFs to be ≈ 2.5 kPa, 5.5 kPa and 7 kPa at deformation rates of 5 μl/s, 20 μl/s and 50 μl/s, respectively. While the three models predicted similar initial shear moduli at each deformation rate, the overall performance of Arruda-Boyce model in data fitting was the least sufficient. This is due to the limited number of parameters unlike the other two phenomenological models. However, Arruda-Boyce model has the capacity to predict the material response in other forms of loading using the same material parameters due to its micromechanical nature (use of eight Langevin chains network) (Arruda & Boyce, 1993; Steinmann et al., 2012), an advantage that does not exist in other empirical models such as Yeoh and Ogden.

In this study, the PVA hydrogels were considered incompressible. This assumption was based on the very low compressibility nature of this type of gels. Nafo & Al-Mayah, 2019 reported that there is no significant difference between the compressible and incompressible assumptions in simulating the behavior of PVA hydrogels subjected to cavity loads. In addition, Chen et al., 2013 reported a relatively high Poisson's ratio for this type of hydrogels (≈ 0.5); thus, we considered the gels as incompressible materials in this study. It is also worth mentioning that the volumetric behavior of most rubber-like materials has very little or no time-dependency (Dalrymple et al., 2007). Therefore, only the relaxation parameters (g_i and $\boldsymbol{\tau}$) were calibrated and considered for the viscous response of the hydrogels.

The friction force between the rubber-stopper and the inner wall of plunger increased when the injection velocity was increased as shown in Figure 6.6. Overall, the friction response is divided into two stages, static and dynamic. The dynamic stage seems very steady when the injection velocity was low. However, when the injection velocity was increased, the force data exhibited relatively volatile behavior. The two friction phases observed by the LVDT makes it difficult to estimate V_p, particularly, at high velocities, which may lead to fallible calculation of "λ" and inaccurate characterization of material properties. Therefore, observing the pressure from an independent source (pressurized water that flows into the system) will result in measurements that are more accurate. There is no published data, to author's knowledge, exists on testing the viscoelastic response of PVA hydrogels in multi-axial loading; however, the test proved to be capable of measuring the rate-dependent response of the hydrogels. Due to the technique's multi-axial nature and simplicity, it has the potential to provide enough information about in-vivo viscoelastic behavior of biological tissues in different loading axes, which will be addressed in a different study.

6.7. Conclusions

Measuring the rate-dependent response of rubber-like materials commonly performed using uniaxial loading. This investigation introduced an alternative that allows for multi-axial measurement to the viscoelastic properties of these materials. The following results can be concluded from this study:

- The hydrogel specimens were loaded up to 80% hoop strain, and the corresponding hoop stresses were 0.44 MPa, 0.7 MPa and 0.82 MPa at strain rates of 5 μl/s, 20 μl/s and 50 μl/s, respectively. At the same rates, the observed pressure magnitudes were 0.035 MPa, 0.044MPa and 0.052 MPa, respectively.
- Yeoh and Ogden models provided good fit to the experimental data, R^2 (0.97-0.99), while Arruda-Boyce model provided the least fit to the experimental data, R^2 (0.8-0.86). However, the three models provided similar initial shear moduli in all deformation rates.
- The agreement between the experimental, analytical and numerical data indicates that the cavity expansion test is capable of measuring the rate-dependent response of rubber-like materials.

- The relaxation coefficients of Prony series can be used with the material parameters of the three SEFs to perform linear viscoelastic analysis for PVA hydrogels subjected to multi-axial loading at different deformation rates using FE solvers such as Abaqus®.
- The cavity expansion technique proved to be capable of measuring the rate-dependent properties of rubber-like materials. Thus, it has the potential to measure the viscoelastic properties of biological tissues under multi-axial loading conditions, in addition to the hyperplastic properties, .

Chapter 7

Conclusions and Future Work

This thesis presented the application of a multiaxial loading protocol that harnesses the cavitation phenomenon to measure the mechanical properties of soft materials. The focus was on materials that are commonly characterized for different applications in the biomedical field, PVA hydrogels and Porcine liver tissues. This was performed on four stages presented as independent chapters (Ch3 – Ch6). In this chapter, results from these chapters are summarized, and future research directions are proposed.

7.1. Summary of results and contributions

Chapter 3 presented the measurement of PVA hydrogels' mechanical response to cavity deformations. In this study, three experiments were performed: cavity expansion test, compressibility test, and CT imaging. The objectives of this study are: (i) introducing a framework that allows for calibrating SEFs in the polar coordinate system, (ii) calculating the stresses generated due to cavity deformations in both of compressible and incompressible material assumptions, and (iii) verifying the geometric configuration of the cavity defamations. This study concluded the following:

- The analytical framework used for the calibration process is sufficient to calibrate the hyperelastic models. This is evident in the FE simulation results, which were able to reproduce the experimental data.
- The needle has a negligible effect on the material properties measured by the cavity test. This is mainly due to the insignificance of the stresses and strains generated during the needle insertion in comparison with their counterparts generated due to the cavity expansion.
- The needle-balloon tool is capable of limiting the cavity deformations to a spherical configuration, which agrees with the analytical hypothesis adopted for the calibration process. Although at low volume levels the deformations were not perfectly spherical, FE simulations of irregular cavities showed that the overall volume of the cavity is sufficient to calibrate the hyperelastic material models.

In chapter 4, the mechanical properties of porcine liver were measured. The measurement process was performed on two porcine livers few hours post-mortem. In addition, the liver tissues were tested without the need to perform any preparation procedures, such as cutting into specific shapes, that are usually needed in other conventional testing methodologies. In this study, new needle-balloon tool and new pressure sensor were used to obtain more accurate experimental data. The following conclusions are drawn from this study:

- The cavity expansion technique successfully predicted the initial shear moduli of porcine liver tissues (≈ 4 kPa). This magnitude agrees with the range of moduli reported in literature using different approaches (3 kPa – 5 kPa).
- The cavity expansion test generates hoop Cauchy stresses, particularly at the peak loading point, higher than the magnitudes reported in literature using uniaxial tension.
- The cavity expansion method is capable of obtaining robust experimental data due to logistically very short time needed to test the livers after excision. In addition, the technique is capable to measure the tissues mechanics, which is evident in the agreement between the experimental data, FE simulations, and the results from CT imaging.

Chapter 5 provided an explanation of the cavity expansion method by comparing it to a reference method, uniaxial tension. The 10% w/w PVA hydrogels were used as a representative of rubber-like materials in this study. The comparison addressed the tension stress levels, range of strains, and the initial shear moduli. The following conclusions are drawn:

- The data from both techniques show that the PVA hydrogels specimens failed at the same strain level ($\varepsilon = 75\%$). This magnitude agrees with the range of ultimate strains reported in literature for 10% w/w PVA hydrogels.
- Both techniques show similar tension stress levels up to 45 % strain. Afterward, the hoop stresses generated due to cavitation increased exponentially. In addition, the maximum stresses in the cavity expansion method are twice the stresses generated during the uniaxial tension.
- Both techniques predicted similar initial shear moduli (≈ 22 kPa).
- The observed pressure data was insignificant in comparison with the hoop stresses data. Although the cavity test is a multi-axial loading technique, the significance of the hoop stresses shows that the material failure is controlled by equi-biaxial tension.

Chapter 6 presented a study in which the viscoelastic response of soft materials was measured using the cavity expansion method. This type of behaviors is usually investigated using uniaxial and biaxial loading techniques. In this study, the cavity expansion method provided a new option that allows for multi-axial loading to measure the time-dependent response of soft materials such as PVA hydrogels. The study concluded the following:

- Using the linear viscoelastic framework is sufficient to describe the mechanical viscoelasticity of PVA hydrogels subjected to cavity loads.
- The implemented phenomenological and micromechanical models were successful in capturing the instantaneous nonlinear elastic response of the hydrogels at different deformation rates with R^2 larger than 0.97 and 0.8, respectively.
- The cavity expansion technique is capable of measuring the mechanical time-dependence of PVA hydrogels. This is evident in the agreement between the experimental data, analytical solution, and FE simulations.

7.2. Recommendations and future research directions

The analytical framework provided a mathematical tool that allowed the SEFs to capture the nonlinear elastic response of soft materials. In chapter 6, the same analytical tool was used to obtain material parameters for the linear viscoelastic solution. However, biological tissues tend to have nonlinear history-dependent viscoelastic properties. This behavior is commonly described using Fung's quasilinear viscoelastic theory. Alternatively, more complex nonlinear viscoelastic solutions can be used to describe the viscoelasticity of biological tissues. Both solutions can be used with the cavity expansion method. They can be used with the cavity expansion method as follows:

- The current calibration procedure is still sufficient to obtain the parameters necessary for the QLV solution, however, QLV is not available in most of FE solvers, and thus, a subroutine is needed in order to implement QLV solution numerically.
- For nonlinear viscoelastic solutions, most FE solvers provide a Parallel Rheological Framework (PRF) to simulate this behavior. The current analytical framework is not able to evaluate the parameters of PRF, thus a new analytical framework needs to be developed to calibrate the PRF parameters in polar coordinates to utilize the data obtained from the cavity expansion test.

This thesis provided different applications for the cavity expansion test. In these applications, the materials under investigation were considered isotropic. To enable the cavity expansion method to characterize the mechanical properties of transversely isotropic materials, a new framework needs to be developed. Analysis of cavitation growth in anisotropic rubber-like materials while being loaded axially was addressed in several studies (Antman & Negron-Marrero, 1987; C. O. Horgan & Pence, 1989; Polignone & Horgan, 1993), which can be used in the derivation of a new solution.

In chapters 4, 5, and 6, the definition of the deformation term (λ) was based on an initial volume of the incompressible fluid introduced into the balloon. This volume was calculated from the time data collected during the experiments. Although this volume commenced the cavitation process, it encountered no tangible resistance by the gels and liver tissues. It is hypothesized that the lack of resistance is because of the displacement of the channel wall created by the needle shaft along the balloon region, which relieves the restrictions imposed by the material structure. Further investigation is needed to verify this phenomenon. Using transparent gels and an optical microscope (e.g. Keyence Model VHX 5000) will provide a visual characterization to the initial stage of the cavity expansion.

References

A. Weiss, J., N. Maker, B., & Govindjee, S. (1996). Finite Element Implementation of Incompressible, Transversely Isotropic Hyperelasticity. *Computer Methods in Applied Mechanics and Engineering*, *135*, 107–128. https://doi.org/10.1016/0045-7825(96)01035-3

ABAQUS/CAE. (2013). *Abaqus/CAE v6.13 User's Manual.* ABAQUS Inc., Richmond, USA.

Afghan, N. (2016). *Mechanical Properties of Poly (vinyl alcohol) Based Blends and Composites* [Thesis]. Western University.

Agoras, M., Lopez-Pamies, O., & Ponte Castañeda, P. (2009). A general hyperelastic model for incompressible fiber-reinforced elastomers. *Journal of the Mechanics and Physics of Solids*, *57*(2), 268–286. https://doi.org/10.1016/j.jmps.2008.10.014

Ahsanizadeh, S., & Li, L. (2015). Visco-hyperelastic constitutive modeling of soft tissues based on short and long-term internal variables. *BioMedical Engineering OnLine*, *14*(1), 29. https://doi.org/10.1186/s12938-015-0023-7

Alexander, H. (1968). A constitutive relation for rubber-like materials. *International Journal of Engineering Science*, *6*(9), 549–563. https://doi.org/10.1016/0020-7225(68)90006-2

Al-Mayah, A, Moseley, J., & Brock, K. K. (2008). Contact surface and material nonlinearity modeling of human lungs. *Physics in Medicine and Biology*, *53*(1), 305–317. https://doi.org/10.1088/0031-9155/53/1/022

Al-Mayah, Adil. (2011). *Soft tissues mechanical characterization using internal deformation* [Technical discolusre report (WatCo)]. University of Waterloo.

Al-Mayah, Adil, Moseley, J., Hunter, S., & Brock, K. (2015). Radiation dose response simulation for biomechanical-based deformable image registration of head and neck cancer treatment. *Physics in Medicine and Biology*, *60*(21), 8481–8489. https://doi.org/10.1088/0031-9155/60/21/8481

Al-Mayah, Adil, Moseley, J., Velec, M., & Brock, K. (2011). Toward efficient biomechanical-based deformable image registration of lungs for image-guided radiotherapy. *Physics in Medicine and Biology*, *56*(15), 4701–4713. https://doi.org/10.1088/0031-9155/56/15/005

Al-Mayah, Adil, Moseley, J., Velec, M., & Brock, K. (2009). Deformable modeling of human liver with contact surface. *2009 IEEE Toronto International Conference Science and*

Technology for Humanity (TIC-STH), 137–140. https://doi.org/10.1109/TIC-STH.2009.5444517

Antman, S. S., & Negron-Marrero, P. V. (1987). The remarkable nature of radially symmetric equilibrium states of aeolotropic nonlinearly elastic bodies. *Journal of Elasticity*, *18*(2), 131–164. https://doi.org/10.1007/BF00127554

Arruda, E. M., & Boyce, M. C. (1993). A three-dimensional constitutive model for the large stretch behavior of rubber elastic materials. *Journal of the Mechanics and Physics of Solids*, *41*(2), 389–412. https://doi.org/10.1016/0022-5096(93)90013-6

Ashrafi, P., & Tönük, E. (2014). Indentation and Observation of Anisotropic Soft Tissues Using an Indenter Device. *Süleyman Demirel Üniversitesi Fen Bilimleri Enstitüsü Dergisi*, *18*(3). https://doi.org/10.19113/sdufbed.48294

Bergstrom, J. (2015). *Mechanics of solid polymers: Theory and computational modeling*. Elsevier.

Betsch, D. F., & Baer, E. (1980). Structure and mechanical properties of rat tail tendon1. *Biorheology*, *17*(1–2), 83–94. https://doi.org/10.3233/BIR-1980-171-211

Blake, A. (Ed.). (1985). *Handbook of mechanics, materials, and structures*. Wiley.

Brands, D. W., Bovendeerd, P. H., Peters, G. W., & Wismans, J. S. (2000). The large shear strain dynamic behaviour of in-vitro porcine brain tissue and a silicone gel model material. *Stapp Car Crash Journal*, *44*, 249–260.

Brostow, W., Pietkiewicz, D., & Wisner, S. R. (2007). Polymer tribology in safety medical devices: Retractable syringes. *Advances in Polymer Technology*, *26*(1), 56–64. https://doi.org/10.1002/adv.20084

Brunon, A., Bruyère-Garnier, K., & Coret, M. (2010). Mechanical characterization of liver capsule through uniaxial quasi-static tensile tests until failure. *Journal of Biomechanics*, *43*(11), 2221–2227. https://doi.org/10.1016/j.jbiomech.2010.03.038

Burnett, P. J., & Rickerby, D. S. (1987). The mechanical properties of wear-resistant coatings. *Thin Solid Films*, *148*(1), 41–50. https://doi.org/10.1016/0040-6090(87)90119-2

Buschmann, M. D., Soulhat, J., Shirazi-Adl, A., Jurvelin, J. S., & Hunziker, E. B. (1997). Confined compression of articular cartilage. *Journal of Biomechanics*, *31*(2), 171–178. https://doi.org/10.1016/S0021-9290(97)00124-3

Carter, F. J., Frank, T. G., Davies, P. J., McLean, D., & Cuschieri, A. (2001). Measurements and modelling of the compliance of human and porcine organs. *Medical Image Analysis*, *5*(4), 231–236. https://doi.org/10.1016/S1361-8415(01)00048-2

Casanova, F., Carney, P. R., & Sarntinoranont, M. (2014). Effect of Needle Insertion Speed on Tissue Injury, Stress, and Backflow Distribution for Convection-Enhanced Delivery in the Rat Brain. *PLoS ONE*, *9*(4), e94919. https://doi.org/10.1371/journal.pone.0094919

Cash, D. M., Miga, M. I., Glasgow, S. C., Dawant, B. M., Clements, L. W., Cao, Z., Galloway, R. L., & Chapman, W. C. (2007). Concepts and Preliminary Data Toward the Realization of Image-guided Liver Surgery. *Journal of Gastrointestinal Surgery*, *11*(7), 844–859. https://doi.org/10.1007/s11605-007-0090-6

Chabanas, M., Luboz, V., & Payan, Y. (2003). Patient specific finite element model of the face soft tissues for computer-assisted maxillofacial surgery. *Medical Image Analysis*, *7*(2), 131–151. https://doi.org/10.1016/S1361-8415(02)00108-1

Chan, E., Hubbard, A., Sane, S., & Maa, Y.-F. (2012). Syringe Siliconization Process Investigation and Optimization. *PDA Journal of Pharmaceutical Science and Technology*, *66*(2), 136–150. https://doi.org/10.5731/pdajpst.2012.00856

Chang, C. (Ed.). (2000). *Biopolymers, PVA hydrogels, anionic polymerisation, nanocomposites*. Springer.

Charlton, D. J., Yang, J., & Teh, K. K. (1994). A Review of Methods to Characterize Rubber Elastic Behavior for Use in Finite Element Analysis. *Rubber Chemistry and Technology*, *67*(3), 481–503. https://doi.org/10.5254/1.3538686

Chatelin, S., Oudry, J., Périchon, N., Sandrin, L., Allemann, P., Soler, L., & Willinger, R. (2011). In vivo liver tissue mechanical properties by transient elastography: Comparison with dynamic mechanical analysis. *Biorheology*, *48*(2), 75–88. https://doi.org/10.3233/BIR-2011-0584

Chen, F., Kang, D.-J., & Park, J.-H. (2013). New measurement method of Poisson's ratio of PVA hydrogels using an optical flow analysis for a digital imaging system. *Measurement Science and Technology*, *24*(5), 055602. https://doi.org/10.1088/0957-0233/24/5/055602

Chien, L.-C., Lo, S.-S., & Yeh, S.-Y. (2013). Incidence of liver trauma and relative risk factors for mortality: A population-based study. *Journal of the Chinese Medical Association*, *76*(10), 576–582. https://doi.org/10.1016/j.jcma.2013.06.004

Christensen, R. (2012). *Theory of Viscoelasticity: An Introduction*. Elsevier.

Christensen, R. (2014). *Theory of Viscoelasticity: An Introduction.* Elsevier Science. http://qut.eblib.com.au/patron/FullRecord.aspx?p=1152643

Corkhill, P. H., Hamilton, C. J., & Tighe, B. J. (1989). Synthetic hydrogels VI. Hydrogel composites as wound dressings and implant materials. *Biomaterials*, *10*(1), 3–10. https://doi.org/10.1016/0142-9612(89)90002-1

Dalrymple, T., Choi, J., & Kurt, M. (2007, October). *Elastomer Rate-Dependence: a Testing and Material Modelling Methodology*. Technical Meeting of the Rubber Division of the American Chemical Society.

De Bardi, M., Müller, R., Grünzweig, C., Mannes, D., Rigollet, M., Bamberg, F., Jung, T. A., & Yang, K. (2018). Clogging in staked-in needle pre-filled syringes (SIN-PFS): Influence of water vapor transmission through the needle shield. *European Journal of Pharmaceutics and Biopharmaceutics*, *127*, 104–111. https://doi.org/10.1016/j.ejpb.2018.02.016

deBotton, G., Bustamante, R., & Dorfmann, A. (2013). Axisymmetric bifurcations of thick spherical shells under inflation and compression. *International Journal of Solids and Structures*, *50*(2), 403–413. https://doi.org/10.1016/j.ijsolstr.2012.10.004

DeCarlo, P. F., Slowik, J. G., Worsnop, D. R., Davidovits, P., & Jimenez, J. L. (2004). Particle Morphology and Density Characterization by Combined Mobility and Aerodynamic Diameter Measurements. Part 1: Theory. *Aerosol Science and Technology*, *38*(12), 1185–1205. https://doi.org/10.1080/027868290903907

Deffieux, T., Gennisson, J.-L., Bousquet, L., Corouge, M., Cosconea, S., Amroun, D., Tripon, S., Terris, B., Mallet, V., Sogni, P., Tanter, M., & Pol, S. (2015). Investigating liver stiffness and viscosity for fibrosis, steatosis and activity staging using shear wave elastography. *Journal of Hepatology*, *62*(2), 317–324. https://doi.org/10.1016/j.jhep.2014.09.020

Deng, Y.-C., Kong, W., & Ho, H. (1999). Development of a Finite Element Human Thorax Model for Impact Injury Studies. *SAE Transactions*, *108*, 1193–1199. JSTOR.

Destrade, M., Gilchrist, M. D., Murphy, J. G., Rashid, B., & Saccomandi, G. (2015). Extreme softness of brain matter in simple shear. *International Journal of Non-Linear Mechanics*, *75*, 54–58. https://doi.org/10.1016/j.ijnonlinmec.2015.02.014

Doerner, M. F., & Nix, W. D. (1986). A method for interpreting the data from depth-sensing indentation instruments. *Journal of Materials Research*, *1*(04), 601–609. https://doi.org/10.1557/JMR.1986.0601

Dong, Y., Ke, Y., Zheng, Z., Yang, H., & Yao, X. (2017). Effect of stress relaxation on sealing performance of the fabric rubber seal. *Composites Science and Technology*, *151*, 291–301. https://doi.org/10.1016/j.compscitech.2017.08.025

Drury, J. L., & Mooney, D. J. (2003). Hydrogels for tissue engineering: Scaffold design variables and applications. *Biomaterials*, *24*(24), 4337–4351. https://doi.org/10.1016/S0142-9612(03)00340-5

du Plessis, A., Broeckhoven, C., Guelpa, A., & le Roux, S. G. (2017). Laboratory x-ray micro-computed tomography: A user guideline for biological samples. *GigaScience*, *6*(6). https://doi.org/10.1093/gigascience/gix027

Duliu, O. (1999). Computer axial tomography in geosciences: An overview. *Earth-Science Reviews*, *48*(4), 265–281. https://doi.org/10.1016/S0012-8252(99)00056-2

Dương, M. T., Nguyễn, N. H., Trần, T. N., Tolba, R. H., & Staat, M. (2015). Influence of refrigerated storage on tensile mechanical properties of porcine liver and spleen. *International Biomechanics*, *2*(1), 79–88. https://doi.org/10.1080/23335432.2015.1049295

Elshazly, T. (2004). *Characterization of PVA hydrogels with Regards to Vascular Graft Development*. Georgeia Institute of Technology.

Eom, J., Shi, C., Xu, X. G., & De, S. (2009a). Modeling Respiratory Motion for Cancer Radiation Therapy Based on Patient-Specific 4DCT Data. In *Medical Image Computing and Computer-Assisted Intervention – MICCAI 2009* (Vol. 5762, pp. 348–355). Springer Berlin Heidelberg. https://doi.org/10.1007/978-3-642-04271-3_43

Eom, J., Shi, C., Xu, X. G., & De, S. (2009b). Modeling respiratory motion for cancer radiation therapy based on patient-specific 4DCT data. *Medical Image Computing and Computer-Assisted Intervention: MICCAI ... International Conference on Medical Image Computing and Computer-Assisted Intervention*, *12*(Pt 2), 348–355.

Farges, G., & Degout, D. (1989). Interpretation of the indentation size effect in vickers microhardness measurements-absolute hardness of materials. *Thin Solid Films*, *181*(1–2), 365–374. https://doi.org/10.1016/0040-6090(89)90505-1

Faye, A., Rodríguez-Martínez, J. A., & Volokh, K. Y. (2017). Spherical void expansion in rubber-like materials: The stabilizing effects of viscosity and inertia. *International Journal of Non-Linear Mechanics*, *92*, 118–126. https://doi.org/10.1016/j.ijnonlinmec.2017.04.005

Fehervary, H., Smoljkić, M., Vander Sloten, J., & Famaey, N. (2016). Planar biaxial testing of soft biological tissue using rakes: A critical analysis of protocol and fitting process. *Journal of the Mechanical Behavior of Biomedical Materials*, *61*, 135–151. https://doi.org/10.1016/j.jmbbm.2016.01.011

Feldkamp, L. A., Davis, L. C., & Kress, J. W. (1984). Practical cone-beam algorithm. *JOSA A*, *1*(6), 612–619. https://doi.org/10.1364/JOSAA.1.000612

Feliciano, D. V. (1989). Surgery for Liver Trauma. *Surgical Clinics of North America*, *69*(2), 273–284. https://doi.org/10.1016/S0039-6109(16)44785-7

Findley, W. N., Lai, J. S., & Onaran, K. (1976). *Creep and relaxation of nonlinear viscoelastic materials, with an introduction to linear viscoelasticity*. North-Holland Pub. Co. : Sole distributors for the U.S.A. and Canada, Elsevier/North Holland. http://www.123library.org/book_details/?id=100782

Flory, Paul. J., & Volkenstein, M. (1969). Statistical mechanics of chain molecules. *Biopolymers*, *8*(5), 699–700. https://doi.org/10.1002/bip.1969.360080514

Fond, C. (2001). Cavitation criterion for rubber materials: A review of void-growth models. *Journal of Polymer Science Part B: Polymer Physics*, *39*(17), 2081–2096. https://doi.org/10.1002/polb.1183

Franchi-Abella, S., Elie, C., & Correas, J.-M. (2013). Ultrasound elastography: Advantages, limitations and artefacts of the different techniques from a study on a phantom. *Diagnostic and Interventional Imaging*, *94*(5), 497–501. https://doi.org/10.1016/j.diii.2013.01.024

Fung, Y.-C. (1993). *Biomechanics Mechanical Properties of Living Tissues*. Springer New York. http://dx.doi.org/10.1007/978-1-4757-2257-4

Gao, Z., Lister, K., & Desai, J. P. (2010a). Constitutive Modeling of Liver Tissue: Experiment and Theory. *Annals of Biomedical Engineering*, *38*(2), 505–516. https://doi.org/10.1007/s10439-009-9812-0

Gao, Z., Lister, K., & Desai, J. P. (2010b). Constitutive Modeling of Liver Tissue: Experiment and Theory. *Annals of Biomedical Engineering*, *38*(2), 505–516. https://doi.org/10.1007/s10439-009-9812-0

Gent, A. N., & Lindley. (1959). Internal rupture of bonded rubber cylinders in tension. *Proceedings of the Royal Society of London. Series A. Mathematical and Physical Sciences*, *249*(1257), 195–205. https://doi.org/10.1098/rspa.1959.0016

Giannakopoulos, A. E., & Triantafyllou, A. (2007). Spherical indentation of incompressible rubber-like materials. *Journal of the Mechanics and Physics of Solids*, *55*(6), 1196–1211. https://doi.org/10.1016/j.jmps.2006.11.010

Gilchrist, M. D., Murphy, J. G., Parnell, W., & Pierrat, B. (2014). Modelling the slight compressibility of anisotropic soft tissue. *International Journal of Solids and Structures*, *51*(23–24), 3857–3865. https://doi.org/10.1016/j.ijsolstr.2014.06.018

Glozman, T., & Azhari, H. (2010). A Method for Characterization of Tissue Elastic Properties Combining Ultrasonic Computed Tomography With Elastography. *Journal of Ultrasound in Medicine*, *29*(3), 387–398. https://doi.org/10.7863/jum.2010.29.3.387

Gu, W. Y., Yao, H., Huang, C. Y., & Cheung, H. S. (2003). New insight into deformation-dependent hydraulic permeability of gels and cartilage, and dynamic behavior of agarose gels in confined compression. *Journal of Biomechanics*, *36*(4), 593–598.

Hackett, R. M. (2016). *Hyperelasticity Primer*. Springer International Publishing. https://doi.org/10.1007/978-3-319-23273-7

Hassan, C. M., & Peppas, N. A. (2000). Structure and Morphology of Freeze/Thawed PVA Hydrogels. *Macromolecules*, *33*(7), 2472–2479. https://doi.org/10.1021/ma9907587

Hatakeyema, T., Uno, J., Yamada, C., Kishi, A., & Hatakeyama, H. (2005). Gel–sol transition of poly(vinyl alcohol) hydrogels formed by freezing and thawing. *Thermochimica Acta*, *431*(1–2), 144–148. https://doi.org/10.1016/j.tca.2005.01.062

Haug, E. (1997). Biomechanical Models in Vehicle Accident Simulation. In J. A. C. Ambrósio, M. F. O. S. Pereira, & F. P. Silva (Eds.), *Crashworthiness of Transportation Systems: Structural Impact and Occupant Protection* (pp. 237–259). Springer Netherlands. https://doi.org/10.1007/978-94-011-5796-4_11

Hernández, R., Sarafian, A., López, D., & Mijangos, C. (2004). Viscoelastic properties of poly(vinyl alcohol) hydrogels and ferrogels obtained through freezing–thawing cycles. *Polymer*, *45*(16), 5543–5549. https://doi.org/10.1016/j.polymer.2004.05.061

Herzog, W., & Gal, J. (1999). Tendon. In *Biomechanics of musculo-skeletal system* (2nd ed., pp. 127–147). John Wiley.

Holbrook, T. L., Hoyt, D. B., Eastman, A. B., Sise, M. J., Kennedy, F., Velky, T., Conroy, C., Pacyna, S., & Erwin, S. (2007). The Impact of Safety Belt Use on Liver Injuries in Motor Vehicle Crashes: The Importance of Motor Vehicle Safety Systems: *The Journal of Trauma: Injury, Infection, and Critical Care*, *63*(2), 300–306. https://doi.org/10.1097/TA.0b013e318074de05

Hollenstein, M., Nava, A., Valtorta, D., Snedeker, J. G., & Mazza, E. (2006). Mechanical Characterization of the Liver Capsule and Parenchyma. In M. Harders & G. Székely (Eds.), *Biomedical Simulation* (pp. 150–158). Springer Berlin Heidelberg. https://doi.org/10.1007/11790273_17

Holzapfel, G. A. (2000). *Nonlinear solid mechanics: A continuum approach for engineering*. Wiley.

Horgan, C. O., & Pence, T. J. (1989). Void nucleation in tensile dead-loading of a composite incompressible nonlinearly elastic sphere. *Journal of Elasticity*, *21*(1), 61–82. https://doi.org/10.1007/BF00040934

Horgan, Cornelius O., & Murphy, J. G. (2009). Compression tests and constitutive models for the slight compressibility of elastic rubber-like materials. *International Journal of Engineering Science*, *47*(11–12), 1232–1239. https://doi.org/10.1016/j.ijengsci.2008.10.009

Hu, X., Hao, L., Wang, H., Yang, X., Zhang, G., Wang, G., & Zhang, X. (2011). Hydrogel Contact Lens for Extended Delivery of Ophthalmic Drugs. *International Journal of Polymer Science*, *2011*, 1–9. https://doi.org/10.1155/2011/814163

Jacobs, N. T., Cortes, D. H., Vresilovic, E. J., & Elliott, D. M. (2013a). Biaxial Tension of Fibrous Tissue: Using Finite Element Methods to Address Experimental Challenges Arising From Boundary Conditions and Anisotropy. *Journal of Biomechanical Engineering*, *135*(2), 021004. https://doi.org/10.1115/1.4023503

Jacobs, N. T., Cortes, D. H., Vresilovic, E. J., & Elliott, D. M. (2013b). Biaxial Tension of Fibrous Tissue: Using Finite Element Methods to Address Experimental Challenges Arising From Boundary Conditions and Anisotropy. *Journal of Biomechanical Engineering*, *135*(2), 021004. https://doi.org/10.1115/1.4023503

Joshi, A., Fussell, G., Thomas, J., Hsuan, A., Lowman, A., Karduna, A., Vresilovic, E., & Marcolongo, M. (2006a). Functional compressive mechanics of a PVA/PVP nucleus

pulposus replacement. *Biomaterials*, *27*(2), 176–184. https://doi.org/10.1016/j.biomaterials.2005.06.003

Joshi, A., Fussell, G., Thomas, J., Hsuan, A., Lowman, A., Karduna, A., Vresilovic, E., & Marcolongo, M. (2006b). Functional compressive mechanics of a PVA/PVP nucleus pulposus replacement. *Biomaterials*, *27*(2), 176–184. https://doi.org/10.1016/j.biomaterials.2005.06.003

Kaliske, M., & Rothert, H. (1997). On the finite element implementation of rubber-like materials at finite strains. *Engineering Computations*, *14*(2), 216–232. https://doi.org/10.1108/02644409710166190

Kang, T. (2008). Mechanical behavior of arteries under inflation and extension. *Journal of Mechanical Science and Technology*, *22*(4), 621–627. https://doi.org/10.1007/s12206-008-0213-3

Karimi, A., Navidbakhsh, M., & Beigzadeh, B. (2014). A visco-hyperelastic constitutive approach for modeling polyvinyl alcohol sponge. *Tissue and Cell*, *46*(1), 97–102. https://doi.org/10.1016/j.tice.2013.12.004

Kasem, H., Shriki, H., Ganon, L., Mizrahi, M., Abd-Rbo, K., & Domb, A. J. (2019). Rubber plunger surface texturing for friction reduction in medical syringes. *Friction*, *7*(4), 351–358. https://doi.org/10.1007/s40544-018-0227-5

Kawabata, S., Yamashita, Y., Ooyama, H., & Yoshida, S. (1995). Mechanism of Carbon-Black Reinforcement of Rubber Vulcanizate. *Rubber Chemistry and Technology*, *68*(2), 311–329. https://doi.org/10.5254/1.3538745

Kemper, A. R., Santago, A. C., Stitzel, J. D., Sparks, J. L., & Duma, S. M. (2010). Biomechanical response of human liver in tensile loading. *Annals of Advances in Automotive Medicine. Association for the Advancement of Automotive Medicine. Annual Scientific Conference*, *54*, 15–26.

Kendall, M. J., & Siviour, C. R. (2015). Experimentally Simulating High Rate Composite Deformation in Tension and Compression: Polymer Bonded Explosive Simulant. *Journal of Dynamic Behavior of Materials*, *1*(2), 114–123. https://doi.org/10.1007/s40870-015-0018-2

Kennedy, P., Wagner, M., Castéra, L., Hong, C. W., Johnson, C. L., Sirlin, C. B., & Taouli, B. (2018). Quantitative Elastography Methods in Liver Disease: Current Evidence and Future Directions. *Radiology*, *286*(3), 738–763. https://doi.org/10.1148/radiol.2018170601

Kim, K., Kim, C. H., Kim, H.-Y., & Kim, D.-S. (2010). Effects of Blanket Roller Deformation on Printing Qualities in Gravure-Offset Printing Method. *Japanese Journal of Applied Physics*, *49*(5), 05EC04. https://doi.org/10.1143/JJAP.49.05EC04

Kiss, M. Z., Daniels, M. J., & Varghese, T. (2009). Investigation of temperature-dependent viscoelastic properties of thermal lesions in ex vivo animal liver tissue. *Journal of Biomechanics*, *42*(8), 959–966. https://doi.org/10.1016/j.jbiomech.2009.03.002

Kobayashi, M., & Hyu, H. S. (2010). Development and Evaluation of Polyvinyl Alcohol-Hydrogels as an Artificial Atrticular Cartilage for Orthopedic Implants. *Materials*, *3*(4), 2753–2771. https://doi.org/10.3390/ma3042753

Kokabi, M., Sirousazar, M., & Hassan, Z. M. (2007). PVA–clay nanocomposite hydrogels for wound dressing. *European Polymer Journal*, *43*(3), 773–781. https://doi.org/10.1016/j.eurpolymj.2006.11.030

Krouskop, T. A., Wheeler, T. M., Kallel, F., Garra, B. S., & Hall, T. (1998). Elastic Moduli of Breast and Prostate Tissues under Compression. *Ultrasonic Imaging*, *20*(4), 260–274. https://doi.org/10.1177/016173469802000403

Kundu, S., & Crosby, A. J. (2009). Cavitation and fracture behavior of polyacrylamide hydrogels. *Soft Matter*, *5*(20), 3963. https://doi.org/10.1039/b909237d

Last, J. A., Pan, T., Ding, Y., Reilly, C. M., Keller, K., Acott, T. S., Fautsch, M. P., Murphy, C. J., & Russell, P. (2011). Elastic Modulus Determination of Normal and Glaucomatous Human Trabecular Meshwork. *Investigative Opthalmology & Visual Science*, *52*(5), 2147. https://doi.org/10.1167/iovs.10-6342

Lee, C.-T., Kung, P.-H., & Lee, Y.-D. (2005). Preparation of poly(vinyl alcohol)-chondroitin sulfate hydrogel as matrices in tissue engineering. *Carbohydrate Polymers*, *61*(3), 348–354. https://doi.org/10.1016/j.carbpol.2005.06.018

Lee, J.-H., Lee, S.-S., Chang, J.-D., Thompson, M. S., Kang, D.-J., Park, S., & Park, S. (2013). A Novel Method for the Accurate Evaluation of Poisson's Ratio of Soft Polymer Materials. *The Scientific World Journal*, *2013*, 1–7. https://doi.org/10.1155/2013/930798

Lee, S.-Y., Pereira, B. P., Yusof, N., Selvaratnam, L., Yu, Z., Abbas, A. A., & Kamarul, T. (2009). Unconfined compression properties of a porous poly(vinyl alcohol)–chitosan-based hydrogel after hydration. *Acta Biomaterialia*, *5*(6), 1919–1925. https://doi.org/10.1016/j.actbio.2009.02.014

Leibinger, A., Forte, A. E., Tan, Z., Oldfield, M. J., Beyrau, F., Dini, D., & Rodriguez y Baena, F. (2016). Soft Tissue Phantoms for Realistic Needle Insertion: A Comparative Study. *Annals of Biomedical Engineering*, *44*(8), 2442–2452. https://doi.org/10.1007/s10439-015-1523-0

Lemaître, J. (Ed.). (2001). *Handbook of materials behavior models*. Academic Press.

Leng, D., Xu, K., Qin, L., Ma, Y., & Liu, G. (2019). A Hyper-Elastic Creep Approach and Characterization Analysis for Rubber Vibration Systems. *Polymers*, *11*(6), 988. https://doi.org/10.3390/polym11060988

Lev, Y., & Volokh, K. Y. (2016). On Cavitation in Rubberlike Materials. *Journal of Applied Mechanics*, *83*(4), 044501. https://doi.org/10.1115/1.4032377

Li, J., Mayau, D., & Song, F. (2007). A constitutive model for cavitation and cavity growth in rubber-like materials under arbitrary tri-axial loading. *International Journal of Solids and Structures*, *44*(18–19), 6080–6100. https://doi.org/10.1016/j.ijsolstr.2007.02.016

Li, L., Maccabi, A., Abiri, A., Juo, Y.-Y., Zhang, W., Chang, Y.-J., Saddik, G. N., Jin, L., Grundfest, W. S., Dutson, E. P., Eldredge, J. D., Benharash, P., & Candler, R. N. (2019). Characterization of perfused and sectioned liver tissue in a full indentation cycle using a visco-hyperelastic model. *Journal of the Mechanical Behavior of Biomedical Materials*, *90*, 591–603. https://doi.org/10.1016/j.jmbbm.2018.11.006

Li, W., Wang, D., Yang, W., & Song, Y. (2016). Compressive mechanical properties and microstructure of PVA–HA hydrogels for cartilage repair. *RSC Adv.*, *6*(24), 20166–20172. https://doi.org/10.1039/C6RA02166B

Li, X., Shu, M., Li, H., Gao, X., Long, S., Hu, T., & Wu, C. (2018). Strong, tough and mechanically self-recoverable poly(vinyl alcohol)/alginate dual-physical double-network hydrogels with large cross-link density contrast. *RSC Advances*, *8*(30), 16674–16689. https://doi.org/10.1039/C8RA01302K

Lim, Y.-J., Deo, D., Singh, T. P., Jones, D. B., & De, S. (2009). In situ measurement and modeling of biomechanical response of human cadaveric soft tissues for physics-based surgical

simulation. *Surgical Endoscopy*, *23*(6), 1298–1307. https://doi.org/10.1007/s00464-008-0154-z

Lin, C.-C., & Anseth, K. S. (2009). PEG Hydrogels for the Controlled Release of Biomolecules in Regenerative Medicine. *Pharmaceutical Research*, *26*(3), 631–643. https://doi.org/10.1007/s11095-008-9801-2

Lin, D. C., Shreiber, D. I., Dimitriadis, E. K., & Horkay, F. (2009). Spherical indentation of soft matter beyond the Hertzian regime: Numerical and experimental validation of hyperelastic models. *Biomechanics and Modeling in Mechanobiology*, *8*(5), 345–358. https://doi.org/10.1007/s10237-008-0139-9

Ling, Y., Li, C., Feng, K., Duncan, R., Eisma, R., Huang, Z., & Nabi, G. (2016). Effects of fixation and preservation on tissue elastic properties measured by quantitative optical coherence elastography (OCE). *Journal of Biomechanics*, *49*(7), 1009–1015. https://doi.org/10.1016/j.jbiomech.2016.02.013

Liu, L., Zhao, C., & Yang, F. (2012). TiO2 and polyvinyl alcohol (PVA) coated polyester filter in bioreactor for wastewater treatment. *Water Research*, *46*(6), 1969–1978. https://doi.org/10.1016/j.watres.2012.01.017

Lozinsky, V. I., Plieva, F. M., Galaev, I. Yu., & Mattiasson, B. (2001). The potential of polymeric cryogels in bioseparation. *Bioseparation*, *10*(4/5), 163–188. https://doi.org/10.1023/A:1016386902611

Lu, Y. C., & Shinozaki, D. M. (2010). Temperature Dependent Viscoelastic Properties of Polymers Investigated by Small-Scale Dynamic Mechanical Analysis. *Experimental Mechanics*, *50*(1), 71–77. https://doi.org/10.1007/s11340-008-9215-4

Lu, Y.-C., & Untaroiu, C. D. (2012a). Freezing and decay effects on material properties of porcine kidney and liver. *Biomedical Sciences Instrumentation*, *48*, 275–281.

Lu, Y.-C., & Untaroiu, C. D. (2012b). Freezing and decay effects on material properties of porcine kidney and liver. *Biomedical Sciences Instrumentation*, *48*, 275–281.

Luboz, V., Chabanas, M., Swider, P., & Payan, Y. (2005). Orbital and maxillofacial computer aided surgery: Patient-specific finite element models to predict surgical outcomes. *Computer Methods in Biomechanics and Biomedical Engineering*, *8*(4), 259–265. https://doi.org/10.1080/10255840500289921

Ma, R., Xiong, D., Miao, F., Zhang, J., & Peng, Y. (2009). Novel PVP/PVA hydrogels for articular cartilage replacement. *Materials Science and Engineering: C*, *29*(6), 1979–1983. https://doi.org/10.1016/j.msec.2009.03.010

Maiolo, A. S., Amado, M. N., Gonzalez, J. S., & Alvarez, V. A. (2012). Development and characterization of Poly (vinyl alcohol) based hydrogels for potential use as an articular cartilage replacement. *Materials Science and Engineering: C*, *32*(6), 1490–1495. https://doi.org/10.1016/j.msec.2012.04.030

Mansouri, M. R., & Darijani, H. (2014). Constitutive modeling of isotropic hyperelastic materials in an exponential framework using a self-contained approach. *International Journal of Solids and Structures*, *51*(25–26), 4316–4326. https://doi.org/10.1016/j.ijsolstr.2014.08.018

Matthews, G. L., Keegan, K. G., & Graham, H. L. (1996). Effects of tendon grip technique (frozen versus unfrozen) on in vitro surface strain measurements of the equine deep digital flexor tendon. *American Journal of Veterinary Research*, *57*(1), 111–115.

Menčík, J., & Swain, M. V. (1995). Errors associated with depth-sensing microindentation tests. *Journal of Materials Research*, *10*(06), 1491–1501. https://doi.org/10.1557/JMR.1995.1491

Miller, K., & Chinzei, K. (1997). Constitutive modelling of brain tissue: Experiment and theory. *Journal of Biomechanics*, *30*(11–12), 1115–1121. https://doi.org/10.1016/S0021-9290(97)00092-4

Millon, L. E., Mohammadi, H., & Wan, W. K. (2006). Anisotropic polyvinyl alcohol hydrogel for cardiovascular applications. *Journal of Biomedical Materials Research. Part B, Applied Biomaterials*, *79*(2), 305–311. https://doi.org/10.1002/jbm.b.30543

Mills, N. J. (2007). *Polymer foams handbook: Engineering and biomechanics applications and design guide* (1st ed). Butterworth Heinemann.

Mitchell, M. R., Link, R. E., Brieu, M., Diani, J., & Bhatnagar, N. (2007). A New Biaxial Tension Test Fixture for Uniaxial Testing Machine—A Validation for Hyperelastic Behavior of Rubber-like Materials. *Journal of Testing and Evaluation*, *35*(4), 100688. https://doi.org/10.1520/JTE100688

Mohan, Ch., Ramanathan, J., Kumar, S., & Gupta, A. (2011). Characterisation of Materials used in Flex Bearings of Large Solid Rocket Motors. *Defence Science Journal*, *61*(3), 264–269. https://doi.org/10.14429/dsj.61.52

Morriss, L., Wittek, A., & Miller, K. (2008). Compression testing of very soft biological tissues using semi-confined configuration—A word of caution. *Journal of Biomechanics*, *41*(1), 235–238. https://doi.org/10.1016/j.jbiomech.2007.06.025

Nafo, W., & Al-Mayah, A. (2019). Measuring Hyperelastic Properties of Hydrogels Using Cavity Expansion Method. *Experimental Mechanics*. https://doi.org/10.1007/s11340-019-00504-4

Nafo, Wanis. (2016). *Experimental and Analytical Investigation of the Cavity Expansion Method for Mechanical Characterization of Soft Materials*. https://uwspace.uwaterloo.ca/handle/10012/10327

Nafo, Wanis, & Al Mayah, A. (2018). Mechanical Investigations of Biological Tissues Using Tensile Loading and Indentation. In A. Al Mayah, *Biomechanics of Soft Tissues* (1st ed., pp. 27–54). CRC Press. https://doi.org/10.1201/9781351135825-2

Ng, B. H., Chou, S. M., & Krishna, V. (2005). The influence of gripping techniques on the tensile properties of tendons. *Proceedings of the Institution of Mechanical Engineers. Part H, Journal of Engineering in Medicine*, *219*(5), 349–354. https://doi.org/10.1243/095441105X34239

Nguyễn, N. H., Dương, M. T., Trần, T. N., Phạm, P. T., Grottke, O., Tolba, R., & Staat, M. (2012). Influence of a freeze–thaw cycle on the stress–stretch curves of tissues of porcine abdominal organs. *Journal of Biomechanics*, *45*(14), 2382–2386. https://doi.org/10.1016/j.jbiomech.2012.07.008

Ní Annaidh, A., Destrade, M., Gilchrist, M. D., & Murphy, J. G. (2013). Deficiencies in numerical models of anisotropic nonlinearly elastic materials. *Biomechanics and Modeling in Mechanobiology*, *12*(4), 781–791. https://doi.org/10.1007/s10237-012-0442-3

Nicolle, S., & Palierne, J.-F. (2010). Dehydration effect on the mechanical behaviour of biological soft tissues: Observations on kidney tissues. *Journal of the Mechanical Behavior of Biomedical Materials*, *3*(8), 630–635. https://doi.org/10.1016/j.jmbbm.2010.07.010

Nix, W. D. (1989). Mechanical properties of thin films. *Metallurgical Transactions A*, *20*(11), 2217. https://doi.org/10.1007/BF02666659

Ogden, R. W. (1972). Large Deformation Isotropic Elasticity—On the Correlation of Theory and Experiment for Incompressible Rubberlike Solids. *Proceedings of the Royal Society A: Mathematical, Physical and Engineering Sciences*, *326*(1567), 565–584. https://doi.org/10.1098/rspa.1972.0026

Ogden, R. W. (1997). *Non-linear elastic deformations*. Dover Publications.

Ogden, R. W., Saccomandi, G., & Sgura, I. (2004). Fitting hyperelastic models to experimental data. *Computational Mechanics*, *34*(6), 484–502. https://doi.org/10.1007/s00466-004-0593-y

Ottenbrite, R. M., Park, K., & Okano, T. (Eds.). (2010). *Biomedical Applications of Hydrogels Handbook*. Springer-Verlag. https://doi.org/10.1007/978-1-4419-5919-5

Oyen, M. L. (2014). Mechanical characterisation of hydrogel materials. *International Materials Reviews*, *59*(1), 44–59. https://doi.org/10.1179/1743280413Y.0000000022

Oyen, Michelle L. (Ed.). (2011). *Handbook of nanoindentation with biological applications*. Pan Stanford Publ.

Pan, Y., & Xiong, D. (2009). Study on compressive mechanical properties of nanohydroxyapatite reinforced poly(vinyl alcohol) gel composites as biomaterial. *Journal of Materials Science: Materials in Medicine*, *20*(6), 1291–1297. https://doi.org/10.1007/s10856-008-3679-8

Pan, Y.-S., Xiong, D.-S., & Ma, R.-Y. (2007). A study on the friction properties of poly(vinyl alcohol) hydrogel as articular cartilage against titanium alloy. *Wear*, *262*(7–8), 1021–1025. https://doi.org/10.1016/j.wear.2006.10.005

Park, H., & Park, K. (1996). Hydrogels in Bioapplications. In R. M. Ottenbrite, S. J. Huang, & K. Park (Eds.), *Hydrogels and Biodegradable Polymers for Bioapplications* (Vol. 627, pp. 2–10). American Chemical Society. https://doi.org/10.1021/bk-1996-0627.ch001

Paszek, M. J., Zahir, N., Johnson, K. R., Lakins, J. N., Rozenberg, G. I., Gefen, A., Reinhart-King, C. A., Margulies, S. S., Dembo, M., Boettiger, D., Hammer, D. A., & Weaver, V. M. (2005). Tensional homeostasis and the malignant phenotype. *Cancer Cell*, *8*(3), 241–254. https://doi.org/10.1016/j.ccr.2005.08.010

Peppas, N. A. (1975). Turbidimetric studies of aqueous poly(vinyl alcohol) solutions. *Die Makromolekulare Chemie*, *176*(11), 3433–3440. https://doi.org/10.1002/macp.1975.021761125

Polignone, D. A., & Horgan, C. O. (1993). Cavitation for incompressible anisotropic nonlinearly elastic spheres. *Journal of Elasticity*, *33*(1), 27–65. https://doi.org/10.1007/BF00042634

Poulain, X., Lefèvre, V., Lopez-Pamies, O., & Ravi-Chandar, K. (2017). Damage in elastomers: Nucleation and growth of cavities, micro-cracks, and macro-cracks. *International Journal of Fracture*, *205*(1), 1–21. https://doi.org/10.1007/s10704-016-0176-9

Rashid, B., Destrade, M., & Gilchrist, M. D. (2014a). Mechanical characterization of brain tissue in tension at dynamic strain rates. *Journal of the Mechanical Behavior of Biomedical Materials*, *33*, 43–54. https://doi.org/10.1016/j.jmbbm.2012.07.015

Rashid, B., Destrade, M., & Gilchrist, M. D. (2014b). Mechanical characterization of brain tissue in tension at dynamic strain rates. *Journal of the Mechanical Behavior of Biomedical Materials*, *33*, 43–54. https://doi.org/10.1016/j.jmbbm.2012.07.015

Ricciardi, R., Auriemma, F., Gaillet, C., De Rosa, C., & Lauprêtre, F. (2004). Investigation of the Crystallinity of Freeze/Thaw Poly(vinyl alcohol) Hydrogels by Different Techniques. *Macromolecules*, *37*(25), 9510–9516. https://doi.org/10.1021/ma048418v

Riemersa, D. J., & Schamhardt, H. C. (1982). The cryo-jaw, a clamp designed for in vitro rheology studies of horse digital flexor tendons. *Journal of Biomechanics*, *15*(8), 619–620.

Roberts, J. J., Earnshaw, A., Ferguson, V. L., & Bryant, S. J. (2011). Comparative study of the viscoelastic mechanical behavior of agarose and poly(ethylene glycol) hydrogels. *Journal of Biomedical Materials Research Part B: Applied Biomaterials*, *99B*(1), 158–169. https://doi.org/10.1002/jbm.b.31883

Safshekan, F., Tafazzoli-Shadpour, M., Abdouss, M., & Shadmehr, M. (2016). Mechanical Characterization and Constitutive Modeling of Human Trachea: Age and Gender Dependency. *Materials*, *9*(6), 456. https://doi.org/10.3390/ma9060456

Salameh, N., Larrat, B., Abarca-Quinones, J., Pallu, S., Dorvillius, M., Leclercq, I., Fink, M., Sinkus, R., & Van Beers, B. E. (2009). Early Detection of Steatohepatitis in Fatty Rat Liver by Using MR Elastography. *Radiology*, *253*(1), 90–97. https://doi.org/10.1148/radiol.2523081817

Samani, A., & Plewes, D. (2007). An inverse problem solution for measuring the elastic modulus of intact *ex vivo* breast tissue tumours. *Physics in Medicine and Biology*, *52*(5), 1247–1260. https://doi.org/10.1088/0031-9155/52/5/003

Samur, E., Sedef, M., Basdogan, C., Avtan, L., & Duzgun, O. (2007). A robotic indenter for minimally invasive measurement and characterization of soft tissue response. *Medical Image Analysis*, *11*(4), 361–373. https://doi.org/10.1016/j.media.2007.04.001

Sasso, M., Palmieri, G., Chiappini, G., & Amodio, D. (2008a). Characterization of hyperelastic rubber-like materials by biaxial and uniaxial stretching tests based on optical methods. *Polymer Testing*, *27*(8), 995–1004. https://doi.org/10.1016/j.polymertesting.2008.09.001

Sasso, M., Palmieri, G., Chiappini, G., & Amodio, D. (2008b). Characterization of hyperelastic rubber-like materials by biaxial and uniaxial stretching tests based on optical methods. *Polymer Testing*, *27*(8), 995–1004. https://doi.org/10.1016/j.polymertesting.2008.09.001

Shahzad, M., Kamran, A., Siddiqui, M. Z., & Farhan, M. (2015). Mechanical Characterization and FE Modelling of a Hyperelastic Material. *Materials Research*, *18*(5), 918–924. https://doi.org/10.1590/1516-1439.320414

Shao, Y., Zou, D., Li, Z., Wan, L., Qin, Z., Liu, N., Zhang, J., Zhong, L., Huang, P., & Chen, Y. (2013). Blunt Liver Injury with Intact Ribs under Impacts on the Abdomen: A Biomechanical Investigation. *PLoS ONE*, *8*(1), e52366. https://doi.org/10.1371/journal.pone.0052366

Shaw, M. T. (2018). *Introduction to polymer viscoelasticity* (Fourth edition). Wiley.

Shi, Y., & Xiong, D. (2013). Microstructure and friction properties of PVA/PVP hydrogels for articular cartilage repair as function of polymerization degree and polymer concentration. *Wear*, *305*(1–2), 280–285. https://doi.org/10.1016/j.wear.2012.12.020

Siviour, C. R. (2017). *High strain rate characterization of polymers*. 060029. https://doi.org/10.1063/1.4971585

Slotta, J. E., Justinger, C., Kollmar, O., Kollmar, C., Schäfer, T., & Schilling, M. K. (2014). Liver injury following blunt abdominal trauma: A new mechanism-driven classification. *Surgery Today*, *44*(2), 241–246. https://doi.org/10.1007/s00595-013-0515-7

Soden, P. D., & Kershaw, I. (1974). Tensile testing of connective tissues. *Medical and Biological Engineering*, *12*(4), 510–518. https://doi.org/10.1007/BF02478609

Song, G., Chandrashekhara, K., Breig, W. F., Klein, D. L., & Oliver, L. R. (2004). Failure Analysis of Serpentine V-ribbed Belt Drive System. *SAE Transactions*, *113*, 735–749. JSTOR.

Stammen, J. A., Williams, S., Ku, D. N., & Guldberg, R. E. (2001). Mechanical properties of a novel PVA hydrogel in shear and unconfined compression. *Biomaterials*, *22*(8), 799–806.

Steinmann, P., Hossain, M., & Possart, G. (2012). Hyperelastic models for rubber-like materials: Consistent tangent operators and suitability for Treloar's data. *Archive of Applied Mechanics*, *82*(9), 1183–1217. https://doi.org/10.1007/s00419-012-0610-z

Stone, D., LaFontaine, W. R., Alexopoulos, P., Wu, T.-W., & Li, C.-Y. (1988). An investigation of hardness and adhesion of sputter-deposited aluminum on silicon by utilizing a continuous indentation test. *Journal of Materials Research*, *3*(01), 141–147. https://doi.org/10.1557/JMR.1988.0141

Suciu, A. N., Iwatsubo, T., Matsuda, M., & Nishino, T. (2004). Wear Characteristics of a Novel Bearing System for Artificial Knee Joint (Micro-Pocket-Covered Femoral Component and Tibial Poro-Elastic-Hydrated Cartilage). *JSME International Journal Series C*, *47*(1), 209–217. https://doi.org/10.1299/jsmec.47.209

Szabó, G., & Váradi, K. (2018). Failure Mechanism of O-Ring Seals under Extreme Operating Conditions. *Modern Mechanical Engineering*, *08*(01), 11–30. https://doi.org/10.4236/mme.2018.81002

Tay, B. K., Jung Kim, & Srinivasan, M. A. (2006). In Vivo Mechanical Behavior of Intra-abdominal Organs. *IEEE Transactions on Biomedical Engineering*, *53*(11), 2129–2138. https://doi.org/10.1109/TBME.2006.879474

Tracker Video Analysis and Modeling Tool for Physics Education. Retrieved October 24, 2017, from http://physlets.org/tracker/

Treloar, L. R. G. (1944). Stress-strain data for vulcanised rubber under various types of deformation. *Transactions of the Faraday Society*, *40*, 59. https://doi.org/10.1039/tf9444000059

Treloar, L. R. G. (2005). *The Physics of Rubber Elasticity* (Third Edition). Oxford University Press.

Uddin, M. S., & Ju, J. (2016). Multiscale modeling of a natural rubber: Bridging a coarse-grained molecular model to the rubber network theory. *Polymer*, *101*, 34–47. https://doi.org/10.1016/j.polymer.2016.08.037

Urayama, K., Takigawa, T., & Masuda, T. (1993). Poisson's ratio of poly(vinyl alcohol) gels. *Macromolecules*, *26*(12), 3092–3096. https://doi.org/10.1021/ma00064a016

Urrea, F. A., Casanova, F., Orozco, G. A., & García, J. J. (2016). Evaluation of the friction coefficient, the radial stress, and the damage work during needle insertions into agarose

gels. *Journal of the Mechanical Behavior of Biomedical Materials*, *56*, 98–105. https://doi.org/10.1016/j.jmbbm.2015.11.024

Varghese, T., Ophir, J., Konofagou, E., Kallel, F., & Righetti, R. (2001). Tradeoffs in Elastographic Imaging. *Ultrasonic Imaging*, *23*(4), 216–248. https://doi.org/10.1177/016173460102300402

Volumegraphics.com. Volumegraphics.Com. Retrieved December 23, 2019, from https://www.volumegraphics.com/

Volumegraphics.com. Retrieved September 3, 2018, from https://www.volumegraphics.com/

Wan, W. K., Campbell, G., Zhang, Z. F., Hui, A. J., & Boughner, D. R. (2002). Optimizing the tensile properties of polyvinyl alcohol hydrogel for the construction of a bioprosthetic heart valve stent. *Journal of Biomedical Materials Research*, *63*(6), 854–861. https://doi.org/10.1002/jbm.10333

Ward, I. M., & Sweeney, J. (2004). *An introduction to the mechanical properties of solid polymers* (2nd ed). Wiley.

Ward, Ian Macmillan. (1983). *Mechanical properties of solid polymers*. Wiley.

Wittek, A., Miller, K., Kikinis, R., & Warfield, S. K. (2007). Patient-specific model of brain deformation: Application to medical image registration. *Journal of Biomechanics*, *40*(4), 919–929. https://doi.org/10.1016/j.jbiomech.2006.02.021

Xu, L., Zhao, X., Xu, C., & Kotov, N. A. (2018). Water-Rich Biomimetic Composites with Abiotic Self-Organizing Nanofiber Network. *Advanced Materials*, *30*(1), 1703343. https://doi.org/10.1002/adma.201703343

Yang, S.-H., Lee, Y.-S. J., Lin, F.-H., Yang, J.-M., & Chen, K. (2007). Chitosan/poly(vinyl alcohol) blending hydrogel coating improves the surface characteristics of segmented polyurethane urethral catheters. *Journal of Biomedical Materials Research Part B: Applied Biomaterials*, *83B*(2), 304–313. https://doi.org/10.1002/jbm.b.30796

Yannas, I. V. (1974). Nonlinear viscoelasticity of solid polymers (in uniaxial tensile loading). *Journal of Polymer Science: Macromolecular Reviews*, *9*(1), 163–190. https://doi.org/10.1002/pol.1974.230090104

Yeh, W.-C., Li, P.-C., Jeng, Y.-M., Hsu, H.-C., Kuo, P.-L., Li, M.-L., Yang, P.-M., & Lee, P. H. (2002). Elastic modulus measurements of human liver and correlation with pathology.

Ultrasound in Medicine & Biology, *28*(4), 467–474. https://doi.org/10.1016/S0301-5629(02)00489-1

Yeoh, O. H. (1993). Some Forms of the Strain Energy Function for Rubber. *Rubber Chemistry and Technology*, *66*(5), 754–771. https://doi.org/10.5254/1.3538343

Zhai, M., & McKenna, G. B. (2014). Viscoelastic modeling of nanoindentation experiments: A multicurve method. *Journal of Polymer Science Part B: Polymer Physics*, *52*(9), 633–639. https://doi.org/10.1002/polb.23470

Zhang, D., Chen, K., Wu, L., Wang, D., & Ge, S. (2012). Synthesis and Characterization of PVA-HA-Silk Composite Hydrogel by Orthogonal Experiment. *Journal of Bionic Engineering*, *9*(2), 234–242. https://doi.org/10.1016/S1672-6529(11)60116-9

Zhang, Q., Fassihi, M. A., & Fassihi, R. (2018). Delivery Considerations of Highly Viscous Polymeric Fluids Mimicking Concentrated Biopharmaceuticals: Assessment of Injectability via Measurement of Total Work Done "WT." *AAPS PharmSciTech*, *19*(4), 1520–1528. https://doi.org/10.1208/s12249-018-0963-x

Zhao, J., Zhai, F., Cheng, J., He, Q., Luo, J., Yang, X., Shao, J., & Xing, H. (2017). Evaluating the Significance of Viscoelasticity in Diagnosing Early-Stage Liver Fibrosis with Transient Elastography. *PLOS ONE*, *12*(1), e0170073. https://doi.org/10.1371/journal.pone.0170073

Zhong, H., Kim, J., Li, H., Nurushev, T., Movsas, B., & Chetty, I. J. (2012). A finite element method to correct deformable image registration errors in low-contrast regions. *Physics in Medicine and Biology*, *57*(11), 3499–3515. https://doi.org/10.1088/0031-9155/57/11/3499

Zimberlin, J. A., & Crosby, A. J. (2010). Water cavitation of hydrogels. *Journal of Polymer Science Part B: Polymer Physics*, *48*(13), 1423–1427. https://doi.org/10.1002/polb.21968

Zimberlin, J. A., McManus, J. J., & Crosby, A. J. (2010). Cavitation rheology of the vitreous: Mechanical properties of biological tissue. *Soft Matter*, *6*(15), 3632. https://doi.org/10.1039/b925407b

Zimberlin, J. A., Sanabria-DeLong, N., Tew, G. N., & Crosby, A. J. (2007). Cavitation rheology for soft materials. *Soft Matter*, *3*(6), 763. https://doi.org/10.1039/b617050a

Appendix A

Part A:

$$\frac{\partial W(\mathbf{U})}{\partial \mathbf{U}} = 2\mathbf{U}\frac{\partial W(\mathbf{C})}{\partial \mathbf{C}} \tag{A.1}$$

To solve this equation, it is convenient to use Einstein notations

$$\left(\frac{\partial W}{\partial \mathbf{U}}\right)_{ij} = \frac{\partial W}{\partial U_{ij}} \tag{A.2}$$

$$= \frac{\partial W}{\partial C_{kl}}\frac{\partial C_{kl}}{\partial \mathbf{U}_{ij}} \tag{A.3}$$

$$= \frac{\partial W}{\partial C_{kl}}\frac{\partial (U_{km}\, U_{ml})}{\partial U_{ij}} \tag{A.4}$$

By expanding terms and taking the partial derivative, equation A.4 becomes:

$$\left(\frac{\partial W}{\partial U}\right)_{ij} = 2U_{ik}\frac{\partial U}{\partial C_{kj}} \tag{A.5}$$

$$= \left(2\mathbf{U}\frac{\partial W(\mathbf{C})}{\partial C}\right)_{ij} \tag{A.6}$$

Part B:

If a strain function W is a function of strain invariants, W(I_1, I_2, J), then Piola Kirchoff stress tensor (T) and Cauchy stress tensor (σ) can be given as

$$\mathbf{T} = \frac{\partial W}{\partial \mathbf{F}} = \frac{\partial W}{\partial I_1}\frac{\partial I_1}{\partial \mathbf{F}} + \frac{\partial W}{\partial I_2}\frac{\partial I_2}{\partial \mathbf{F}} + \frac{\partial W}{\partial J}\frac{\partial J}{\partial \mathbf{F}} \tag{A.7}$$

$$\boldsymbol{\sigma} = \frac{1}{J}\mathbf{T}\mathbf{F}^T = \frac{1}{J}\left(\frac{\partial W}{\partial I_1}\frac{\partial I_1}{\partial \mathbf{F}} + \frac{\partial W}{\partial I_2}\frac{\partial I_2}{\partial \mathbf{F}} + \frac{\partial W}{\partial J}\frac{\partial J}{\partial \mathbf{F}}\right)\mathbf{F}^T \tag{A.8}$$

The derivation of the strain invariants with respect to the deformation tensor can be defined as

$$\frac{\partial I_1}{\partial \mathbf{F}} = 2\mathbf{F} \tag{A.9}$$

$$\frac{\partial I_2}{\partial \mathbf{F}} = 2I_1\mathbf{F} - 2\mathbf{F}\mathbf{F}^T\mathbf{F} \tag{A.10}$$

$$\frac{\partial J}{\partial \mathbf{F}} = J\mathbf{F}^{-T} \tag{A.11}$$

Equations A.4 and A.5 become

$$\mathbf{T} = \frac{\partial W}{\partial I_2}2\mathbf{F} + \frac{\partial W}{\partial I_2}(2I_2\mathbf{F} - 2\mathbf{F}\mathbf{F}^T\mathbf{F}) + \frac{\partial W}{\partial J}\partial\mathbf{F}^{-T} \tag{A.12}$$

$$\boldsymbol{\sigma} = \frac{2}{J}\left(\frac{\partial W}{\partial I_1} + I_1\frac{\partial W}{\partial I_2}\right)\mathbf{F}\mathbf{F}^T - \frac{2}{J}\frac{\partial W}{\partial I_2}(\mathbf{F}\mathbf{F}^T\mathbf{F}\mathbf{F}^T) + \frac{\partial W}{\partial J}I \tag{A.13}$$

Equation A.13 is equivalent to equation 3.9.

Appendix B

The definition of the stretch term (λ) was based on the initial radius "R" which was equal to 1.42 mm and 1.393 mm in chapters 4 & 5, respectively. These magnitudes were calculated from the initial volume, which was estimated as

$$V_i = V_{n\text{-}b} + V_p \tag{B.1}$$

Where $V_{n\text{-}b}$ is the cylindrical volume of the balloon region, and V_p is the volume at which the material starts to resist balloon inflation. This volume was calculated from the time data of the cavity expansion test. V_P is found to be 9.177 mm^3 and 8.502 mm^3 in liver tissues (chapter 4) and PVA hydrogels (chapter 5), respectively. The definition of λ is based on the assumption that the cavity expands spherically with a spherical volume. The cavity starts from a cylindrical volume ($V_{n\text{-}b}$) that is 5 mm in length and 0.85 mm in diameter, in addition to V_p. It was demonstrated that the initial cavity geometry from which the expansion occurs does not affect the assumption of perfect spherical expansion as long as the volume of this initial cavity is known (Nafo & Al-Mayah, 2019). Therefore, for consistency, the initial volume (V_i) was converted into an equivalent spherical volume by using the concept of Equivalent-Volume Diameter (EVD) (DeCarlo et al., 2004), to define the initial value of R. Thus, we can still base the calibration process on equation 10. The equivalent diameter is calculated as

$$D_e = \sqrt[3]{\frac{6V_i}{\pi}} \tag{B.2}$$

R was then calculated as $\frac{D_e}{2}$

Appendix C

Matlab File Name: LVE_Large_deformation_Yeoh_model

```
N = 100;
time = linspace(0,1,N);
strain1 = linspace(0,0.8,N);
strain = strain1;
params = [3.5e-03,2.9e-03,3e-04,7.837e-02,47.845];%[C10,C20,C30,g,tau]
stress = LVE_uniax(time, strain, params);
figure(1)
plot(strain, stress, '.-b')
xlabel('True strain')
ylabel('True stress (MPa)')
legend('LVE','Location','southeast')

%% Yeoh model. Incompressible hyperelastic hoop stress.
function st_Yh = Yh(strain, params)
C10 = params(1);
C20 = params(2);
C30 = params(3);
lam = exp(strain);
st_Yh = (C10 + 2*C20*(2*lam^2 + lam^-4 - 3) + 3*C30*...
  (2*lam^2 + lam^-4 - 3)^2)*2*(lam^2 - lam^-4);
end

%% Linear viscoelasticity.
function stress = LVE_uniax(time, strain, params)
stress = zeros(1,length(time));
g = params(4);
tau = params(5);
stressV = zeros(1,length(g));
stressH0 = Yh(strain(1), params);
for i=2:length(time)
  stressH1 = Yh(strain(i), params);
  dstressH = stressH1 - stressH0;
  dt = time(i)-time(i-1);
  stress(i) = stressH1;
  for j = 1:length(g)
      stressV(j) = exp(-dt/tau(j))*stressV(j)+...
          g(j)*stressH0*(1-exp(-dt/tau(j)))+...
          g(j)*dstressH/dt*(dt-tau(j)+tau(j)*exp(-dt/tau(j)));
      stress(i) = stress(i)-stressV(j);
  end
  stressH0 = stressH1;
end
end
```